Doctoral theses at NTNU, 2019:43

David Dominikus Eide Brennhaugen

Bulk Metallic Glasses

Deformation and Design

NTNU
Norwegian University of
Science and Technology

Doctoral thesis

David Dominikus Eide Brennhaugen

ISBN 978-82-326-3690-7 (printed ver.)
ISBN 978-82-326-3691-4 (electronic ver.)
ISSN 1503-8181

NTNU
Norwegian University of
Science and Technology

Thesis for the Degree of
Philosophiae Doctor
Faculty of Natural Sciences
Department of Materials Science and
Engineering

NTNU

Norwegian University of Science and Technology

Doctoral theses at NTNU, 2019:43

NTNU

David Dominikus Eide Brennhaugen

Bulk Metallic Glasses

Deformation and Design

Thesis for the Degree of Philosophiae Doctor

Trondheim, February 2019

Norwegian University of Science and Technology
Faculty of Natural Sciences
Department of Materials Science and Engineering

NTNU
Norwegian University of
Science and Technology

NTNU
Norwegian University of Science and Technology

Thesis for the Degree of Philosophiae Doctor

Faculty of Natural Sciences
Department of Materials Science and Engineering

ISBN 978-82-326-3690-7 (printed ver.)
ISBN 978-82-326-3691-4 (electronic ver.)
ISSN 1503-8181

Doctoral theses at NTNU, 2019:43

Printed by NTNU Grafisk senter

Preface

The field of bulk metallic glasses has garnered significant interest in the scientific community during the last few decades. Several very attractive properties, such as high strength, elasticity and formability, as well as good magnetic properties, compete with key limitations such as brittleness and size limitations to achieve widespread usage.

Throughout this project, I have worked on addressing two of the limitations, namely the tendency for catastrophic failure in tension and the high cost of developing new alloys. The work has been done at the Department of Materials Science and Engineering at NTNU, Norwegian University of Science and Technology and at Tohoku University, Japan, resulting in the three papers listed at the bottom.

The thesis is structured around the three papers. For each one, an introduction to the relevant background and theory is given, together with the applied experimental procedures. Finally, the paper is summarized, before the next publication is addressed in the same manner.

The included publications are:

Tensile properties of Zr70Ni16Cu6Al8 BMG at room and cryogenic temperatures
David D.E. Brennhaugen, Konstantinos Georgarakis, Yoshihiko Yokoyama, Koji S. Nakayama, Lars Arnberg, Ragnhild E. Aune
Journal of Alloys and Compounds 742 (2018) 952-957

Probing heat generation during tensile plastic deformation of a bulk metallic glass at cryogenic temperature
David D. E. Brennhaugen, Konstantinos Georgarakis, Yoshihiko Yokoyama, Koji S. Nakayama, Lars Arnberg and Ragnhild E. Aune
Scientific Reports 8, Article number: 16317 (2018)

Predictive modeling of glass forming ability in the Fe-Nb-B system using the CALPHAD approach
David D.E. Brennhaugen, Huahai Mao, Dmitri V. Louzguine-Luzgin, Lars Arnberg, Ragnhild E. Aune
Journal of Alloys and Compounds 707 (2017) 120-125

Acknowledgements

No man is an island, and I am no exception.

Firstly, I would like to thank my two supervisors, Ragnhild E. Aune and Lars Arnberg. I deeply appreciate your guidance, but also your lack of guidance. You have let me be independent and creative. You have been my safety net.

Konstantinos Georgarakis, thank you for sharing with me your experience and your time. I have learned a lot and I have had a lot of fun.

Yoshihiko Yokoyama, thank you for introducing me to the field of metallic glasses. My time with you has formed me as a scientist.

Dmitri V. Louzguine, thank you for letting me be at your lab, and for bringing understanding to my confusion. And my thanks to your whole lab for including me during the time I was there and afterwards.

Huahai Mao, thank you for your time and effort. Your calculations were the cornerstone of our work together, and it would not have been possible without you.

Koji S. Nakayama, thank you for your thoughts and input. Your assessments and analyses have been valuable and have built my confidence in our work.

To err is human, and I am no exception. I mention no names and omit no one.

Everyone at the Department of Materials Science and Engineering at NTNU, thank you. You have not only let me run free but given me shoes to run.

My friends. Thank you. All of you. I would have been far more productive and far less happy without you.

My family. Thank you. With you I can laugh and cry and cry and laugh about it all again.

Last, but very far from least: My wife Dehlia and my daughter Ingrid. I need not say more.

Abstract

Two key limitations to the applicability of bulk metallic glasses are the focus of this thesis. Firstly, the typically very limited plasticity in tension is studied by tensile testing metallic glass samples across a range of temperatures and strain rates. Secondly, a design tool for reducing the normally high cost of discovery of new alloys is tested.

$Zr_{70}Ni_{16}Cu_6Al_8$ bulk metallic glass samples were mechanically tested in tension at nominal strain rates and temperatures of 10^{-4}, 10^{-3}, 10^{-2} and 10^{-1} s^{-1} and 77, 150 and 295 K, respectively. A strengthening is observed with decreased temperature, with yield strength increasing by an average of 16 % from 1503 MPa at 295 K to 1746 MPa at 77 K. Plastic deformability is found highest at 150 K, intermediate at 77 K, and very low at 295 K. At room temperature only a single sample showed any plastic deformation, which occurred due to the intersection and mutual stabilization of several shear bands. At the two lower temperatures, large plastic deformation was accommodated by the stable sliding of a single shear band. Between 150 and 295 K a reversal of strain rate sensitivity is observed, with high strain rate favoring high strength and low plasticity at low temperature and vice versa at room temperature.

In-situ probing of heat generation during the stable sliding of a shear band is achieved by studying localized boiling along the shear band in a sample submerged in liquid nitrogen during testing. By measuring size and frequency of the bubbles, heat release is correlated to plastic deformation, showing that heating occurs even during stable flow at cryogenic temperature, but only becomes noticeable well after onset of deformation. Heat release is therefore considered to be a secondary effect of the shear band deformation.

In the final part of the thesis, a tool for design of new glassy alloys is tested. By combining thermodynamic modelling in the Thermo-Calc software with a topological mismatch factor based on constituent atomic size and compositional ratios, an area in the Fe-Nb-B phase diagram is pinpointed as favorable for glass formation. Both new experimental production and literature data fit well with the predictions of the model, making it worthy of further testing in other systems.

List of Abbreviations and Symbols

ABBREVIATION	DESCRIPTION
BMG	Bulk Metallic Glasses
CALPHAD	CALculation of PHAse Diagrams
DSC	Differential Scanning Calorimetry
GFA	Glass Forming Ability
HV	Vickers Hardness
LN2	Liquid Nitrogen
SEM	Scanning Electron Microscopy
XRD	X-Ray Diffraction

SYMBOL	DESCRIPTION
D_C	Critical diameter
ΔH_{vap}	Heat of vaporization
ΔT_x	Supercooled liquid region
H_C	Coercivity
I_s	Saturation magnetization
m	Fragility index
μ	Permeability
P	Internal bubble pressure
R	Ideal gas constant
R_C	Critical cooling rate
r_b	Radius of bubble
r_n	Atomic radius of element n
r_s	Radius of specimen
ρ	Resistivity
σ_y	Yield strength
T	Temperature
T_g	Glass forming temperature
T_l	Liquidus temperature
T_{rg}	Reduced glass forming temperature
T_s	Solidus temperature
T_x	Crystallization temperature
Ø	Diameter

Contents

1 Introduction

1.1 What are Metallic Glasses?

The opening line of Turnbull's 1969 paper "Under what conditions can a glass be formed" contains the definition that a "glass is considered by technologists to be any solid formed by the continuous hardening of a cooled liquid"[1]. This process-oriented definition was the clearest available at the time, as the structural configurations of glasses were still debated. As the understanding of glasses has evolved, the precision of the term has as well. In the current definition, the further criteria that the material is amorphous and exhibits a glass transition are also included [2]. Excluded from this definition are amorphous metals not formed from the melt, such as those made by pulsed laser deposition, severe plastic deformation etc. [3–5]

The glass transition marks the point where the material changes from being considered a liquid to a solid during cooling. From a rheological perspective, this limit has been arbitrarily set to a viscosity of 10^{12}-10^{14} Pas, which equates to a molecular rearrangement time of more than 24 hours [1,6]. In the thermodynamic sense, the glass transition corresponds do a discrete drop in heat capacity of the material during cooling [7].

The most commonly known glasses are the family of oxide glasses, known from wide applications like windows, kitchenware and optics. Oxide glasses in various forms have been known and used for millennia. However, in their pivotal 1960 paper "Non-crystalline Structure in Solidified Gold-Silicon Alloys", Klement, Willens and Duwez showed that the amorphous structure could also be achieved by quenching metallic alloys [8]. This was initially only possible in extremely thin sections produced by techniques like splat quenching, melt spinning etc. due to the extreme cooling rates required [9].

Through pioneering work by Chen, Inoue, Johnson and others [10,11] throughout the 1970's, 80's and 90's, the known glass forming alloys grew in both number and size, entering the realm of bulk materials. In this work, all samples where the smallest section thickness is at least 1 mm are characterized as "bulk" [12]. Bulk Metallic Glasses (BMG) have been produced in diameters ranging from 1 to several 10's of mm, in various systems including Zr-, Fe-, Ti-, Pd- and Cu-based alloys [13].

In summary, metallic glasses are amorphous metals with a distinct glass transition, produced from the melt. When available in thicknesses above 1 mm, they gain the additional distinction "bulk".

The difficulty in producing metallic glasses gives rise to an important question: Why? In the following Section 1.2, a brief overview of the attractive properties of metallic glasses are introduced.

1.2 Properties and Applications

Ashby and Greer called metallic glasses a category of materials that was born "homeless" – they originated from basic research without any intended use, and suitable applications were, or have to be, identified based on their properties [14]. Metallic glasses do indeed possess some unique, interesting and beneficial properties, but also some critical limitations that need to be considered.

Among the earliest exploited properties in metallic glasses was the soft magnetism found in the Fe-based alloy family. Compared to standard electrical steel, Fe-based alloys show lower coercivity as well as higher resistivity and permeability, while drawbacks include lower saturation magnetization and sometimes higher magnetostriction, as well as higher production costs [14–16]. Currently, soft magnetic metallic glasses are in widespread use as inductor cores in electrical transformers, especially on the power grid in China and India.

Metallic glasses further exhibit a host of attractive mechanical properties, which have become more exploitable as the size limitations for the alloys have relaxed with research. Characteristics such as high strength, hardness, toughness, elasticity, abrasion and corrosion resistance are found in many of the alloys, owing to their amorphous atomic structure [16]. Limitations in plasticity, especially in tension, and size have been alleviated by selective and precise application in areas like sporting goods, micro machinery and consumer electronics, where neither materials cost nor risk of failure are critical [17].

Although there are several stories of successful commercialization, some significant hinders still await scaling. In Section 1.3, an outline of the motivation and approach for the present work is given.

1.3 Motivation

The work in this PhD project has been centered around increasing the practical applicability of BMGs. The focus has been on two important limitations to the class of materials, namely the limited plastic deformability in tension, leading to very abrupt catastrophic failures, and the high cost of designing new alloys.

The first two included papers focus on tensile testing of the $Zr_{70}Ni_{16}Cu_6Al_8$ BMG under various conditions. Limited plasticity leading to sudden, catastrophic failure has been amongst the primary hindrances for reliable application of BMGs as structural materials. The investigated alloy was originally designed specifically with tensile plasticity in mind [18,19]. Initially promising results [20–22] were followed up on in order to further refine the applicability of the alloy through mechanical testing at various imposed strain rates and ambient temperatures [23]. An even deeper investigation of the fracture mechanism, by studying heat generation during failure at cryogenic temperature, followed.

In the final paper, focus was shifted from Zr-based BMGs to the Fe-based family. Metallic glasses in the Fe-Nb-B system have shown promising mechanical properties with ultrahigh strength and appreciable compressive plasticity, often not expected in Fe-based alloys [24]. Good soft magnetic properties [25] combined with a significantly lower cost of raw materials compared to Zr-alloys makes this system an interesting topic. A design process aimed at low-cost exploration for new BMG alloys through reducing experimental work was tested by combining thermodynamic modeling by the CALPHAD (CALculation of PHAse Diagrams) method [26] and topological glass forming indicators [27,28].

2 Deformation in Metallic Glasses

2.1 Mechanical Properties

As already mentioned in Section 1.2, metallic glasses exhibit a host of interesting mechanical properties.

In conventional crystalline metals, easy slip planes and presence of dislocations limit the achievable yield strength, σ_y. Correspondingly, the absence of these features in metallic glasses lets their strength approach the theoretical limit based on interatomic bond strength [14,29,30]. Typical numbers of σ_y for construction steel and tool steel are in the range of 100-500 MPa and 1000- 2000 MPa, respectively [31]. In comparison, σ_y of metallic glasses routinely reaches 1500 MPa [30], and has been reported reaching up to 5000 MPa [14,24].

The lack of crystallographic slip directions and dislocations also removes the primary mode for crystalline materials to accommodate deformation [29]. Consequently, their responses to stress differ significantly. The relatively high σ_y, in combination with Young's moduli typically lower than the 210 GPa of steel, *e.g.* 70 GPa for $Zr_{70}Ni_{16}Cu_6Al_8$ [19], results in high elastic deformability [14,32]. The elastic limit is reported to be remarkably uniform around 2 % across metallic glasses of various compositions [32–34].

Associated with high σ_y, this group of alloys also shows exceptionally high hardness. A reported value of Vickers Hardness (HV) 1200 [25] for a Fe-Nb-B alloy compares favorably to HV 120 for austenitic steel and HV 1000 for pure martensite at 0.8 wt% C [31]. This high hardness also gives rise to excellent abrasion resistance and the ability to achieve and maintain a highly polished surface. Surface performance is further aided by a high corrosion resistance due to the lack of grain boundaries and other corrosion initiation points [29]. Especially Zr-based BMG have proven to have good corrosion properties in halide free solutions, but to be susceptible to pitting and stress corrosion cracking when Cl^- ions are present [35–37].

Whereas dislocations typically cause strain-hardening after yield in common metals, metallic glasses experience strain-softening [38]. This softening leads to one of the major hurdles in the widespread applicability of metallic glasses as it significantly limits plastic deformability. Furthermore, a unique discrepancy between properties in compression and in tension arises [29]. For example, Conner *et al.* reported a fracture strength of 1800 MPa and 0.5 % plastic deformation in compression, but only 1200 MPa and no plasticity in tension for the $Zr_{57}Nb_5Al_{10}Cu_{15.4}Ni_{12.6}$ BMG [39]. Metallic glasses are also typically very sensitive to extrinsic defects, *e.g.* casting porosity and surface scratches, as well as on sample geometry [33,40]. In combination with a strong dependence on intrinsic factors, such as variable structure with cooling rate during production, the reliability of the mechanical properties can be limited. Some work has, however, been done on establishing proper safety thresholds [33], or on circumventing the challenges by very specific application of the materials [14,17].

After yield, any plastic deformation in metallic glasses is usually accommodated by shear bands, *i.e.* the sample is intersected at roughly 45 ° by several deformed bands, forming steps on the surface [41]. Localized sliding in these bands results in global plastic strain, with a higher number of bands generally corresponding to higher deformation before fracture [42].

In very small volumes, below the µm range, the deformation mechanisms of metallic glasses change, with homogeneous plastic deformation becoming more reliable [43]. This, in combination with an excellent ability for thermoplastic forming in the supercooled liquid temperature range, makes metallic glasses a good candidate for micro-machinery parts [44]. Formability, elasticity and strength also make the material attractive for gears and compliant mechanisms for space travel purposes, where good low-temperature properties are a further benefit [45,46].

2.2 Properties at Low Temperatures

Many crystalline materials, for instance ferritic steels, become brittle at low temperature due to dislocation mobility dependence on temperature. The possibly catastrophic consequences of this ductile-to-brittle transition is famously exemplified by the case of the Liberty-class ships, of which almost 10 % sank or incurred irreparable damage during operation at winter temperatures [47].

In the case of metallic glasses, the opposite effect is seen. In general, a significant strengthening is observed[23,34,48,49], as well as an increase in plastic deformability – both in tension [20,23,48] and in compression[40,48]. For concrete examples, tensile plastic deformation of the $Zr_{70}Ni_{16}Cu_6Al_8$ BMG increased from negligible to 2 % when reducing temperature from 298 to 77 K. σ_y increased by 16 % from 1503 to 1746 MPa over the same span [23]. Similarly, under compression of $Zr_{60}Ni_{25}Al_{15}$ BMG, plasticity and σ_y increased from 3.5 % to 16.7 % and from 1791 to 2217 MPa, respectively [48]. This strengthening has been partially linked to an increase in Young's modulus due to a reduced interatomic distance, but an additional strain rate sensitivity below a critical temperature has also been proposed [40]. The increased deformability has been attributed to nucleation of a higher number of shear bands [42].

In some cases, however, cryogenic temperatures have been found to result in further localization of plasticity, *i.e.* from being spread across several shear bands at room temperature to confinement into a single heavily deformed shear band at cryogenic temperature [20,23,40]. Single shear band plasticity is related to a more pronounced strain softening and a lower σ_y than multi shear band plasticity, and often initiates at extrinsic defects in the sample [40].

The increase in both strength and ductility at low temperatures, carves out an important niche for metallic glasses. They can be applied for cryogenic applications without fear of premature failure, as is experienced in some crystalline materials. Important areas include aerospace applications, where low temperature strength combined with formability and high hardness facilitates uses in lubrication-free machinery [45]. Further, the materials are well suited for cryogenic vessels related to superconducting fields [48].

2.3 $Zr_{70}Ni_{16}Cu_6Al_8$

The particular alloy chosen for evaluation in this work is the Zr-based BMG $Zr_{70}Ni_{16}Cu_6Al_8$. This alloy was specifically conceived with tensile ductility in mind. A low Young's modulus and a high Poisson ratio have been proposed to facilitate shear band formation. Optimization for those two factors within the Zr-Ni-Cu-Al quaternary alloying system, led to the hypoeutectic composition $Zr_{70}Ni_{16}Cu_6Al_8$ [18]. This alloy initially exhibited a 1.7 % tensile plastic elongation at

a strain rate of $1.6 \cdot 10^{-1}$ s^{-1}. By increasing cooling rate during casting, and slightly reducing strain rate to $1.5 \cdot 10^{-1}$ s^{-1}, plasticity was increased to 2.8 % [19].

The alloy was further investigated in tension while monitored by a high-speed camera by Yokoyama *et al.* with the aim of a deeper understanding of the shear banding mechanism, and related temperature increase [21]. For a plastic elongation of 1.3 %, they estimated a shear band core temperature of 852 K, based on the equilibrium viscosity-temperature relationship of the alloy.

Tensile plasticity was found to increase further at lower strain rates, 10^{-3} and 10^{-4}, when testing at cryogenic temperatures [20,50]. Both works reported some occurrences of concentration of deformation from multiple shear bands into a single one at low temperature and strain rate, even though not all samples exhibited this under the same conditions.

In order to evaluate the suitability of the alloy for biomedical applications, several corrosion studies have been performed. Although metallic glasses in general show good corrosion resistance, Zr-based alloys have been reported to be susceptible to pitting and stress corrosion cracking [37]. The Zr-enriched $Zr_{70}Ni_{16}Cu_6Al_8$ alloy, however, compared to the previously known $Zr_{50}Cu_{40}Al_{10}$ and $Zr_{50}Cu_{30}Al_{10}Ni_{10}$, showed passivation even in 0.5 M NaCl solution, making it an interesting candidate for biocompatibility testing [35,36].

3 Paper 1 – Tensile Properties

3.1 Methods

3.1.1 Arc Melting

Arc melting was used for production of the precursor alloys of all the reported metallic glasses. This is a versatile technique, which allows production of high-purity alloys with high melting temperatures under inert atmosphere. Figure 3.1 shows a schematic illustration of the equipment, where the elements to be melted are placed in a cavity on a water-cooled Cu hearth, inside a chamber with an Ar atmosphere of 5N purity. An electric arc is established between a W electrode and the hearth, and used to melt the elements together, forming a precursor "master alloy ingot." The arc is maintained for some time, typically 60 seconds, to allow for full melting and diffusion off alloying elements. The ingot is then flipped, bottom side up, and re-melted using the same procedure. This is repeated three to five times, to ensure homogenization even for the cold parts of the ingot which have been in contact with the hearth during melting.

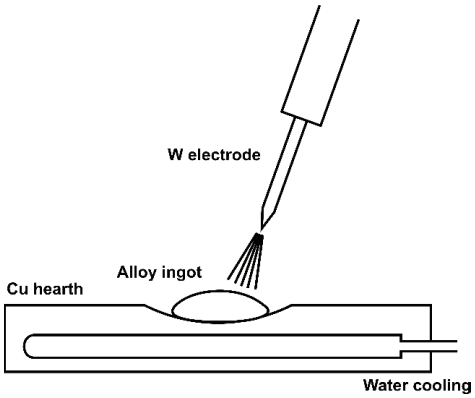

Figure 3.1: Schematic illustration of the arc melting principle for alloying of metallic glasses.

In the present project, Fe-Nb-B master alloy ingots of 5 g were produced in an Edmund Bühler MAM-1 mini arc melter, while the $Zr_{70}Ni_{16}Cu_6Al_8$ ingots were produced by a custom built Diavac Limited automatic arc melter, capable of simultaneously making 22 ingots of 25 g each.

Elemental metals of at least 99.9 % purity and B crystal of 99.5 % purity were used for production, as impurities such as oxygen have been shown to have a significantly adverse effect on glass formation [51]. The Zr source was in the form of crystal rod, which improves glass formation over sponge Zr [52].

3.1.2 Tilt Casting

For casting larger diameter $Zr_{70}Ni_{16}Cu_6Al_8$ rods of Ø=3.5 mm, tilt casting was applied. As an extension of the arc melting technique, tilt casting allows for production of relatively large samples on the mm to cm scale. As illustrated in Figure 3.2, pre-alloyed ingots are molten in a shallow cavity on a cooled Cu hearth by arc melting. Once sufficient temperature is reached, the hearth is tilted on a rotational axis, allowing the molten alloy to flow into the mold driven by gravity.

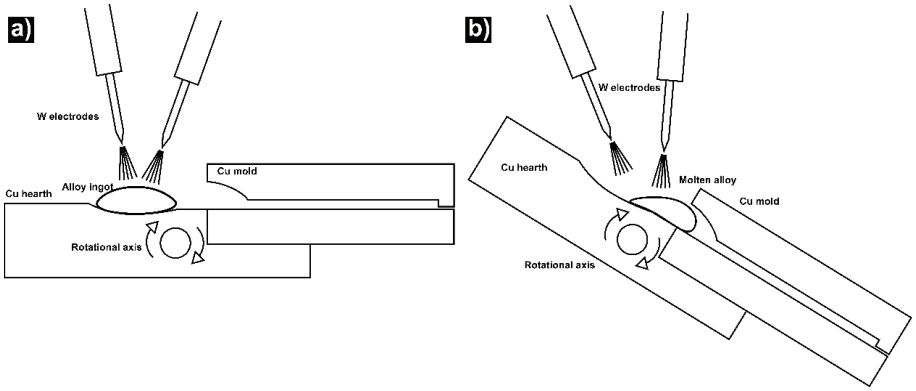

Figure 3.2: Schematic overview of the tilt casting technique, with a) showing initial heating of the alloy ingot and b) tilting of the hearth allowing the molten alloy to flow into the mold.

A Nissin Giken manual double-torch arc melter was used for production of the reported $Zr_{70}Ni_{16}Cu_6Al_8$ samples. The two W torches allow for high convection during melting, avoiding any crystalline inclusions, as well as continuous heating even while the alloy is being poured into the mold [53].

3.1.3 X-Ray Diffraction

X-ray Diffraction (XRD) is one of the most commonly applied methods for verifying successful production of metallic glasses. Contrary to crystalline samples, which show sharp characteristic peaks as seen in Figure 3.3 c), amorphous substances produce only a broad, continuous, wave-like diffraction pattern, Figure 3.3 a). The in-between stage of a partially amorphous, partially crystalline sample results in an XRD diffractogram as shown in Figure 3.3 b), consisting of a wavy baseline with sharper peaks. All three samples in Figure 3.3 were produced by melt spinning Fe-Nb-B alloys, see Section 7.1.3, and reported in the paper "*Predictive Modeling of Glass Forming Ability in the Fe-Nb-B System Using the CALPHAD Approach*" [54].

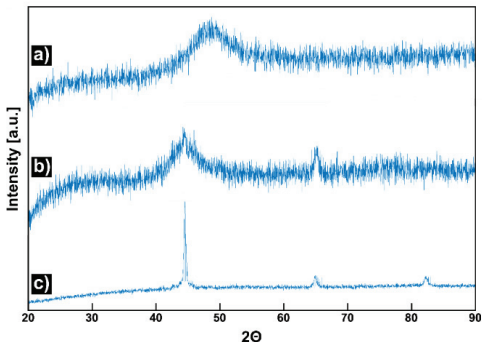

Figure 3.3: Example XRD patterns showing Fe-Nb-B samples which are a) fully amorphous, b) partly amorphous and c) fully crystalline.

Depending on sample geometry, the reported alloys were mounted differently to ensure representative results. Melt spun Fe-Nb-B ribbons, see Section 7.1.3, were fastened flatly on a Si sample holder in a Bruker D8 Advance, with a Cu target and scanned at 2θ in the range 20-90 °. The scans were performed twice, with both the wheel-contact surface and the non-contact surface facing upwards to account for differences in cooling rate. Ø=1 mm Fe-Nb-B rods produced by suction casting, see Section 7.1.2, were polished lengthwise, into semicylindrical shape, allowing for XRD analysis of the cross section along the entire rod. These samples were scanned with Mo-Kα radiation with 2θ at 5-50 ° in a Bruker D8 Advance. From the Ø=3.5 mm $Zr_{70}Ni_{16}Cu_6Al_8$ tilt cast rods, Ø=3 mm cylinders were machined from sections close to those machined into tensile specimen. XRD scans were performed on-edge on these cylindrical samples in a Rigaku Ultima IV, with a Cu target and 2θ values 20-100 °.

3.1.4 Tensile Testing

Mechanical properties of the $Zr_{70}Ni_{16}Cu_6Al_8$ samples were investigated by tensile testing. The cast rods were machined into tensile specimen with Ø=0.8 mm, L=2.3 mm gauge areas. Tests were performed at nominal strain rates 10^{-4}, 10^{-3}, 10^{-2} and 10^{-1} s^{-1} and temperatures 77 K, 150 K and 295 K. All experiments were recorded using a high frame-rate camera. Due to high compliance in the sample holder required for recording and Liquid Nitrogen (LN2) submersion, the actual strain rate in the gauge area during elastic deformation was only about 20 % of the applied strain rate.

Temperature control was achieved by use of a LN2 bath. For experiments at 77 K both the sample and parts of the sample holder were submerged in LN2. For tests at 150 K, however, the sample and sample holder were suspended immediately above the surface of the LN2 bath.

A sample holder, consisting of an inner rod inside an outer tube, as illustrated in Figure 3.4, let the sample holder be connected to the testing rig only from above. This allowed for submersion of the sample and sample holder in the LN2 bath inside a double-walled quartz container with a flat window section for unaberrated observation using the camera. A thermocouple mounted on the sample holder monitored temperature during the 150 K testing.

To confirm the accuracy of the temperature measured by the thermocouple, test runs were made of the 150 K temperature regime with an extra thermocouple soldered to the sample itself. An offset of 25 K was found, which was accounted for during the tensile tests. Although temperature measurement was accurate to within ±5 K with this setup, temperature control was not achievable beyond ±20 K. For simplicity, all tests suspended over the LN2 bath are still designated as “150 K.”

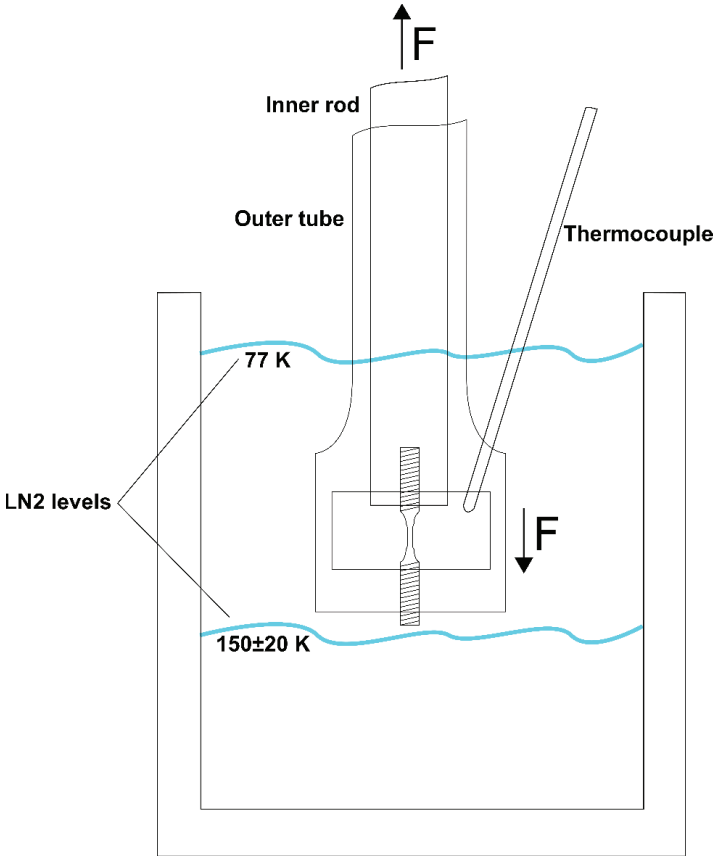

Figure 3.4: Schematic overview of the applied tensile testing set-up

A strain-rate controlled Shimadzu AG-X testing rig was used to perform the tensile tests. Load and cross beam displacement were recorded by the Shimadzu TRAPEZIUM X software. A Photron FASTCAM SA1.12 high-speed camera was used to record the sample surface during testing at framerates 60, 125, 1000 and 5400 Hz for tests at 10^{-4}, 10^{-3}, 10^{-2} and 10^{-1} s^{-1} respectively. The camera also recorded corresponding load data for each video frame, allowing the video to be synchronized to the testing rig data. Due to limited storage space, the camera was set to start overwriting its oldest data once storage capacity was reached. A sensor measuring conductivity through the tensile specimen was set to stop the camera immediately upon fracture, to keep the relevant parts of the video from being overwritten. The stored data typically amounted to 50.000 images. Results from both the testing rig and the camera were used in combination to obtain as accurate stress-strain relationships as possible.

3.1.5 Video Analysis

The videos recorded by the high frame-rate camera were analyzed by using Digital Image Correlation (DIC). Two similar pieces of software were used to analyze all videos, and compared for verification of results. eCorr v4.0 software by SIMLab, NTNU [55], was used for primary analysis. The obtained results were verified by running the same analysis in TEMA

Automotive software by Image Systems AB. Both softwares are able to automatically recognize and track high-contrast features in a video.

Figure 3.5 a) and b) show video snapshots from the beginning and end of elastic deformation in a sample, respectively. The green dots and squares mark the various high-contrast points, which were tracked by DIC throughout deformation. The relative distance between the points was used to measure strain, as plotted in blue in Figure 3.5 c). Each dot in the blue line represents measurements from a single image obtained by the camera. Strain measured by the crossbeam displacement, red dashed line, had lower scatter, but included significant error due to machine compliance. The true stress-strain relationship was therefore found by linear regression of the elastic deformation from DIC, combining with plastic deformation from the testing rig, and scaling the latter to fit with DIC measurements. The resulting curve is shown as a solid yellow line.

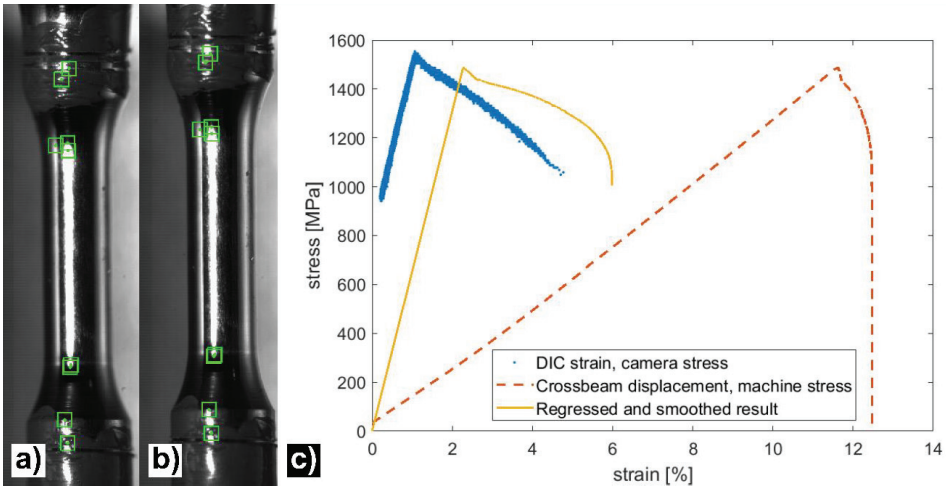

Figure 3.5: Stress-strain analysis by DIC: Tensile specimen at the beginning of elastic deformation, with points used for DIC marked by green squares, a), and the same specimen at the end of elastic deformation, b). c) Shows the combination of DIC data, blue dots, with crossbeam displacement, red dashes, to find the true stress-strain relationship, yellow line.

3.1.6 Scanning Electron Microscopy

Scanning Electron Microscopy (SEM) was used to observe the Zr specimens after tensile testing. A Zeiss Ultra 55 and a Hitachi S-3400N were both used in secondary electron mode with accelerating voltages of 10 and 15 kV to study the surface topography. For top-down analysis of the fracture surfaces, the samples were mounted standing vertically inside the SEM, giving a circular projection of the features. The fractures occurred at 54 ° to the tensile axis due to shear banding, see Section 4.2, which was accounted for during measurement of fracture features.

3.2 Summary of Paper

3.2.1 Introduction

The paper is titled "Tensile Properties of $Zr_{70}Ni_{16}Cu_6Al_8$ BMG at Room and Cryogenic Temperatures", published in Journal of Alloys and Compounds, Volume 742, 25 April 2018, Pages 952-957 [23]. This is a re-analysis of data from experiments conducted at Tohoku University during my master thesis in 2013 and 2014 [50]. A large number of samples were produced and tensile tested over a range of temperatures and strain rates, as previously explained in Section 3.1. The use of a high frame-rate camera during testing, as well as tests performed at cryogenic temperatures put this body of data in a unique position for the study of deformation in BMG. Plastic deformation in tensile mode is normally not expected for BMG, but some positive reports for this and similar alloys at cryogenic temperatures motivated this study [20,48,56].

3.2.2 Results

Tensile testing was performed on $Zr_{70}Ni_{16}Cu_6Al_8$ samples at nominal strain rates 10^{-4}, 10^{-3}, 10^{-2} and 10^{-1} s^{-1}. Further, each strain rate was applied at temperatures 295, 150 and 77 K, for a total of 12 different conditions. The target temperatures were achieved by testing at ambient temperature, with the sample and sample holder submerged in LN2 and with the sample suspended immediately above the LN2 surface, as detailed in Section 3.1.4.

Images recorded by the high frame-rate camera were analyzed by DIC, as explained in Section 3.1.5. The combination of DIC data and values gathered for crossbeam displacement in the testing rig was used to estimate the true stress-strain relationship.

Firstly, an increase in yield stress, σ_y, of 16 % was observed when decreasing temperature from 295 to 77 K. Average σ_y was 1503, 1584 and 1746 MPa for 295, 150 and 77 K, respectively. These results were in good accordance with previous reports of low-temperature strengthening [40,48,56,57]. Interestingly, an apparent reversal of strain rate sensitivity happened between 295 and 150 K. As seen in Figure 3.6, σ_y is negatively correlated with strain rate at room temperature. At the two cryogenic temperatures, the reverse is seen, with higher strength at higher strain rate.

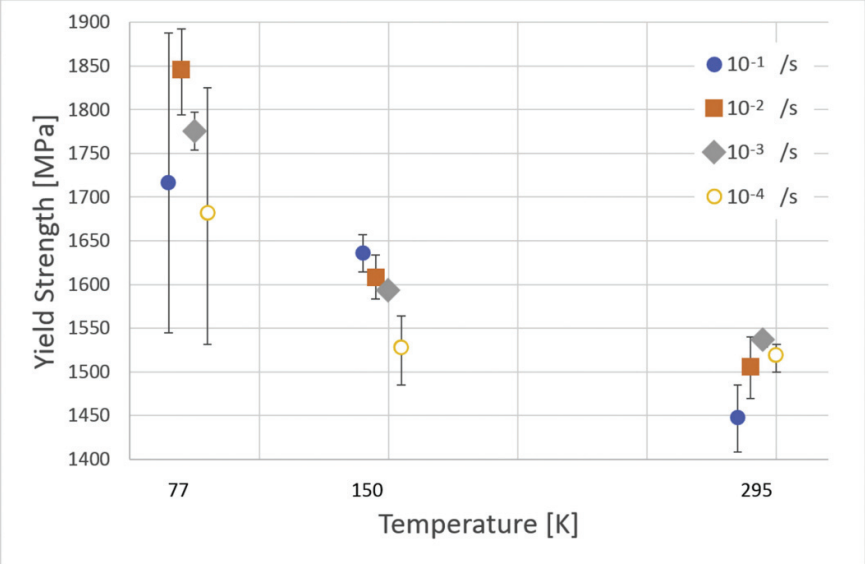

Figure 3.6: Yield strength dependence on temperature and strain rate.

Maaß et al. suggested a non-Newtonian, positive strain-rate dependence of σ_y below a transition temperature 200 K for a similar alloy [40], which fits well with these observations. The negative strain rate dependence above the transition was however not accounted for in their model.

Plastic deformation was observed for at least some samples at all temperatures. Interestingly, as can be seen in Figure 3.7, the highest degree of plastic deformation was observed at the intermediate temperature, 150 K. At room temperature, only a single sample, tested at 10^{-1} s^{-1} showed any plasticity, 0.42 %, attributed to the interaction and mutual stabilization of two primary shear bands. There again appears to be a reversal of strain rate sensitivity. The sensitivity in this case is the opposite to that of σ_y, with higher plasticity at low strain rate at low temperature, and at high strain rate at high temperature. Roberts *et al.* reported a decrease of fracture toughness in Zr-based BMGs of 65 % with decreasing temperature from room to LN2 temperatures [58]. This embrittlement, in competition with shear band stabilization, could explain the lowered, but still present, plasticity at 77 K.

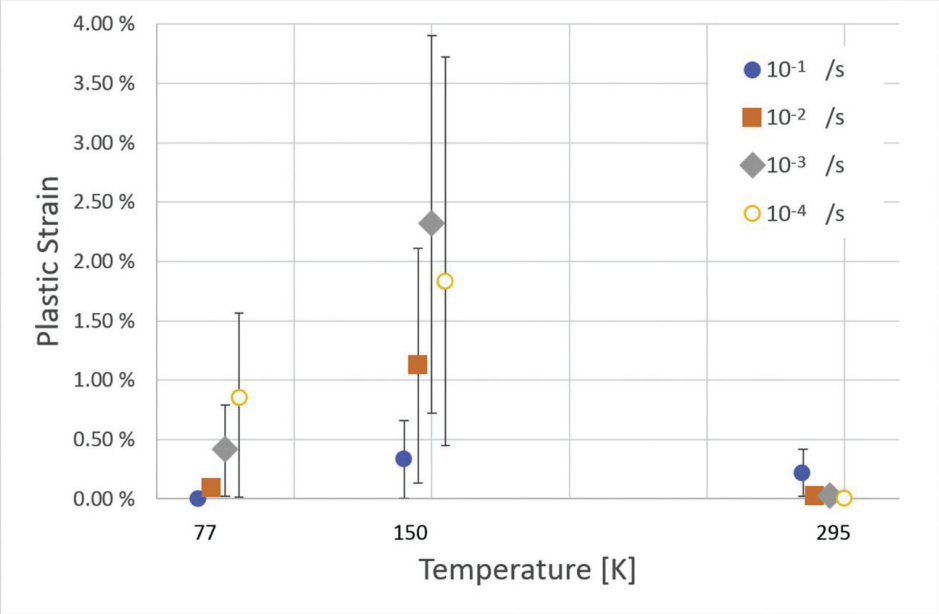

Figure 3.7: Plastic deformation dependence on temperature and strain rate.

Similarly to previous reports, some of the samples tested at low temperature had their plastic deformation contained in a single shear band [40,59], while room temperature plasticity is typically related to nucleation of a high number of shear bands [19]. At the lowest strain rates, shear band sliding along a single plane could be observed over several tens of seconds. With the understanding that plasticity in shear bands is dominated by diffusion of shear transformation zones, low temperature and strain rate could stabilize shear bands by slowing kinetics to a degree that prevents the shear band from accelerating into catastrophic failure.

Tensile plasticity is normally not expected in BMG, making the present article one of a few remarkable reports [19,21,59]. The results are especially surprising considering the low stiffness in the sample holder, which typically negatively impacts plasticity [41]. A reduction in fracture toughness competing with kinetic stabilization is proposed to account for the drop in plastic deformation at 77 K.

3.2.3 Conclusion

A strengthening of 16 % was observed when reducing tensile testing temperature from 295 to 77 K. A reversal of strain rate sensitivity was observed between 150 K and 295 K, *i.e.* from positive to negative for σ_γ and opposite for plastic deformability.

The character of plastic deformation also changed: At room temperature, only one sample, with several intersecting and mutually stabilizing shear bands showed any plastic deformation. At cryogenic temperatures, stable shear over several minutes in a single shear band was observed, although not in all samples at the same conditions. Plastic deformability was found highest at 150 K, medium at 77 K and low at 295 K.

3.2.4 Limitations

For each of the twelve experimental conditions, two or three parallel tests were performed. Statistical significance would have been greatly improved by increasing the number of samples, although this was not possible within the given time constraints of production and testing. The application of a strain gage on the back side of the sample could have given further data for correcting the stress-strain relationship, which would have improved reliability.

3.2.5 Further Work

The available high frame-rate camera footage from the experiments was found especially interesting. In the case of samples submerged in LN2, boiling was observed along the circumference of the main shear band well in advance of fracture. This opens a line of deeper investigation into shear band heating using the same data set, which is pursued in Paper 2.

The marked improvement of mechanical properties in the samples at cryogenic temperatures would also be interesting to compare across alloys in a systematic fashion. The first steps towards this are taken in Paper 3, when the main focus is shifted towards the design of new alloys.

4 Shear Bands in Metallic Glasses

4.1 Atomic-level Structure

The first paper to report a metallic glass, published by Klement *et al.* in 1960, described the acquired structure as amorphous[8]. However, due to the impossibility of distinguishing the diffraction patterns of nanocrystalline and amorphous solids, there was still real debate as to the true structure of glasses a decade later [1]. Bernal constructed a model showing that monoatomic liquids could attain a dense structure without periodic repetition by combining various face-sharing polyhedra, which showed good accordance with experimental density distribution functions [60]. This was also used as a basis for understanding glassy structures, although metallic glasses typically consist of at least two different species [1]. Cohen and Turnbull did however predict already in 1959 that even pure atomic liquids should be able to reach a glass transition, if cooled rapidly enough [61]. Indeed, Zhong *et al.* succeeded in 2014 in producing monoatomic metallic glasses on the scale of 50 nm from Ta, V, W and Mo [62].

The more complex concept of amorphous polyatomic alloys was, among others, tackled by Miracle [63,64]. The proposed Efficient Cluster Packing (ECP) model allows for atoms of three distinct sizes to form a structure where solvent atoms form a tight cluster around a solute atom. These clusters are then arranged in a face-centered cubic configuration, with atoms of a second solute filling the gaps between the clusters. Resulting from this model, are very distinct preferences for certain ratios of constituent atom radii, as well as for certain preferred compositions for good glass forming alloys.

Later updates to the model extended it by a fourth distinct atomic size [65] and allowed for the clusters to be packed as icosahedra rather than in a face-centered cubic configuration [66]. The extended model, combined with extensive comparison to experiments, allowed for some degree of predictive success, even when only topological and not chemical factors are considered [66].

Although amorphous, the above models show that the structure of glasses is not entirely random. The discussed clustering is driven by a typically large negative heat of mixing between constituent atoms, which drives identical atoms from one-another by favoring unlike bonds [64,65]. As a result, glasses exhibit degrees of short- and medium-range ordering, although long-range ordering can, by definition, not be present. Experimental findings fit quite well with the ordering introduced by the ECP [64,67].

A very important concept in the structure of metallic glasses is free volume, which is the difference in density between optimal packing, as described by Miracle and Bernal [60,63], and that of an actual glass [64]. The free volume in a particular sample increases with the imposed cooling rate during vitrification, and is directly linked to an increase in plastic deformability [68]. Further tuning after casting is possible, where for example shear deformation [69,70] and cryogenic cycling [71,72] will increase the contained free volume (“rejuvenation”), while annealing decreases it (“relaxation”)[70], making the sample more brittle.

The free volume in a specimen is randomly distributed throughout its volume, leading to structural heterogeneities [70,73]. This distribution causes some atomic clusters to have a reduced resistance to deformation compared to the average of the material [74]. Such zones

are commonly referred to as Shear Transformation Zones (STZs) [29]. Although they have quite diffuse boundaries to the matrix, the number of atoms constituting an STZ is typically considered to be on the order of 10-100 [41]. Therefore, their cross-sectional dimension should be in the range of 1-10 nm. Macroscopic plastic deformation typically occurs through the cooperative deformation of these STZs, when they form into shear bands intersecting the specimen [74].

4.2 Shear Bands

Shear deformation gives a local increase in free volume [73,74]. At temperatures well below T_g, atomic diffusion in the glass is too slow to quickly compensate for this generation of free volume, leading to a further weakening of the STZ through shear dilation. This process leads to a self-intensifying shear localization roughly along the plane of maximum shear, at 45° to the deformation direction [74]. As a consequence, macroscopic plastic deformation happens in the form of heavily deformed steps called shear bands [29,41]. These shear bands have a thickness in the range of 10-20 nm, as measured by TEM observations [75]. Their angle to the deformation axis varies both by specific alloy and by deformation mode, with shear bands generated under compressive loads having typical angles of 40-45°, and tensile loads giving angles of 50-57° [76]. An example of a fractured tensile specimen with a visible shear band on the surface is shown in Figure 4.1.

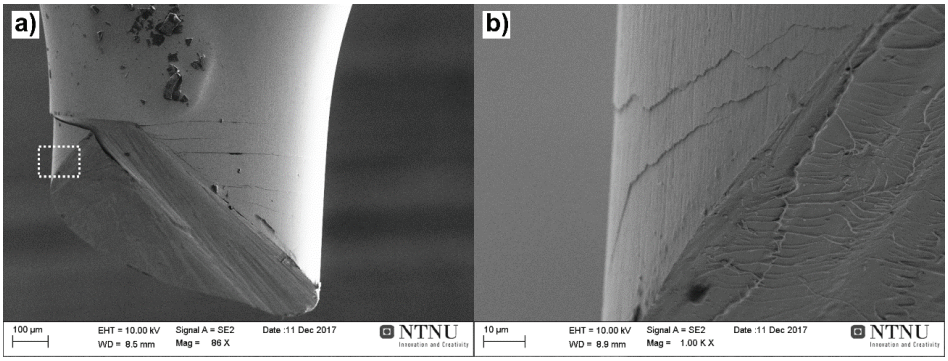

Figure 4.1: Side view of a $Zr_{70}Ni_{16}Cu_6Al_8$ BMG sample tested in tension, after fracture. In a) the fracture surface can be seen to be along the intersection of a primary and a secondary shear band, with several other secondary bands originating from the fracture surface. The area marked by a dotted square is enlarged in b), showing the steps of further minor shear bands.

The shear band nucleates once sufficient stress is present to allow a set of STZs to operate cooperatively. Nucleation therefore often happens at stress concentrators, such as micro voids or surface notches, which activate nearby STZs [40,41]. Activation of a shear band across a sample has previously been shown to occur within less than 1.7 ms by high speed cinematography [77], although sliding of the two opposed surfaces can last longer [78]. The structural dilation experienced inside the shear band further increases local free volume, leaving an arrested shear band weaker than the matrix material [41].

Post-mortem inspection of fractured samples reveal that any plasticity typically is the product of several shear bands, each with individual shear offsets in the µm range [79,80]. Under imposed load, several shear bands can nucleate, propagate and arrest simultaneously or

sequentially, due to the elastic unloading of the sample following shear band sliding [81]. Repetition of this mechanism gives rise to serrations observed in the stress-strain curve during compressive testing of BMGs [80].

The displacement of single shear bands scales proportionally with the specimen cross section [79], with typical sliding distances reported in the 10-1000 nm range [82]. Shear banding as a phenomenon disappears once the sample is below a critical thickness on the micrometer scale [43]. Temperature approaching T_g or very low deformation rates also tend to homogenize plastic deformation [73].

Although the initial localized weakening that causes a shear band to form is of structural origin, the temperature inside an operating shear band has been the subject of long-standing debate. This is examined more closely in the following.

4.3 Localized Heating

Localized temperature increase has been considered both as the initiating and the arresting mechanism for shear bands, as well as a secondary effect. Estimated temperature increases range from 10^{-2} K [74] to 10^{4} K [83] for various alloys and shear offsets. Considering the shear band as a high friction environment, heat release depends on sliding speed, distance and shear band thickness [79,82]. The fracture surfaces of BMGs typically show a veined pattern, called Saffman-Taylor fingering, characteristic of a viscous meniscus between two separated plates [84]. This, together with observed sparks during failure and drops of molten material on the fracture surfaces, strongly suggests that high temperatures are involved in failure [41], although the exact timing of heat release is debated.

Since many shear bands are found to arrest by themselves, Argon considered whether a 7 nm thick shear band with a shear offset of 100 nm would be able to generate enough heat to self-anneal to counteract its structural softening. However, his calculations only estimated a temperature increase in the range of 10^{-2} K, insufficient by orders of magnitude to initiate the effect in question [74]. Arrest of active shear bands has later been proposed to be due to elastic relaxation in the sample during shear banding, which removed the stress required for further propagation [80].

Local temperature rise was also a considered cause of shear banding, with the proposed mechanism that strain leading to temperature increase would give a viscosity drop, which then caused preferential deformation [41]. In current understanding, structural effects through STZ interaction are considered the leading cause, as not all shear bands operate hotly [85,86].

The actual magnitude of heating during shear band operation, before fracture itself, has been investigated by a series of techniques. As already mentioned, Argon calculated a temperature rise in a shear band with a 100 nm offset to be only 10^{-2}K, by assuming that the work done by shear was dissipated as heat over 1 ms [74]. Other theoretical approaches have assumed that elastically stored energy in the sample-machine spring system is released through the shear band during the stress drop of the shear event. This has resulted in an estimated heating of 1600-2000 K in the shear band core [80,87]. Sun *et al.* calculated only a 5 K increase when assuming that the shear band heat generation was dependent on their measured

displacement velocity, but acknowledged that the temperature might rise dramatically with higher local deformation rates [82].

Finite Element Models (FEMs) have also been used to analyze temperature evolution. Battezzati and Baldessin proposed an initial rise of about 1200 K, but a quick decrease back to below T_g within 50 ns, by assuming that shearing itself happens at roughly the speed of sound, with the whole event taking less than 12 ns [88]. Bazlov *et al.* also used FEM to study the hot-zone around the shear band, but although acknowledging the possibility of short-lived super-T_g temperatures, set the initial shear band temperature to 423 K [89].

Yokoyama *et al.* used back-calculations from shear band viscosity to estimate operating temperature. By first measuring the temperature dependence of viscosity for their selected alloy, and fitting it to the Vogel-Fulcher-Tammann equation, they estimated operating temperatures of 850 K based on observed stress and deformation rate in the shear band [21].

Traditional experimental approaches are limited either in their spatial or temporal resolution, making it difficult to fully understand the underlying mechanism of heating. The simple attachment of a thermocouple to a sample during testing has shown temperature rises, but only in the range of 1 K. Although the data acquisition rate was 50 kHz, measurements are taken at a distance from the shear band, well after thermal diffusion becomes significant [89].

Similarly, infrared thermography using high speed cameras has been applied [90]. This technique is also limited in spatial resolution to hot-zones on the order of 10 µm, three orders of magnitude larger than the shear band thickness during operation [75]. Temperature rise in the range of 1-6 K are typical findings for shear events during compression testing [78,91,92].

An interesting way of analyzing the heat generation post-mortem was used by Lewandowski and Greer, when they coated a bend test sample in ~100 nm diameter islands of tin. SEM investigation after the bend test, showed molten beads of tin along the surfacing shear bands, indicating temperature rise exceeding 207 K to melt the tin along a 400-2000 nm hot-zone surrounding the shear band. Taking the actual heat generation to be instantaneous, they estimated an upper initial temperature bound of 3600-8600 K [83]. The same method was later applied by different groups [93], but Ketov and Louzguine were only able to find indications of molten coating at intersections of several shear bands, surface cracks and along the final fracture plane, even when coating with Rose metal, which melts at 373 K [94]. Similarly Slaughter *et al.* also reported melting only along the final fracture [86]. Zhang *et al.* proposed a linear relationship between heating and shear displacement, meaning only shear steps of a certain size would generate enough heat for melting the coating [95].

While various experiments on the heat generation of shear bands during their propagation show widely different magnitudes of temperature rise, the post-failure fracture surface typically shows distinctive traces of fully molten material. This morphology will be discussed further in the following.

4.4 Fracture Morphology

Final fracture in BMGs typically happens along single[41], or at the intersection of a few [20,23], shear bands present in a specimen at failure. Common for both compressive [81] and tensile [23] fracture surfaces is a clear separation into two distinct zones. Along one edge there

is a smooth, featureless area, with a distinct boundary to a second area covered by raised veins [96]. Importantly, the veins are symmetrical but raised on both opposing fracture surfaces. On a compressive fracture surface, the veins form a series of cells, oriented along the shear direction, while tensile surfaces typically show veins radiating out from several nucleating cores [76]. An example of a tensile fracture morphology can be seen in Figure 4.2 a), where some radial veins are marked by arrows. The featureless area, marked by the dotted square is enlarged in Figure 4.2 b).

Leamy *et al.* were among the first to examine tensile fracture surfaces, once samples of sufficient size for testing could be produced [96]. They pointed out that the smooth, featureless section of the surface was the trace of shear sliding along the shear band prior to final fracture. The original understanding of the vein pattern included a propagating crack tip heating the material in front of itself. The temperature increase would give the material sufficient ductility to deform by localized necking, leaving vein-like traces. Pampillo and Reimschuessel continued this line of thought, but also mentioned the similarity to the morphology of the Taylor-instability [97].

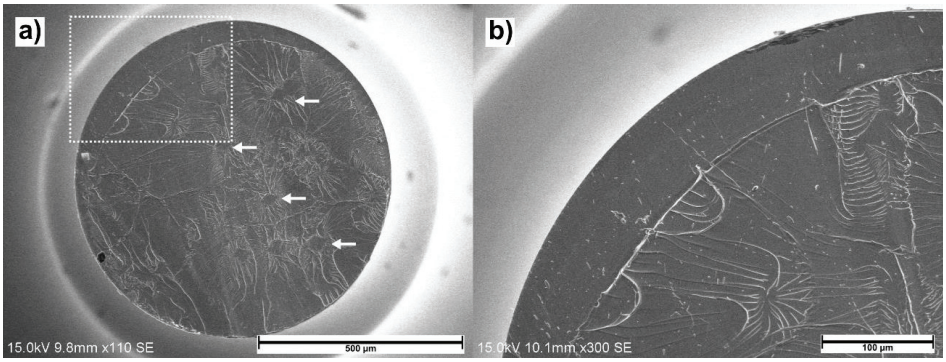

Figure 4.2: Fracture morphology in a $Zr_{70}Ni_{16}Cu_6Al_8$ tensile specimen. An overview is shown in a) with arrows pointing to some cavitation cores with outwardly radiating veins. The area marked by a dotted square is enlarged in b), showing the featureless sliding zone.

The Taylor-instability is an effect where a fluid penetrating into a more viscous fluid propagates along narrow fingers rather than as a single, unified front [84]. Argon and Salama further investigated this possibility, and showed that the observed veined structure fits well with separation of a fluid meniscus along propagating fingers [98]. This process, where fracture happens along a liquid layer intersecting the specimen, is the currently accepted explanation of the vein pattern on BMG fracture surfaces, and is called Saffman-Taylor fingering [41].

It is important to note that the liquid layer thickness far exceeds that of a shear band. Whereas an operating shear band is estimated to be on the order of 10 nm thick, the liquid layer evidenced by the vein patterning should be on the order of 0.1 to 1 µm [75]. The liquid layer thickness is among the factors which determine the distance between ridges in the surface [75], along with the viscosity of the layer [99].

4.5 Viscosity

Understanding the viscosity of metallic glasses in various states is important for understanding their fracture morphology. Based on observations of seemingly molten material covering the fracture surfaces, as well as the release of sparks at the fracture itself, it is typically believed that high temperatures are involved in the final failure of the materials [41]. To be able to form the observed surface features, a layer of 100-1000 nm [75] has to reach well above T_g. The development of this liquid layer from a 10 nm thick shear within a very short timeframe during fracture is also not well understood.

Equilibrium viscosity measurements have been used to calculate internal shear band temperature during sliding [21], based on deformation rate, stress and measured shear band thickness. The estimations found the temperature inside the operating shear band of 15 nm to be well above T_g. These calculations for use during fracture are, however, challenged by the dependence of viscosity of metallic glasses on both temperature and stress state [100].

It can be assumed that T_g acts as a minimum temperature for viscous deformation to commence. However, flash-DSC (Differential Scanning Calorimetry) results have shown that T_g itself is heavily dependent on heating rate. For experiments with heating rates from 0.083 to 8000 Ks^{-1}, Bai *et al.* found an increase in T_g of approximately 70 K [101]. Heating rates up to 40 000 Ks^{-1} have similarly been found to increase T_g by more than 100 K for melt spun ribbons [102]. If the change in viscosity for the whole liquid fracture layer of 100-1000 nm thickness is temperature driven, heating rates will have to be extremely high. Since melting temperatures seem to be relatively stable with varying heating rate [101], it is conceivable that T_g approaches equilibrium melting, and that this becomes the limiting temperature for Saffmann-Taylor fingering on fracture surfaces.

Once viscous flow starts, however, Khonik *et al.* showed that shear viscosity drops rapidly with increased heating rate. They found a two order of magnitude drop in viscosity when increasing heating rate by a factor of 330, from 0.3 Ks^{-1} to 100 Ks^{-1} [103]. This means that the viscosity gradient between the liquid layer and the solid bulk can be very high, consistent with the seemingly sharp boundary of the layer. Viscosity of supercooled liquids is also strain-rate dependent, with higher deformation rate reducing viscosity [12]. Assuming the strain rate is highest in the core of the shear band, this effect can further add to the viscosity gradient, localizing deformation.

To better understand the localized temperature rise in the shear band, an in-situ analysis of cryogen boiling on the sample surface during deformation was applied, as explained in Section 5.1.1. Evaporation of LN2 on the sample surface is used to quantify heat released from the shear band. Some basic concepts in bubble nucleation, boiling and heat transfer will therefore be discussed in the following Section 4.6.

4.6 Heat Transfer in Liquid Nitrogen

The nucleation of bubbles in liquid is limited by the work done to generate new surface, as well as to displace the corresponding volume of liquid. Due to this, nucleation does not happen until a certain superheat above the boiling point is reached [104]. Bubbles start to form spontaneously in the bulk of the liquid at the homogeneous nucleation temperature, below which boiling occurs at favourable nucleation sites. The exact superheat required for boiling

incipience on a surface is dependent on heat flux, nucleation site geometry and surface chemistry [105,106]. When a sample wall is supplying the heat, the optimal nucleation cavity size is typically in the range of 100-1000 μm [106]. With departure from this size range, and with increasing heat flux, boiling incipience is pushed toward the homogeneous nucleation temperature, which in the case of nitrogen is 105 K, 28 K above the boiling point [105]. Depending on the superheat, the characteristics of bubble nucleation will change. At low heat flux or superheat, bubbles generate by nucleate boiling, *i.e.* they nucleate, grow and release individually. At higher fluxes and superheats, the film boiling regime is entered, where a vapour film covers the entire heated surface, actually reducing heat transfer [105,107].

Heat removal from the wall happens through both convection and evaporation, assuming the latter to be the most significant in the case of boiling on the shear band surface, a minimum amount of heat removed can be estimated simply by multiplying the amount of gas generated with its heat of vaporization ($\Delta H_{vap} = 5.57\ kJ/mol$ for nitrogen [108]).

5 Paper 2 – Localized Heating

5.1 Methods

5.1.1 Video Analysis

Videos of the tensile tests performed at 77 K, as described in Sections 3.1.4 and 3.1.5, were further studied to measure heat consumption by boiling along the shear band surface during plastic deformation. Boiling was observed on all samples that showed appreciable plastic deformation while submerged in LN2. However, one sample was selected for deeper analysis due to its correspondence of suitable camera framerate, strain rate and video quality. For this, Kinovea 0.8.15 software by Joan Charmant was used [109]. Figure 5.1 a) shows a single frame from the analyzed video. The horizontal green line at the bottom works as calibration, by measuring the known gauge area thickness of 0.8 mm (note that the display unit is in m, as mm was not supported by Kinovea 0.8.15, although the values were actually measured in mm). The other three lines measure the diameters of bubbles released at the time of the snapshot ± 2 ms. The diameter of all bubbles observed in the video was recorded, together with their respective timestamp at release from the surface.

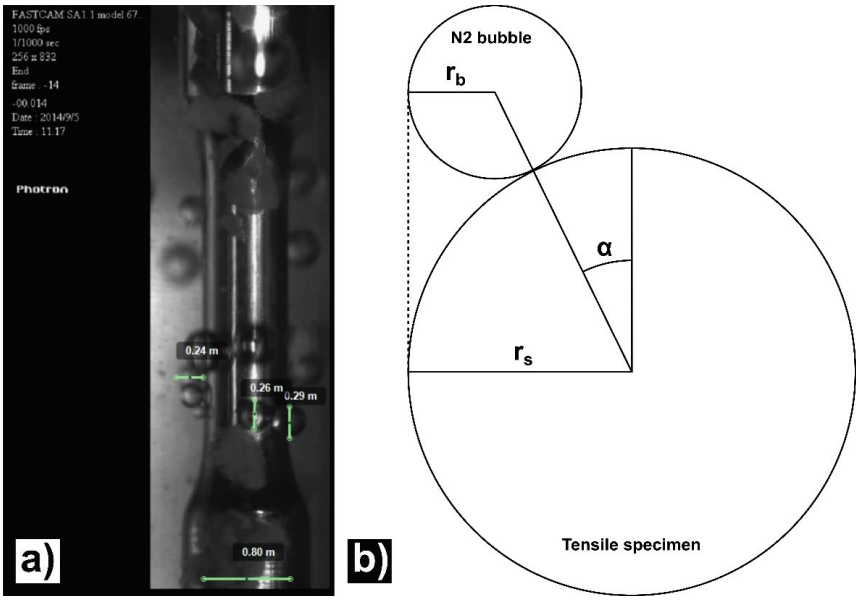

Figure 5.1: Snapshot of video analysis using Kinovea 0.8.15 software, a). The bottom line calibrates length scale using the known width of the gauge area, while the three upper lines measure bubble diameters at the time of release from the surface. In b), a schematic overview of the bubbles invisible to the camera is seen, with α marking the angular section obstructed from view.

A correction factor of 1.17 was used to account for bubbles not observable, due to obstruction from the sample itself. In Figure 5.1 b), α denotes the angular section of the specimen circumference, from which bubbles are unobservable. The proportion of unobservable bubbles, *k*, was calculated by Equation 5.1

Equation 5.1

$$k = \frac{\sin^{-1}\frac{r_s - r_b}{r_s + r_b}}{\pi}$$

where r_s is specimen radius and r_b is the average radius of the observed bubbles, as marked in Figure 5.1 b).

Once bubble volume was known, the number of evaporated gas molecules, *n*, was estimated by using the volume of a sphere and the ideal gas law,

Equation 5.2

$$n = \frac{4P\pi r^3}{3RT}$$

where *P* is internal bubble pressure, assumed atmospheric, *r* is bubble radius, *R* is the ideal gas constant, 8.314 $kg\ m^2\ s^{-2}\ K^{-1}\ mol^{-1}$, and *T* is temperature, set to 77 K. Total heat consumption was then calculated by multiplying the number of evaporated molecules by the heat of vaporization $\Delta H_{vap} = 5.57\ kJ/mol$ for N_2 [108].

5.1.2 Atomic Force Microscopy

Atomic Force Microscopy (AFM) was used to study the fracture morphology of the sample tested in tension. By measuring the deflection of a pointed cantilever, while dragging it across the sample surface, this technique supplies three-dimensional topographical data of the scanned area. Nine representative scans of 50x50 µm^2 areas were conducted across the sample surface. The selected areas are mapped out in Figure 5.2, where they are marked by white dotted squares overlaid on an SEM overview image. The AFM instrumentation used was an Agilent 5500 microscope.

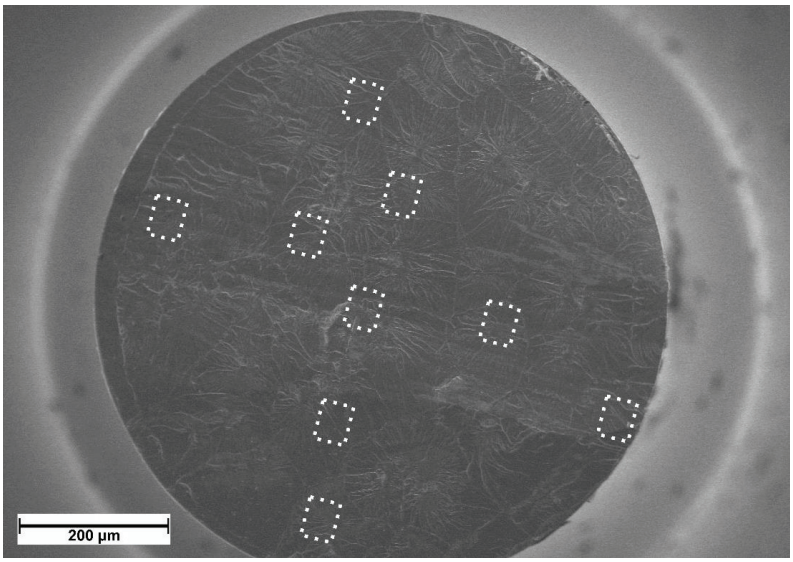

Figure 5.2: Areas scanned by AFM, mapped on an SEM fraction surface overview.

The AFM results were processed using Gwyddion 2.49 software [110] in order to measure the thickness of the liquid layer at fracture. An example of the processing steps is shown in Figure 5.3. The scanned sections, a), were first flattened by subtracting an automatically generated 11th degree polynomial (highest possible in the software). The remaining topography of the flattened area, seen in 3D in Figure 5.3 b) and top-down in c), was then taken to represent the entire liquid layer at fracture, in the form of Saffman-Taylor fingers. The most elevated 80 % of the surface, marked red in d), was spatially integrated to find the liquid layer volume. Liquid layer thickness then became available by dividing by the scanned area 50x50 µm^2.

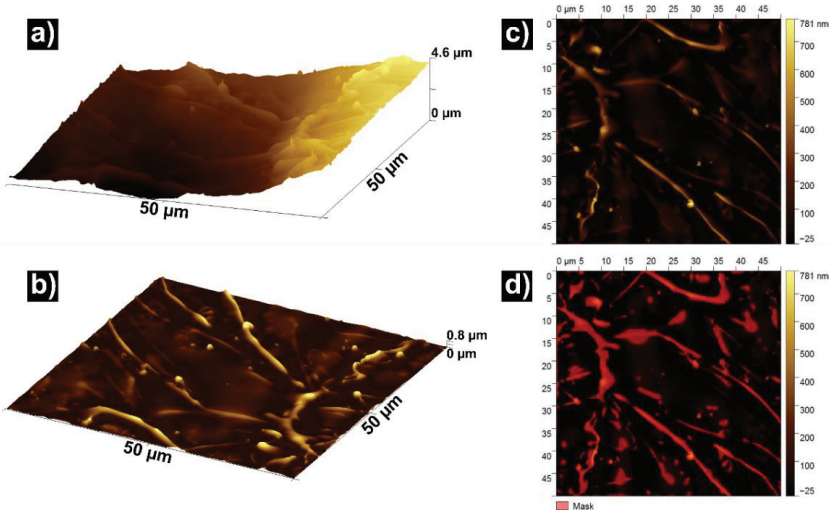

Figure 5.3: Liquid layer measuring process. The original scan, a), was flattened by background subtraction, b). The flattened surface is shown in a top-down view in c), on which a mask, marking the liquid layer, has been overlaid in d).

5.2 Summary of Paper

5.2.1 Introduction

This paper is entitled “Probing Heat Generation During Tensile Plastic Deformation of a Bulk Metallic Glass at Cryogenic Temperature,” published in Scientific Reports 8, Article number 16317 (2018) [111]. It consists of an in-depth analysis of a single sample from the dataset discussed in the paper “Tensile Properties of $Zr_{70}Ni_{16}Cu_6Al_8$ BMG at Room and Cryogenic Temperatures” [23], where localized boiling of the LN2 could be observed during measured plastic deformation. Heat release during deformation of the sample was estimated by measuring the size and frequency of the observed bubbles, adding nicely to a longstanding discussion on shear band temperatures [41,83,85] by applying a novel analytical technique.

5.2.2 Results

Analysis was done on the data recorded from a single tensile test performed in LN2 at nominal strain rate 10^{-2} s^{-1}. Boiling on the sample surface immediately preceding fracture was observed by the camera at 1000 Hz, as seen in Figure 5.4. The size of each bubble was measured at the time it released from the surface, and the volume of the bubbles at that time was used to calculate the number of evaporated gas molecules. This number was further used to estimate

the heat consumed through the enthalpy of vaporization. The resulting profile of accumulated heat consumption is presented in Figure 5.5, where it is overlaid with the corresponding stress-strain curve. A slight decrease in stress can be observed at the end of the stress-strain curve.

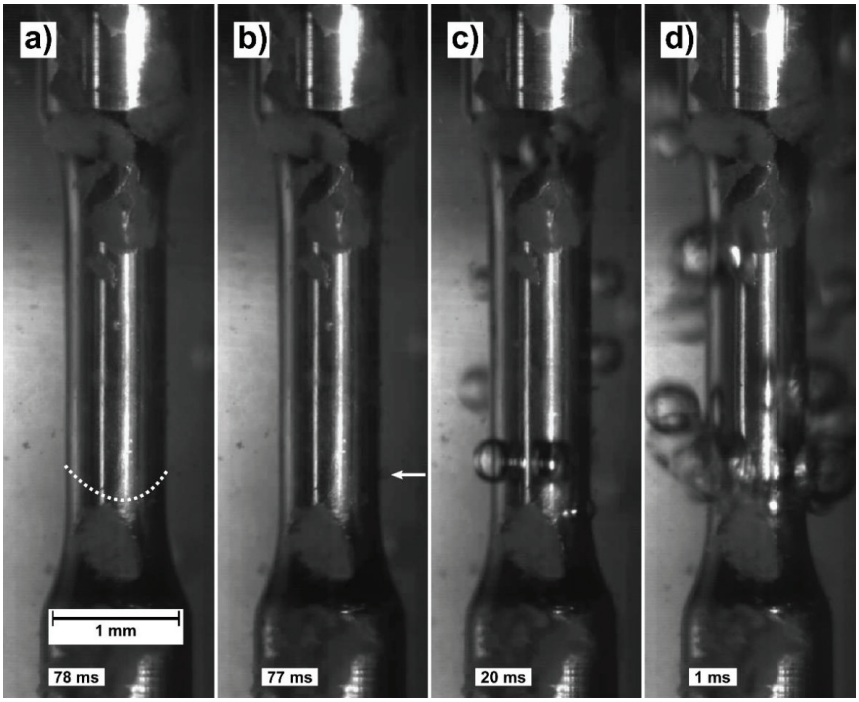

Figure 5.4: Images taken from the tensile testing during the last 78 ms of deformation. In a) the sample is seen prior to any boiling, while in b) the nucleation of the first bubble is marked by a white arrow. In c) and d), progressively more violent boiling is observed when approaching the time of fracture.

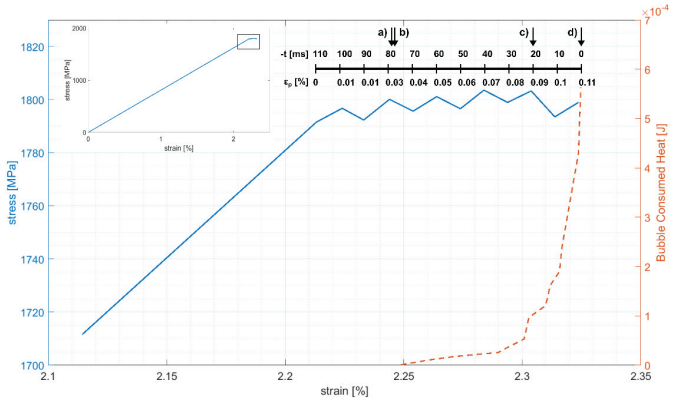

Figure 5.5: The plastic part of deformation, solid blue line, with the corresponding accumulated heat consumed by surface boiling, dashed red line. The inset shows the full stress-strain relationship, while the upper scale bar measures time before fracture and plastic deformation. The arrows denote the locations of snapshots shown in Figure 5.4.

Assuming that the primary shear band accommodates the full extent of plasticity, and accounting for its 54 ° angle to the tensile axis, the deformation corresponds to 4.3 µm in-plane sliding. In comparison, traces on the fracture surface observed with SEM in Figure 5.6, measure 28 µm sliding in the top-down projection, or 34.6 µm in-plane. From this the sliding deformation can be divided into two regimes, 4.3 µm "steady-state" shear over 110 ms, and 30.3 µm "runaway" shear over <1 ms.

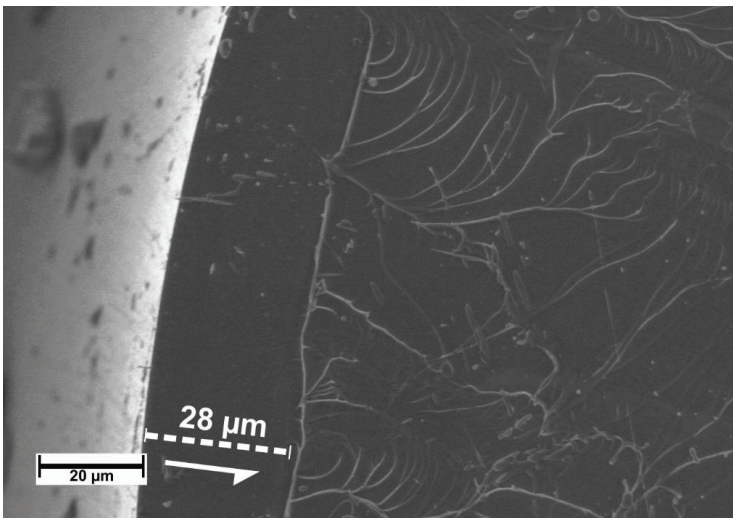

Figure 5.6: SEM image of the sliding traces on the fracture surface.

The sliding distances were used to calculate work done by the shear deformation. During steady-state shear, surface boiling consumed $5.6 \cdot 10^{-4}$ J equivalent to approximately 25 % of the work done by shear.

Investigation of the fracture surface showed that final rupture after runaway shear happened by simultaneous nucleation of voids by shear induced cavitation [112], spread over the surface. These cores grew into the liquid layer, driven by normal forces, until they connected to form a continuous pattern of rhombic cores and radial Saffman-Taylor fingers. The final thickness of the liquid layer was estimated by AFM to be 120 ± 40 nm.

5.2.3 Conclusion

Heat consumption by boiling was found to be $5.6 \cdot 10^{-4}$ J, which corresponds to 25 % of the calculated work done by shear sliding. The transition from observable steady-state shear to too-rapid-to-observe runaway shear was marked by a slight decrease in stress. Shear sliding developed into simultaneous fracture through shear induced cavitation at the end of runaway shear. The offset between measured plastic deformation and nucleation of bubbles indicates that the temperature increase is an effect of - rather than a cause for - shear banding.

5.2.4 Limitations

The procedure for analysis of boiling applied in this work was relatively simple in design. However, since the heat release calculation was not intended in the original experimental setup, which was simply tensile testing at various strain rates and temperatures, there are

some modifications that could have improved the quality of results. Firstly, a thermocouple added to the LN2 bath would have helped ensure that the boiling heat was indeed supplied only from the shear band and not from a potentially superheated liquid. Trying to arrest a sample during testing, to control that bubble nucleation stopped without further heat generation would also have achieved this.

A larger number of samples tested at the same camera framerate would also have been beneficial for the statistical robustness of the work.

The understanding of the steady-state to runaway shear transition could have been further improved by recording stress-strain data at an even higher frequency.

5.2.5 Further Work

The technique of the bubble sensor has several potential extensions and improvements: Submersion in other liquids or mixtures of liquids would allow analysis at other temperatures. The sensitivity of the sensor would also change with surface tension, heat of vaporization and homogeneous nucleation temperature of the liquid, allowing for further tuning. By mounting the sample horizontally or by using a two-camera setup, even better tracking of the bubbles could be achieved. A thermocouple submerged in the LN2 would also improve the reliability of the results, as it could quantify any uncertainty regarding LN2 superheat.

The AFM technique could also be significantly improved by scanning the entire fracture surface. The present setup did not have access to automatic scanning and stitching together of several scans. This is, however, available on some similar AFM machines and would give a better picture of the fracture surface. An interesting analysis would be to determine the liquid layer thickness profile over the entire surface, to allow study of fracture nucleation and progression, as well as liquid layer growth during fracture itself.

6 Design of Glassy Alloys

6.1 Glass Forming Ability

The Glass Forming Ability (GFA) of an alloy is a measure of the ease with which it can be turned into a glass. In developing practically applicable BMGs, the GFA is among the primary properties to optimize during design. Some common ways to measure GFA, as well as to predict it, are discussed in the following Sections 6.1.1 and 6.1.2.

6.1.1 Measures of GFA

Formation of a glass requires sufficiently fast cooling from the melt for crystallization to be bypassed. The critical cooling rate, R_c, is the minimum cooling rate which will produce a fully amorphous sample. For alloys discovered before 1990, R_c was typically in the range of 10^5 Ks^{-1}, allowing only very small specimens to be produced. Later research has reduced that requirement to the range of 10^{-1} Ks^{-1} for several BMG systems [12]. R_c is one of the measures used to quantify GFA [113,114].

The achievable cooling rate inside a real sample is dependent on several external factors such as thermal conductivity, section geometry, cooling medium *etc.* Therefore, R_c as a measurement of GFA is somewhat remote from practical applicability. Another commonly used parameter, the critical diameter, D_c, is often used to describe GFA instead [6,114]. D_c describes the maximum diameter of a cast cylinder, which can be obtained in a fully vitrified state. The minimum D_c for a sample to be considered "bulk," and hence qualify the given alloy as a BMG, is often cited as 1 mm [12]. While D_c is an experimentally relatable value, it is also more sensitive to individual variations in casting procedures and equipment than R_c, which is more material specific. The currently largest reported D_c value is 72 mm, which was achieved in the $Pd_{40}Cu_{30}Ni_{10}P_{20}$ alloy by cleaning the melt from potentially nucleating impurities with a B_2O_3 flux [32,115].

Both R_c and D_c act as measurements to compare the GFA of various alloys after production. In the upcoming Section 6.1.2, various important indicators predicting high GFA will be discussed.

6.1.2 Indicators of GFA

Turnbull posed the important question "Under what conditions can a glass be formed?" in his classic, homonymous paper of 1969 [1]. He argued, that to suppress crystallization, a high ratio of T_g to the liquidus temperature, T_l, should be beneficial. The implication is that if the liquid is stable at a temperature close to where atomic rearrangement into crystals no longer occurs on an experimental timescale, this temperature gap could be traversed easily during cooling to avoid crystallization. This ratio, $T_{rg}=T_g/T_l$, is called the reduced glass transition temperature, and is among the primarily used indicators of good GFA. With T_{rg} values above 2/3, Turnbull argued that the glassy state is sufficiently favored to only allow crystallization within a very limited undercooling range from the melt [1]. Some publications also define T_{rg} as $T_{rg}=T_g/T_s$, where T_s is the solidus temperature, but this has been shown to have a weaker, although still existent, correlation with GFA [114,116]. The difference in correlation to GFA between the two definitions of T_{rg} has been attributed to T_l having a stronger compositional dependence than T_s [116].

Another important material value used for determining GFA is T_x, the crystallization temperature. This is the temperature at which, upon heating from the glassy state, crystallization occurs. Since crystallization is a kinetic phenomenon, T_x, like T_g, is dependent on heating rate during measurements. Therefore both the measured value and scanning rate are normally stated together. A typical scanning rate might be 20 $Kmin^{-1}$ [54]. Although all liquid present below T_s is technically supercooled, the range between T_g and T_x is referred to as the supercooled liquid region, ΔT_x. In this region, the supercooled liquid is stable within appreciable timeframes. A large ΔT_x has been shown to be a quite robust indicator of good GFA [12,113]. A wide ΔT_x implies that the supercooled liquid is highly stable against crystallization, making processing into the amorphous state relatively easy.

Several parameters similar to T_{rg} and ΔT_x have been developed to indicate GFA. They include, but are not limited to $\alpha=T_x/T_l$, $T_{rx}=T_x/T_s$, $\gamma=T_x/(T_g+T_l)$ and $K_{gl}=(T_x-T_g)/(T_m-T_x)$ [15,113].

Alternatively to thermodynamic phenomena, the viscosity of the melt has been used to predict GFA. Angell proposed the categorization of liquids by their thermal dependence of viscosities [117]. Liquids with an Arrhenius-like behavior are called “strong” liquids, with deviating liquids called “fragile.” The fragility of a liquid is summarized in the fragility parameter, m, which ranges from strong at m=~10 to fragile at m=~200. m is defined as

Equation 6.1

$$m = \left. \frac{d\ \log_{10} < \tau >}{d(\frac{T_g}{T})} \right|_{T=T_g}$$

where $<\tau>$ is the average relaxation time [118].

A stronger behavior correlates well with higher GFA [119,120]. These liquids will have a higher viscosity at their melting temperature, and therefore limited diffusivity, effectively kinetically hindering crystallization and facilitating vitrification.

Johnson *et al.* analyzed GFA values of around 40 BMGs where high quality data on both viscosity and thermodynamics was available [6]. Surprisingly, they found that m and T_{rg} values for the set of BMGs are almost completely independent of each other. While each of the indicators is useful individually, a correlation on the form $log(D_c^2)=\Lambda_t T_{rg}+\Lambda_m m$, where Λ_t and Λ_m are fitting constants with values 25.6 and 0.0481 respectively, was found to predict GFA to within the experimental error of the dataset.

A more fundamental approach to GFA has been through the analysis of atomic-level structure in the BMGs. The ECP model, previously introduced in Section 4.1, by Miracle [63], was originally conceived as a descriptive model which fit well with previous data. Through later extensions and modifications [65], the model was also shown to have some predictive capabilities by optimizing solute-solvent size and compositional ratios for high packing efficiency [66]. The degree of structural ordering of a supercooled liquid, and its similarity to the structure in the corresponding glass, has also been directly linked to the viscosity of the melt in this temperature region [121].

The topological approach to GFA has also been handled without building an entire structural model. Egami and Waseda found that the solute concentration required for GFA in a binary system was dependent on atomic volume mismatch of the constituent atoms [27]. By linking the observed mismatch to structural stresses which destabilize the corresponding crystal structure, they developed the atomic mismatch factor $\lambda=c^B[(r_B/r_A)^3-1]$, where c^B is the concentration of solute B in solvent A and r_A and r_B the respective atomic radii of A and B. Practical GFA was found for $\lambda\geq0.1$, giving an expression for the minimum solute concentration in the alloys tested. This approach was later extended to multicomponent systems [28]. The optimal solute concentration for high GFA has been shown experimentally to be at $\lambda=0.18$, with the analytical explanation that this represents the highest density available in a close random packed structure, which coincides with the lowest atomic mobility [122].

In the early search for BMGs, Inoue introduced three empirical rules to guide in which systems high GFA would be expected [12,123]: "(1) multicomponent systems consisting of more than three elements; (2) significant difference in atomic size ratios above about 12 % among the three main constituent elements; and (3) negative heats of mixing among the three main constituent elements." Although these criteria do not pinpoint exact alloy compositions in the way that some of the other criteria do, they combine features from several of them. Criteria (1) and (2) combine into the same analytical approach as the ECP model and the λ factor, by promoting a dense structure with low mobility. Criterion (3) promotes chemical stabilization of the liquid, by discouraging diffusion of atoms into crystalline positions. This helps depressing the melting temperature, thereby increasing T_{rg} [124].

It is evident from the preceding discussion that information on liquid stability and melting temperatures is highly important in the design of BMGs. A major challenge is therefore the lack of complete thermodynamic evaluations of all potentially glass forming systems. One approach to solving this is through the CALPHAD (CALculation of PHAse Diagrams) method, which will be briefly introduced in the upcoming Section 6.2.

6.2 CALPHAD

The CALPHAD method is a framework for the "computer coupling of phase diagrams and thermochemistry" [125]. Based on experimental assessments of phase equilibria in single-, two- and multicomponent systems, this method calculates the Gibbs free energies of all potential phases at a composition for a given set of conditions. The comparative energies are used to evaluate the relative stability of the phases, and suggest which phases are most likely to be present [126]. The stabilities are calculated based on factors like temperature, composition, molar volume, pressure and magnetic properties [26]. Experimental data for binary compositions can be extrapolated to ternary systems, which then only require a limited amount of experiments to be verified and corrected. Binary and ternary systems in combination can then be further extrapolated into higher order systems, which actually require less experimental verification as very few stochiometric phases in metallic systems include more than three elements [26].

The assessed thermodynamic descriptions of various systems are contained within thermodynamic databases. Such databases typically contain datasets specialized for certain applications, like steelmaking, soldering or light metals [127]. Depending on the described

systems, the databases might be available free of charge [128], through scientific journal subscriptions [129] or commercially [130,131].

Given the availability of appropriate databases, the CALPHAD method can be a valuable tool in predicting high-GFA compositions through T_{rg} optimization by searching for low T_l areas prior to experimental work. Other thermodynamic approaches have involved comparing modeled driving forces for crystallization and vitrification to find areas where GFA is highest [132,133].

For the present work, Fe-based alloys were chosen as the subject of predictive modeling. These BMGs are attractive due to their already established use as industrial materials. Further, the relevant thermodynamic data is available through the TCFE7 database [134] for the Thermo-Calc software [135], which was applied in this work. The Fe-based family of metallic glasses is introduced in more detailed in the following Section 6.3.

6.3 Fe-Based Metallic Glasses

The first Fe-based metallic glasses were reported in 1967 by Duwez and Lin in the Fe-C-P system, with the approximate composition $Fe_{92.3}C_{1.7}P_6$ [136]. The soft ferromagnetic properties of the alloy were reported already in the first paper, paving the road for the most successful industrial application of metallic glasses so far, *i.e.* magnets for electrical and electronic applications like transformer cores and retail theft alarms [137]. These properties were commercialized within very few years, for instance in the form of soft magnetic ribbons by Metglas, Inc. in 1973 [138]. Amorphous metallic ribbons are also commonly used as precursors for nanocrystalline soft magnetic materials, which often show even better properties, *e.g.* FINEMET ($Fe_{73.5}Cu_1Nb_3Si_{13.5}B_9$) by Hitachi Metals, ltd [139]. Amorphous or nanocrystalline ferromagnetic alloys typically have better soft magnetic properties than their crystalline counterparts, with low coercivity (H_c), high permeability (μ) and high resistivity (ρ), with lower energy losses when switching magnetization [15,140]. A drawback to their application is a comparatively lower saturation magnetization (I_s), due to high metalloid content and antiferromagnetic coupling with some metallic alloying elements [141]. Another feature of the Fe-based BMG family is extremely high strength, such as the alloy $Fe_{71}Nb_6B_{23}$, with a compressive strength of 4.85 GPa and 1.6 % plasticity, although other BMGs in the family tend to be more brittle [24].

Fe-based metallic glasses were restricted to the sub-millimeter scale until 1995, when Inoue *et al.* reported cast rods with 1 mm diameter of the composition $Fe_{73}Al_5Ga_2P_{11}C_5B_4$ [142]. High GFA in the systems are generally obtained by a high number of constituent elements, combining both metals and metalloids [15]. The currently highest GFA was achieved by Shen *et al.* for the $Fe_{41}Co_7Cr_{15}Mo_{14}C_{15}B_6Y_2$ alloy, with D_c=16 mm [143].

Simpler, ternary BMG alloys have been reported more recently, in an attempt to facilitate production, better understand their structure and reduce dependence on high-cost alloying elements [137]. Ø=1-mm amorphous rods were reported at or around the composition $Fe_{72}M_6B_{22}$ for M= Sc, Y, Dy, Ho, or Er, while M=Nb or Zr were initially reported crystalline [141]. Successful production of BMGs in the Fe-P-C, Fe-Zr-B and Fe-Nb-B systems were later reported [25,137,144]. The latter system was the focus of the present work [54], and will therefore be introduced in more detail in the upcoming Section 6.3.1.

6.3.1 The Fe-Nb-B System

Inoue *et al.* first reported amorphous ribbons in the Fe-Nb-B system in 1981, in a study covering a series of binary and ternary Fe-based alloys [145]. Not until 2006 was there any report of BMGs in the system, when Stoica *et al.* produced Ø=1 mm amorphous rods of $Fe_{66}Nb_4B_{30}$ [25,146]. This alloy was produced by first fluxing the master alloy ingot in a B_2O_3 bath to remove impurities, before suction casting, see Section 7.1.2. The technique of fluxing has been shown to increase GFA in some systems by reducing heterogeneous nucleation sites in the melt [147,148]. Yao *et al.* later reported d_c=1.5 mm at $Fe_{71}Nb_6B_{23}$, with several surrounding alloys with d_c=1 mm, even without fluxing [144]. During compression testing, that alloy was found to possess extraordinary strength of 4.85 GPa, as well as some plastic deformability [24].

Various groups have studied the Fe-Nb-B system with regards to magnetic properties, generally finding good soft magnetism, but relatively low I_s [149–151]. The Curie temperature of the amorphous alloys has been found tunable, increasing with added B and decreasing with Nb [152], making it interesting for consideration in magnetocaloric applications [153]. Several structural studies have aimed at understanding the origins of both GFA, magnetic and mechanical properties in the system have been undertaken [154–156]. An improvement in soft magnetic properties has been found when using the amorphous alloy as a precursor for nanocrystallization [157–159]. This led to several groups deeply studying the crystallization behavior and products of various compositions [51,160–166]. It can also be noted that amorphous Fe-Nb-B thin films were found to have very promising magneto-optical properties [3].

7 Paper 3 – Predictive Modeling of Glass Forming Ability

7.1 Methods

7.1.1 Design

Good glass forming regions in the Fe-Nb-B alloying system were identified by searching for low T_l regions to maximize T_{rg} [1] as well as to optimize the topological influence on GFA by bringing the λ factor close to 0.18 (see Section 6.1.2) [122].

The CALPHAD method was applied to model the relevant phase diagram. Thermo-Calc software [135] was used with the TCFE7 database, to model the ternary Fe-Nb-B system for concentrations 0≤Nb≤10 and 0≤B≤30 in atomic percent. The standard TCFE7 database, designed for steelmaking, only has experimental evaluations for the binary Fe-B and Fe-Nb systems, and not the full ternary system. Suggested concentration limits are therefore 5 at.% Nb and only trace amounts of B [134]. An extra phase diagram, based on input data from a complete ternary assessment by Yoshitomi *et al.* [167], was therefore also generated using Thermo-Calc, and used for verification of the stock data.

The phase diagrams were overlaid with iso-λ lines, denoting topological favorability of glass formation. The necessary data on atomic radii, *i.e.* r_{Fe}=125 pm, r_{Nb}=143 pm and r_B=88 pm, was taken from work by Miracle *et al.* [168]

As the T_l values from TCFE7 were found unrealistic for the given composition space, the T_m based parameter, $T_{rg}=T_g/T_s$, was used to assess thermodynamic stability. This definition of T_{rg} has been shown to be a somewhat weaker, although still significant, predictor of GFA than the T_l based one [114,116].

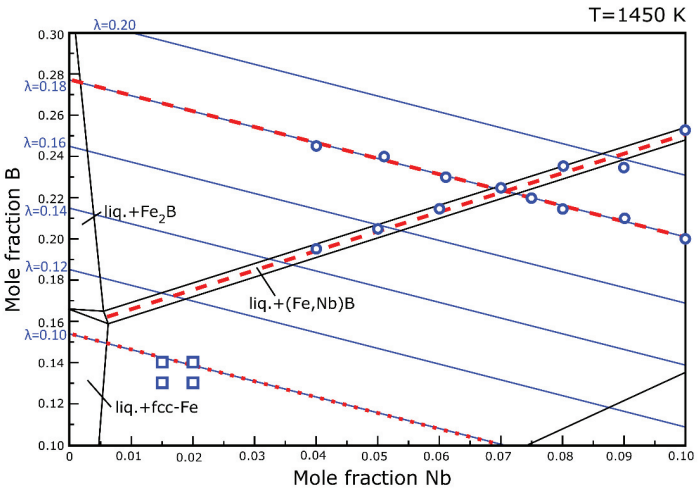

Figure 7.1: Isothermal plot of the modeled Fe-Nb-B ternary phase diagram at 1450 K, with iso- λ lines superimposed in blue, optimal GFA lines in dashed red and minimum λ for any GFA in dotted red. Alloys selected for testing are marked in blue squares for melt spinning and blue circles for 1 mm casting.

The isothermal section of the Fe-Nb-B phase diagram at 1450 K used for predicting GFA is shown in Figure 7.1, where iso-λ lines are marked in blue. The red dashed lines correspond to optimal GFA along the lowest T_s as well as λ=0.18, and the red dotted line marks λ=0.10, below which no GFA is expected. The compositions proposed for testing the model are marked as blue squares and blue circles for melt spinning and Ø=1 mm casting, respectively.

7.1.2 Suction Casting

Suction casting was used to produce Ø=1 mm rods of the reported Fe-Nb-B alloys. This is an extension of the arc melting technique, especially suitable for casting small geometries when high cooling rates are necessary. As illustrated in Figure 7.2, a pre-alloyed sample is melted by arc melting on top of the entrance to a casting mold. The sample is suspended on top of the small mold entrance even while molten due to surface tension. Once suitable temperature has been reached, a vacuum chamber below the mold is connected. A relative overpressure between the chamber and the mold is created, pushing the molten alloy into the mold cavity. This process allows for rapid filling of the mold before solidification occurs.

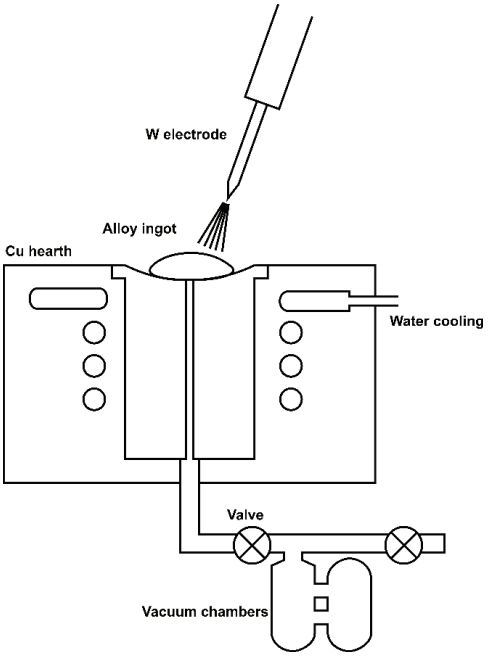

Figure 7.2: Schematic overview of the suction casting technique.

The suction casting equipment used in this project is an extension module of the Edmund Bühler MAM-1 arc melter, customized with an additional vacuum tank for extra capacity.

7.1.3 Melt Spinning

Fe-Nb-B ribbons were cast by melt spinning. In this technique, the precursor alloy is molten in a non-reactive crucible by induction heating. Once the alloy is molten, an overpressure is

applied inside the crucible, ejecting the melt through a nozzle at the bottom. The melt stream impinges on a rotating wheel, with a typical surface velocity of up to 40 ms^{-1}. This gives a rapidly solidified ribbon which is thrown in the spinning direction of the wheel and collected later from the chamber. An overview of the process in is shown in Figure 7.3.

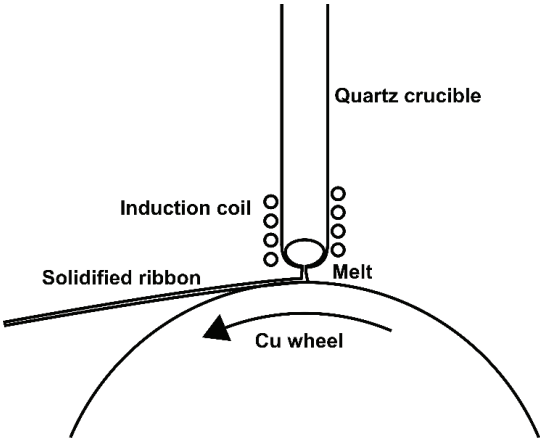

Figure 7.3: Schematic overview of the melt spinning techinque.

Fe-Nb-B ribbons were produced using a melt spinner. Quartz crucibles with round nozzles, Ø=0.8-1.2 mm, were used, and tangential surface velocity was set to 40 ms^{-1}.

7.1.4 Differential Scanning Calorimetry

Differential Scanning Calorimetry (DSC) was used for the estimation of thermodynamic data. T_g and T_x were measured for each sample during heating, as well as T_s and T_l during cooling, both at 20 Ks^{-1}. Figure 7.4 shows curves from a representative DSC scan. The small increase in heat capacity, seen in the green curve to the left (retrieved during heating) marks T_g, while the larger exothermal event is T_x. In the blue curve to the right (retrieved during cooling), T_l and T_s, located on either side of the exothermal solidification event, mark the beginning and end of solidification, respectively.

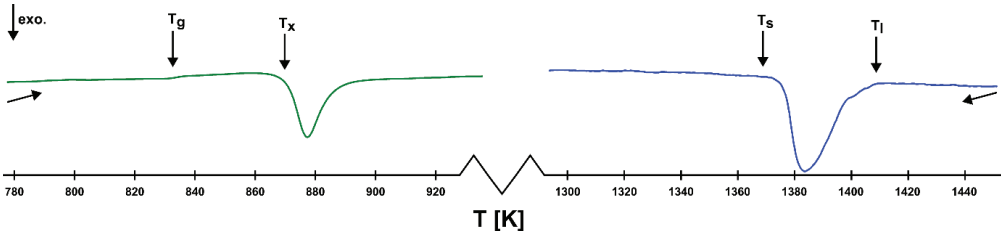

Figure 7.4: Representative DSC curves for a Fe-Nb-B glass.

A NETZSCH STA449 Jupiter machine was used for the DSC measurements, with a scanning rate of 20 Ks^{-1} under constant flow of Ar gas.

7.2 Summary of Paper

7.2.1 Introduction

An important approach to increased applicability of BMGs is reducing their design and production costs. It was therefore decided to test an approach to alloy design as part of the project. The paper is titled "*Predictive Modeling of Glass Forming Ability in the Fe-Nb-B System Using the CALPHAD Approach*", published in Journal of Alloys and Compounds, Volume 707, 15 June 2017, Pages 120-125 [54]. Attention was shifted from the original Zr-based alloy to the Fe-based alloys, due to their attractive combination of high strength, magnetic properties and relatively low materials cost [15,24]. The Fe-Nb-B system, specifically, was chosen due to being one of the few ternary Fe-based system to provide a bulk glass [25], allowing for comparison to literature data for model verification. Further, relevant thermodynamic data was readily available through the TCFE7 database [134], designed for steelmaking, for the Thermo-Calc software [135].

The alloy design is based on two indicators of good GFA, *i.e.* the λ-factor and T_{rg} [1,27,28]. Since it is known that T_l and T_s are more compositionally dependent than T_g [122], a good strategy for optimizing T_{rg} is to search for low-lying T_l or T_s areas. A challenge to this approach is the lack of experimental thermodynamic data for higher-order systems. The CALPHAD method was therefore tested as a way of "quickly" obtaining thermodynamic data of satisfactory quality to combine with the λ-factor in order to pinpoint potentially glass forming compositional areas.

A similar approach was recently successfully applied to the Ti-Fe-Si system by Zhao *et al.* [169], and a report on the Zr-Fe-Al system by Tabeshian *et al.* is currently in preparation [170].

7.2.2 Results

Thermo-Calc software [135] was used with the TCFE7 thermodynamic database [134] to model the Fe-Nb-B ternary system. An isothermal section at 1450 K in the Fe-rich area of the system was used to locate the lowest equilibrium T_s, for high GFA. The quality of the model from the commercially available database, which was used outside of its suggested compositional limits, was evaluated by comparing to a model based on thermodynamic data from literature [167]. The T_l values from the TCFE7 database were found unrealistic, while the location of the line of minimal T_s was offset by approximately 3 at. %. The T_s value was therefore considered of sufficient quality to be used for optimizing GFA. Iso-λ lines were superimposed on the phase diagram, in order to locate the intersection of lowest T_s and optimal λ=0.18.

14 selected compositions were cast into Ø=1 mm rods, while 4 compositions were cast into ribbons. Out of the produced alloys, XRD confirmed 7 bulk rods and 1 ribbon as amorphous. The locations of the amorphous samples agreed very well with the model, as seen in Figure 7.5.

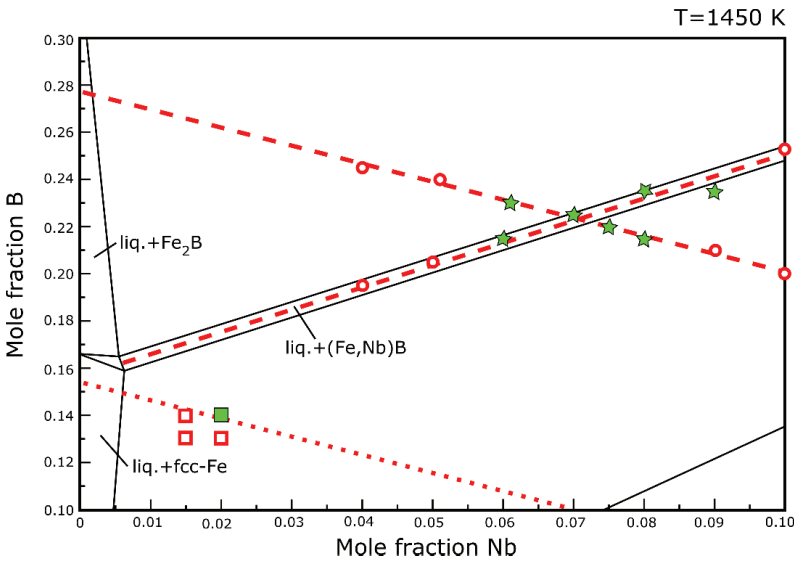

Figure 7.5: Summary of produced amorphous and crystalline alloys, marked on an 1450 K isothermal plot of the Fe-rich section of the Fe-Nb-B system. Red dashed lines mark optimal GFA by low T_s as well as λ=0.18, while the red dotted line marks λ=0.10, below which glass forming is not expected by melt spinning. Melt spun samples are represented as red open squares and green filled squares for crystalline and amorphous specimen. Suction cast rods are represented as red open circles and green filled stars for crystalline and amorphous samples respectively.

Furthermore, the produced alloys corresponded well with previous reports from literature. Stokłosa *et al.* reported a somewhat extended amorphous region by melt spinning compared to the present results [157], and Yao *et al.* some overlapping BMG, as well as some glasses that were slightly more Nb-poor [144]. The most Nb-rich alloy had not previously been reported in a glassy state.

7.2.3 Conclusion

A predictive model of GFA combining thermodynamic modeling through Thermo-Calc and topology was tested. Although there were some limitations to data in the commercial TCFE7 database, it was found sufficient to predict glass forming compositions in good agreement with experiments and literature.

7.2.4 Limitations

As already discussed, there are compositional limits to the databases available to the Thermo-Calc software. It was, however, shown that the model can still give valuable results outside its intended validity range, although more uncertainties are introduced. The λ-factor approach is also a relatively rough tool compared to the ECP model, which could possibly be implemented instead.

7.2.5 Further Work

An obvious extension to this work would be to perform mechanical and magnetic characterization on the produced alloys. Comparative analysis after varying heat treatment regimes and at various temperatures would increase the potential for real application of any of the produced alloys, by comparing them to previously reported ones.

The modeling approach itself also holds potential for extension. The TCFE7 database holds information on 22 alloying elements for Fe-based alloys. By combining this with atomic size data, a model could be made to quickly scan through all possible ternary and higher-order systems and propose any compositions with a favorable combination of T_s or T_l and λ-factor. Since Thermo-Calc allows the automation of such processes, higher order systems could also be scanned without the need to visualize phase diagrams in more than three dimensions. Comparison with literature could help validate proposed compositions. This approach would give a quick high-volume assessment of GFA in a wide range of Fe-based systems, as well as to help insure that the model works across other compositions.

If the degree of fit with the ECP model could be parameterized into a single parameter, similar to the λ factor, a model accounting even better for topology could be constructed.

8 Overall Conclusion

The motivation at the outset of the present project was to increase the practical applicability of BMGs through addressing two key limitations of the material class, *i.e.* their propensity for catastrophic failure in tension and the high cost of designing new alloys.

Through tensile testing at cryogenic temperatures, tensile brittleness is shown to indeed not be an unavoidable material characteristic, but something that is dependent on environmental factors. Both strengthening and ductilization at low temperature should make the materials an attractive selection for niche applications, such as demanding structural parts in refrigeration, cryogenic devices or for aerospace applications.

It is also established that the slow-down of shear band dynamics during cryogenic testing makes this an interesting environment for deeply studying the failure mechanics, in a way that has been unavailable at ambient temperature. This is important in the further understanding of BMG limitations and how to address them.

The successful prediction of a glass forming area in the Fe-Nb-B compositional space, using only data on atomic radii and a commercially available thermodynamic database, can help facilitate the further development of BMGs. Although limited by what databases are available and their precision, the technique allows for quick assessment and comparison of compositions before starting experimental trials. The periodic updates on available databases should also warrant periodic revisitations to the CALPHAD method for exploring GFA.

References

[1] D. Turnbull, Under What Conditions Can A Glass Be Formed?, Contemp. Phys. 10 (1969) 473–488. doi:10.1080/00107516908204405.

[2] M. Chen, A brief overview of bulk metallic glasses, NPG Asia Mater. 3 (2011) 82–90. doi:10.1038/asiamat.2011.30.

[3] A. Masood, T. Tamaki, V. Ström, A. Borgenstam, J. Ågren, K. V Rao, A New Class of Materials for Magneto-Optical Applications: Transparent Amorphous Thin Films of Fe-B-Nb and Fe-B-Nb-Y Metallic Glassy Alloys, IEEE Trans. Magn. 50 (2014). doi:10.1109/TMAG.2013.2290584.

[4] L. Krämer, Y. Champion, R. Pippan, From powders to bulk metallic glass composites, Sci. Rep. 7 (2017) 6651. doi:10.1038/s41598-017-06424-4.

[5] L. Krämer, K. Kormout, D. Setman, Y. Champion, R. Pippan, L. Krämer, K.S. Kormout, D. Setman, Y. Champion, R. Pippan, Production of Bulk Metallic Glasses by Severe Plastic Deformation, Metals (Basel). 5 (2015) 720–729. doi:10.3390/met5020720.

[6] W.L. Johnson, J.H. Na, M.D. Demetriou, Quantifying the origin of metallic glass formation, Nat. Commun. 7 (2016) 10313. doi:10.1038/ncomms10313.

[7] N. Stolen, Svein, Grande, Tor, Allan, Chemical Thermodynamics of Materials, J. Wiley, 2004. doi:10.1002/0470092688.

[8] W. Klement, R.H. Willens, P. Duwez, Non-crystalline structure in solidified Gold-Silicon alloys, Nature. 187 (1960) 869–870. doi:10.1038/187869b0.

[9] H. Jones, Rapid solidification of metals and alloys, Inst. Metall. Ix+ 83, A 5, Illus. (1982).

[10] A. Inoue, Bulk Glassy Alloys: Historical Development and Current Research, Engineering. 1 (2015) 185–191. doi:10.15302/J-ENG-2015038.

[11] A.L. Greer, E. Ma, Bulk Metallic Glasses: At the Cutting Edge of Metals Research, MRS Bull. 32 (2007) 611–619. doi:10.1557/mrs2007.121.

[12] A. Inoue, Stabilization of metallic supercooled liquid and bulk amorphous alloys, Acta Mater. 48 (2000) 279–306. doi:10.1016/S1359-6454(99)00300-6.

[13] A. Inoue, Stabilization of Metallic Supercooled Liquid, Acta Mater. 48 (2000) 279–306. doi:10.1016/S1359-6454(99)00300-6.

[14] M.F. Ashby, A.L. Greer, Metallic glasses as structural materials, Scr. Mater. 54 (2006) 321–326. doi:10.1016/j.scriptamat.2005.09.051.

[15] C. Suryanarayana, A. Inoue, Iron-based bulk metallic glasses, Int. Mater. Rev. 58 (2013) 131–166. doi:10.1179/1743280412Y.0000000007.

[16] M. Telford, The case for bulk metallic glass, Mater. Today. 7 (2004) 36–43. doi:10.1016/S1369-7021(04)00124-5.

[17] A.I. Salimon, M.F. Ashby, Y. Bréchet, A.L. Greer, Bulk metallic glasses: What are they good for?, Mater. Sci. Eng. A. 375–377 (2004) 385–388. doi:10.1016/j.msea.2003.10.167.

[18] Y. Yokoyama, K. Fujita, A.R. Yavari, A. Inoue, Malleable hypoeutectic zr-ni-cu-al bulk glassy alloys with tensile plastic elongation at room temperature, Philos. Mag. Lett. 89 (2009) 322–334. doi:10.1080/09500830902873575.

[19] Y. Yokoyama, H. Tokunaga, A.R. Yavari, T. Kawamata, T. Yamasaki, K. Fujita, K. Sugiyama, P.K. Liaw, A. Inoue, Tough Hypoeutectic Zr-Based Bulk Metallic Glasses, Metall. Mater. Trans. A. 42 (2011) 1468–1475. doi:10.1007/s11661-011-0631-1.

[20] H. Tokunaga, K. Fujita, Y. Yokoyama, Tensile Plastic Deformation Behavior of Zr70Ni16Cu6Al8 Bulk Metallic Glass at Cryogenic Temperature, Mater. Trans. 53 (2012) 1395–1399. doi:10.2320/matertrans.M2012102.

[21] Y. Yokoyama, H. Tokunaga, A.R. Yavari, M. Yamada, T. Yamasaki, K. Fujita, A. Inoue, Viscous flow in sliding shear band formed during tensile deformation of hypoeutectic Zr-based metallic glass, Intermetallics. 19 (2011) 1683–1687. doi:10.1016/j.intermet.2011.06.017.

[22] A. Kawashima, Y. Yokoyama, I. Seki, H. Kurishita, M. Fukuhara, H. Kimura, A. Inoue, Enhanced Tensile Strength and Plasticity of Zr-Cu-Al Bulk Glassy Alloys at Cryogenic Temperatures, Mater. Trans. 50 (2009) 2685–2690. doi:10.2320/matertrans.M2009186.

[23] D.D.E. Brennhaugen, K. Georgarakis, Y. Yokoyama, K.S. Nakayama, L. Arnberg, R.E. Aune, Tensile properties of Zr70Ni16Cu6Al8BMG at room and cryogenic temperatures, J. Alloys Compd. 742 (2018) 952–957. doi:10.1016/j.jallcom.2018.01.322.

[24] J.H. Yao, J.Q. Wang, Y. Li, Ductile Fe – Nb – B bulk metallic glass with ultrahigh strength, Appl. Phys. Lett. 92 (2008) 71–73. doi:10.1063/1.2949747.

[25] M. Stoica, K. Hajlaoui, A. Lemoulec, A.R. Yavari, New ternary Fe-based bulk metallic glass with high boron content, Philos. Mag. Lett. 86 (2006) 267–275. doi:10.1080/09500830600696344.

[26] U.R. Kattner, The thermodynamic modeling of multicomponent phase equilibria, JOM. 49 (1997) 14–19. doi:10.1007/s11837-997-0024-5.

[27] T. Egami, Y. Waseda, Atomic Size effect on the Glass Forming Ability of Metallic Alloys, J. Non. Cryst. Solids. 64 (1984) 113–134.

[28] R.D.S. Lisboa, C. Bolfarini, W.J. Botta, C.S. Kiminami, Topological instability as a criterion for design and selection of aluminum-based glass-former alloys, Cit. Appl. Phys. Lett. 86 (2005) 211904. doi:10.1063/1.1931047.

[29] M.M. Trexler, N.N. Thadhani, Mechanical properties of bulk metallic glasses, Prog. Mater. Sci. 55 (2010) 759–839. doi:10.1016/j.pmatsci.2010.04.002.

[30] A. Inoue, A. Takeuchi, Recent development and application products of bulk glassy alloys, Acta Mater. 59 (2011) 2243–2267. doi:10.1016/j.actamat.2010.11.027.

[31] H.K.D.H. Bhadeshia, S.R. Honeycombe, Steels: Microstructure and Properties, 3rd ed., Butterworth-Heinemann, 2006.

[32] A.L. Greer, Metallic glasses…on the threshold, Mater. Today. 12 (2009) 14–22. doi:10.1016/S1369-7021(09)70037-9.

[33] J.J. Fan, Y.F. Yan, S.H. Chen, C.H. Ng, F.F. Wu, K.C. Chan, Reliability of the plastic

deformation behavior of a Zr-based bulk metallic glass, Intermetallics. 74 (2016) 25–30. doi:10.1016/j.intermet.2016.05.001.

[34] W.L. Johnson, K. Samwer, A universal criterion for plastic yielding of metallic glasses with a (T/Tg)2/3 temperature dependence, Phys. Rev. Lett. 95 (2005) 195501. doi:10.1103/PhysRevLett.95.195501.

[35] A. Kawashima, K. Ohmura, Y. Yokoyama, A. Inoue, The corrosion behaviour of Zr-based bulk metallic glasses in 0.5 M NaCl solution, Corros. Sci. 53 (2011) 2778–2784. doi:10.1016/J.CORSCI.2011.05.014.

[36] A. Kawashima, Y. Yokoyama, A. Inoue, Zr-based bulk glassy alloy with improved resistance to stress corrosion cracking in sodium chloride solutions, Corros. Sci. 52 (2010) 2950–2957. doi:10.1016/J.CORSCI.2010.05.007.

[37] A. Tabeshian, D. Persson, L. Arnberg, R. Aune, Comparison of the electrochemical behavior of amorphous Zr55Cu30Ni5Al10, stainless steel (316LVM), and CoCrMo (F75) in simulated body fluid with and without addition of protein, Mater. Corros. (2018). doi:10.1002/maco.201810480.

[38] T.C. Hufnagel, C.A. Schuh, M.L. Falk, Deformation of metallic glasses: Recent developments in theory, simulations, and experiments, 2016. doi:10.1016/j.actamat.2016.01.049.

[39] R.D. Conner, H. Choi-Yim, W.L. Johnson, Mechanical properties of Zr 57 Nb 5 Al 10 Cu 15.4 Ni 12.6 metallic glass matrix particulate composites, (1999). https://authors.library.caltech.edu/28741/1/CONjmr99.pdf (accessed July 20, 2018).

[40] R. Maaß, D. Klaumünzer, E.I. Preiß, P.M. Derlet, J.F. Löffler, Single shear-band plasticity in a bulk metallic glass at cryogenic temperatures, Scr. Mater. 66 (2012) 231–234. doi:10.1016/j.scriptamat.2011.10.044.

[41] A.L. Greer, Y.Q. Cheng, E. Ma, Shear bands in metallic glasses, Mater. Sci. Eng. R Reports. 74 (2013) 71–132. doi:10.1016/j.mser.2013.04.001.

[42] K.S. Yoon, M. Lee, E. Fleury, J.C. Lee, Cryogenic temperature plasticity of a bulk amorphous alloy, Acta Mater. 58 (2010) 5295–5304. doi:10.1016/j.actamat.2010.06.002.

[43] A.R. Yavari, K. Georgarakis, W.J. Botta, A. Inoue, G. Vaughan, Homogenization of plastic deformation in metallic glass foils less than one micrometer thick, Phys. Rev. B - Condens. Matter Mater. Phys. 82 (2010) 172202. doi:10.1103/PhysRevB.82.172202.

[44] J. Schroers, Q. Pham, A. Desai, Thermoplastic Forming of Bulk Metallic Glass— A Technology for MEMS and Microstructure Fabrication, J. Microelectromechanical Syst. 16 (2007) 240–247. doi:10.1109/JMEMS.0007.892889.

[45] A. Good, Metallic Glass Gears Make for Graceful Robots, 2016. https://www.jpl.nasa.gov/news/news.php?feature=6684 (accessed July 16, 2018).

[46] D.C. Hofmann, G.S. Agnes, Bulk Metallic Glasses and Composites for Optical and Compliant Mechanisms, 2013. https://ntrs.nasa.gov/search.jsp?R=20140002307 (accessed July 24, 2018).

[47] H. Kobayashi, H. Onoue, Brittle fracture of Liberty Ships, n.d. http://www.shippai.org/fkd/en/cfen/CB1011020.html (accessed July 24, 2018).

[48] Y.H. Li, W. Zhang, C. Dong, A. Kawashima, A. Makino, P.K. Liaw, Effects of cryogenic temperatures on mechanical behavior of a Zr60Ni25Al15bulk metallic glass, Mater. Sci. Eng. A. 584 (2013) 7–13. doi:10.1016/j.msea.2013.06.063.

[49] M.Q. Jiang, G. Wilde, J.H. Chen, C.B. Qu, S.Y. Fu, F. Jiang, L.H. Dai, Cryogenic-temperature-induced transition from shear to dilatational failure in metallic glasses, Acta Mater. 77 (2014) 248–257. doi:10.1016/J.ACTAMAT.2014.05.052.

[50] D.D.E. Brennhaugen, Thermal Dependence of Shear Banding in Zr70Ni16Cu6Al8 Bulk Metallic Glasses, Institutt for materialteknologi, 2014. https://brage.bibsys.no/xmlui/handle/11250/249664 (accessed March 8, 2017).

[51] A. Makino, T. Bitoh, A. Inoue, T. Masumoto, Nb-Poor Fe–Nb–B nanocrystalline soft magnetic alloys with small amount of P and Cu prepared by melt-spinning in air, Scr. Mater. 48 (2003) 869–874. doi:10.1016/S1359-6462(02)00612-7.

[52] Y. Yokoyama, H. Fredriksson, H. Yasuda, M. Nishijima, A. Inoue, Glassy Solidification Criterion of Zr50Cu40Al10 Alloy, Mater. Trans. 48 (2007) 1363–1372. doi:10.2320/matertrans.MF200624.

[53] Y. Yokoyama, K. Inoue, K. Fukaura, Pseudo Float Melting State in Ladle Arc-Melt-Type Furnace for Preparing Crystalline Inclusion-Free Bulk Amorphous Alloy., Mater. Trans. 43 (2002) 2316–2319. doi:10.2320/matertrans.43.2316.

[54] D.D.E. Brennhaugen, H. Mao, D. V. Louzguine-Luzgin, L. Arnberg, R.E. Aune, Predictive modeling of glass forming ability in the Fe-Nb-B system using the CALPHAD approach, J. Alloys Compd. 707 (2017) 120–125. doi:10.1016/j.jallcom.2016.12.049.

[55] E. Fagerholt, Field measurements in mechanical testing using close-range photogrammetry and digital image analysis, Norwegian University of Science and Technology, 2012. http://folk.ntnu.no/egilf/Thesis_Egil_Fagerholt.pdf (accessed June 15, 2017).

[56] L.S. Huo, H.Y. Bai, X.K. Xi, D.W. Ding, D.Q. Zhao, W.H. Wang, R.J. Huang, L.F. Li, Tensile properties of ZrCu-based bulk metallic glasses at ambient and cryogenic temperatures, J. Non. Cryst. Solids. 357 (2011) 3088–3093. doi:10.1016/j.jnoncrysol.2011.04.017.

[57] J. Yi, S.M. Seifi, W. Wang, J.J. Lewandowski, A Damage-tolerant Bulk Metallic Glass at Liquid-nitrogen Temperature, J. Mater. Sci. Technol. 30 (2014) 627–630. doi:10.1016/j.jmst.2014.04.017.

[58] S. Roberts, C. Zachrisson, H. Kozachkov, A. Ullah, A.A. Shapiro, W.L. Johnson, D.C. Hofmann, Cryogenic Charpy impact testing of metallic glass matrix composites, Scr. Mater. 66 (2012) 284–287. doi:10.1016/j.scriptamat.2011.11.011.

[59] H. Tokunaga, J. Koyama, K. Fujita, Y. Yokoyama, T. Yamasaki, A. Inoue, Mechanisms of Tensile Plastic Deformation in Zr 70 Ni 16 Cu 6 Al 8 Bulk Metallic Glass, J. Japan Inst. Met. 75 (2011) 569–574. doi:10.2320/matertrans.M2012102.

[60] J.D. BERNAL, Geometry of the Structure of Monatomic Liquids, Nature. 185 (1960) 68–70. doi:10.1038/185068a0.

[61] M.H. Cohen, D. Turnbull, Molecular Transport in Liquids and Glasses, J. Chem. Phys. 31 (1959) 1164–1169. doi:10.1063/1.1730566.

[62] L. Zhong, J. Wang, H. Sheng, Z. Zhang, S.X. Mao, Formation of monatomic metallic glasses through ultrafast liquid quenching, Nature. 512 (2014) 177–180. doi:10.1038/nature13617.

[63] D.B. Miracle, A structural model for metallic glasses, Nat. Mater. 3 (2004) 697–702. doi:10.1038/nmat1219.

[64] D.B. Miracle, T. Egami, K.M. Flores, K.F. Kelton, Structural Aspects of Metallic Glasses, MRS Bull. 32 (2007) 629–634. doi:10.1557/mrs2007.124.

[65] D.B. Miracle, A Physical Model for Metallic Glass Structures: An Introduction and Update, JOM. 64 (2012) 846–855. doi:10.1007/s11837-012-0359-4.

[66] K.J. Laws, D.B. Miracle, M. Ferry, A predictive structural model for bulk metallic glasses, Nat. Commun. 6 (2015) 8123. doi:10.1038/ncomms9123.

[67] T.C. Hufnagel, S. Brennan, Short- and medium-range order in (Zr 70 Cu 20 Ni 10) 90 − x Ta x Al 10 bulk amorphous alloys, Phys. Rev. B. 67 (2003) 014203. doi:10.1103/PhysRevB.67.014203.

[68] L.Y. Chen, A.D. Setyawan, H. Kato, A. Inoue, G.Q. Zhang, J. Saida, X.D. Wang, Q.P. Cao, J.Z. Jiang, Free-volume-induced enhancement of plasticity in a monolithic bulk metallic glass at room temperature, Scr. Mater. 59 (2008) 75–78. doi:10.1016/J.SCRIPTAMAT.2008.02.025.

[69] F. Spaepen, Homogeneous flow of metallic glasses: A free volume perspective, Scr. Mater. 54 (2006) 363–367. doi:10.1016/j.scriptamat.2005.09.046.

[70] A.R. Yavari, A. Le Moulec, A. Inoue, N. Nishiyama, N. Lupu, E. Matsubara, W.J. Botta, G. Vaughan, M. Di Michiel, Å. Kvick, Excess free volume in metallic glasses measured by X-ray diffraction, Acta Mater. 53 (2005) 1611–1619. doi:10.1016/J.ACTAMAT.2004.12.011.

[71] S. V. Ketov, Y.H. Sun, S. Nachum, Z. Lu, A. Checchi, A.R. Beraldin, H.Y. Bai, W.H. Wang, D. V. Louzguine-Luzgin, M.A. Carpenter, A.L. Greer, Rejuvenation of metallic glasses by non-affine thermal strain, Nature. 524 (2015) 200–203. doi:10.1038/nature14674.

[72] W. Guo, R. Yamada, J. Saida, Rejuvenation and plasticization of metallic glass by deep cryogenic cycling treatment, Intermetallics. 93 (2018) 141–147. doi:10.1016/j.intermet.2017.11.015.

[73] F. Spaepen, A microscopic mechanism for steady state inhomogeneous flow in metallic glasses, Acta Metall. 25 (1977) 407–415. doi:10.1016/0001-6160(77)90232-2.

[74] A.S. Argon, Plastic deformation in metallic glasses, Acta Metall. 27 (1979) 47–58. doi:10.1016/0001-6160(79)90055-5.

[75] Y. Zhang, A.L. Greer, Thickness of shear bands in metallic glasses, Appl. Phys. Lett. 89 (2006) 071907. doi:10.1063/1.2336598.

[76] Z.F. Zhang, J. Eckert, L. Schultz, Difference in compressive and tensile fracture mechanisms of Zr59Cu20Al10Ni8Ti3bulk metallic glass, Acta Mater. 51 (2003) 1167–

1179. doi:10.1016/S1359-6454(02)00521-9.

[77] H. Neuhäuser, Rate of shear band formation in metallic glasses, Scr. Metall. 12 (1978) 471–474. doi:10.1016/0036-9748(78)90260-0.

[78] P. Thurnheer, F. Haag, J.F. Löffler, Time-resolved measurement of shear-band temperature during serrated flow in a Zr-based metallic glass, Acta Mater. 115 (2016) 468–474. doi:10.1016/j.actamat.2016.05.008.

[79] D.B. Miracle, A. Concustell, Y. Zhang, A.R. Yavari, A.L. Greer, Shear bands in metallic glasses: Size effects on thermal profiles, Acta Mater. 59 (2011) 2831–2840. doi:10.1016/j.actamat.2011.01.022.

[80] K. Georgarakis, M. Aljerf, Y. Li, A. Lemoulec, F. Charlot, A.R. Yavari, K. Chornokhvostenko, E. Tabachnikova, G.A. Evangelakis, D.B. Miracle, A.L. Greer, T. Zhang, Shear band melting and serrated flow in metallic glasses, Appl. Phys. Lett. 93 (2008) 031907. doi:10.1063/1.2956666.

[81] B.A. Sun, S. Pauly, J. Tan, M. Stoica, W.H. Wang, U. Kühn, J. Eckert, Serrated flow and stick-slip deformation dynamics in the presence of shear-band interactions for a Zr-based metallic glass, Acta Mater. 60 (2012) 4160–4171. doi:10.1016/j.actamat.2012.04.013.

[82] B.A. Sun, Y. Yang, W.H. Wang, C.T. Liu, The Critical Criterion on Runaway Shear Banding in Metallic Glasses, Sci. Rep. 6 (2016) 21388. doi:10.1038/srep21388.

[83] J.J. Lewandowski, A.L. Greer, Temperature rise at shear bands in metallic glasses, Nat. Mater. 5 (2006) 15–18. doi:10.1038/nmat1536.

[84] P.G. Saffman, G. Taylor, The Penetration of a Fluid into a Porous Medium or Hele-Shaw Cell Containing a More Viscous Liquid, Proc. R. Soc. A Math. Phys. Eng. Sci. 245 (1958) 312–329. doi:10.1098/rspa.1958.0085.

[85] F. Spaepen, Metallic glasses: Must shear bands be hot?, Nat. Mater. 5 (2006) 7–8. doi:10.1038/nmat1552.

[86] S.K. Slaughter, F. Kertis, E. Deda, X. Gu, W.J. Wright, T.C. Hufnagel, Shear bands in metallic glasses are not necessarily hot, APL Mater. 2 (2014) 096110. doi:10.1063/1.4895605.

[87] J.G. Wang, Y. Pan, S.X. Song, B.A. Sun, G. Wang, Q.J. Zhai, K.C. Chan, W.H. Wang, How hot is a shear band in a metallic glass?, Mater. Sci. Eng. A. 651 (2016) 321–331. doi:10.1016/j.msea.2015.10.125.

[88] L. Battezzati, D. Baldissin, Quantitative evaluation of lengthscales for temperature rise in shear bands and for failure of metallic glasses, Scr. Mater. 59 (2008) 223–226. doi:10.1016/j.scriptamat.2008.03.016.

[89] A.I. Bazlov, A.Y. Churyumov, M. Buchet, D. V. Louzguine-Luzgin, On Temperature Rise Within the Shear Bands in Bulk Metallic Glasses, Met. Mater. Int. 24 (2018) 481–488. doi:10.1007/s12540-018-0072-0.

[90] G. Wang, Q. Feng, B. Yang, W. Jiang, P.K. Liaw, C.T. Liu, Thermographic studies of temperature evolutions in bulk metallic glasses: An overview, Intermetallics. 30 (2012)

1–11. doi:10.1016/j.intermet.2012.03.022.

[91] W.H. Jiang, H.H. Liao, F.X. Liu, H. Choo, P.K. Liaw, Rate-dependent temperature increases in shear bands of a bulk-metallic glass, Metall. Mater. Trans. A Phys. Metall. Mater. Sci. 39 (2008) 1822–1830. doi:10.1007/s11661-007-9321-4.

[92] B. Yang, P.K. Liaw, G. Wang, M. Morrison, C.T. Liu, R.A. Buchanan, Y. Yokoyama, In-situ thermographic observation of mechanical damage in bulk-metallic glasses during fatigue and tensile experiments, Intermetallics. 12 (2004) 1265–1274. doi:10.1016/j.intermet.2004.04.006.

[93] R.T. Qu, S.G. Wang, G.J. Li, R.F. Wang, X.D. Wang, S.J. Wu, Z.F. Zhang, Shear band fracture in metallic glass: Hot or cold?, Scr. Mater. 162 (2019) 136–140. doi:10.1016/J.SCRIPTAMAT.2018.11.003.

[94] S. V. Ketov, D. V. Louzguine-Luzgin, Localized shear deformation and softening of bulk metallic glass: Stress or temperature driven?, Sci. Rep. 3 (2013) 2798. doi:10.1038/srep02798.

[95] Y. Zhang, N.A. Stelmashenko, Z.H. Barber, W.H. Wang, J.J. Lewandowski, A.L. Greer, Local temperature rises during mechanical testing of metallic glasses, J. Mater. Res. 22 (2007) 419–427. doi:10.1557/jmr.2007.0068.

[96] H.J. Leamy, T.T. Wang, H.S. Chen, Plastic flow and fracture of metallic glass, Metall. Trans. 3 (1972) 699–708. doi:10.1007/BF02642754.

[97] C.A. Pampillo, A.C. Reimschuessel, The fracture topography of metallic glasses, J. Mater. Sci. 9 (1974) 718–724. doi:10.1007/BF00761791.

[98] A.S. Argon, M. Salama, The mechanism of fracture in glassy materials capable of some inelastic deformation, Mater. Sci. Eng. 23 (1976) 219–230. doi:10.1016/0025-5416(76)90198-1.

[99] L.A. Deibler, J.J. Lewandowski, Model experiments to mimic fracture surface features in metallic glasses, Mater. Sci. Eng. A. 527 (2010) 2207–2213. doi:10.1016/j.msea.2009.10.072.

[100] P. Guan, M. Chen, T. Egami, Stress-temperature scaling for steady-state flow in metallic glasses, Phys. Rev. Lett. 104 (2010) 205701. doi:10.1103/PhysRevLett.104.205701.

[101] F.X. Bai, J.H. Yao, Y.X. Wang, J. Pan, Y. Li, Crystallization kinetics of an Au-based metallic glass upon ultrafast heating and cooling, Scr. Mater. 132 (2017) 58–62. doi:10.1016/j.scriptamat.2017.02.001.

[102] J.Q. Wang, N. Chen, P. Liu, Z. Wang, D. V. Louzguine-Luzgin, M.W. Chen, J.H. Perepezko, The ultrastable kinetic behavior of an Au-based nanoglass, Acta Mater. 79 (2014) 30–36. doi:10.1016/j.actamat.2014.07.015.

[103] V.A. Khonik, M. Ohta, K. Kitagawa, Heating rate dependence of the shear viscosity of a finemet glassy alloy, Scr. Mater. 45 (2001) 1393–1400. doi:10.1016/S1359-6462(01)01175-7.

[104] M. Blander, J.L. Katz, Bubble nucleation in liquids, AIChE J. 21 (1975) 833–848. doi:10.1002/aic.690210502.

[105] K. Okuyama, Y. Iida, Transient boiling heat transfer characteristics of nitrogen (bubble behavior and heat transfer rate at stepwise heat generation), Int. J. Heat Mass Transf. 33 (1990) 2065–2071. doi:10.1016/0017-9310(90)90109-8.

[106] Y.Y. Hsu, On the Size Range of Active Nucleation Cavities on a Heating Surface, J. Heat Transfer. 84 (1962) 207–213. doi:10.1115/1.3684339.

[107] M.V. Santos, M. Sansinena, J. Chirife, N. Zaritzky, Determination of heat transfer coefficients in plastic French straws plunged in liquid nitrogen, Cryobiology. 69 (2014) 488–495. doi:10.1016/j.cryobiol.2014.10.010.

[108] D. Lide, CRC Handbook of Chemistry and Physics, 98th ed., CRC Press, 2005. doi:10.1136/oem.53.7.504.

[109] J. Charmant, Kinovea, (n.d.). https://www.kinovea.org/ (accessed May 2, 2018).

[110] D. Nečas, P. Klapetek, Gwyddion: An open-source software for SPM data analysis, Cent. Eur. J. Phys. 10 (2012) 181–188. doi:10.2478/s11534-011-0096-2.

[111] D.D.E. Brennhaugen, K. Georgarakis, Y. Yokoyama, K.S. Nakayama, L. Arnberg, R.E. Aune, Probing heat generation during tensile plastic deformation of a bulk metallic glass at cryogenic temperature, Sci. Rep. 8 (2018) 16317. doi:10.1038/s41598-018-34681-4.

[112] J. Luo, Y. Shi, Tensile fracture of metallic glasses via shear band cavitation, Acta Mater. 82 (2015) 483–490. doi:10.1016/j.actamat.2014.09.008.

[113] Y. Li, S.C. Ng, C.K. Ong, H.H. Hng, T.T. Goh, Glass forming ability of bulk glass forming alloys, Scr. Mater. 36 (1997) 783–787. doi:10.1016/S1359-6462(96)00448-4.

[114] Z.P. Lu, Y. Li, S.C. Ng, Reduced glass transition temperature and glass forming ability of bulk glass forming alloys, J. Non. Cryst. Solids. 270 (2000) 103–114. doi:10.1016/S0022-3093(00)00064-8.

[115] A. Inoue, N. Nishiyama, H. Kimura, Preparation and Thermal Stability of Bulk Amorphous Pd40Cu30Ni10P20 Alloy Cylinder of 72 mm in Diameter, Mater. Trans. JIM. 38 (1997) 179–183. doi:10.2320/matertrans1989.38.179.

[116] Z.P. Lu, H. Tan, S.C. Ng, Y. Li, The correlation between reduced glass transition temperature and glass forming ability of bulk metallic glasses, Scr. Mater. 42 (2000) 667–673. doi:10.1016/S1359-6462(99)00417-0.

[117] C.A. Angell, Formation of glasses from liquids and biopolymers, Science (80-.). 267 (1995) 1924–1935. doi:10.1126/science.267.5206.1924.

[118] L.-M. Wang, C.A. Angell, R. Richert, Fragility and thermodynamics in nonpolymeric glass-forming liquids, J. Chem. Phys. 125 (2006) 074505. doi:10.1063/1.2244551.

[119] R. Busch, J. Schroers, W.H. Wang, Thermodynamics and kinetics of bulk metallic glass, MRS Bull. 32 (2007) 620–623. doi:10.1557/mrs2007.122.

[120] P.G. Debenedetti, F.H. Stillinger, Supercooled liquids and the glass transition, 2001. doi:10.1038/35065704.

[121] N.A. Mauro, M. Blodgett, M.L. Johnson, A.J. Vogt, K.F. Kelton, A structural signature of

liquid fragility, Nat. Commun. 5 (2014) 4616. doi:10.1038/ncomms5616.

[122] Z.J. Yan, J.F. Li, S.R. He, Y.H. Zhou, Evaluation of the optimum solute concentration for good glass forming ability in multicomponent metallic glasses, Mater. Res. Bull. 38 (2003) 681–689. doi:10.1016/S0025-5408(03)00010-2.

[123] A. Inoue, T. Zhang, A. Takeuchi, Ferrous and Nonferrous Bulk Amorphous Alloys, Mater. Sci. Forum. (1998). doi:10.4028/www.scientific.net/MSF.269-272.855.

[124] R.J. Highmore, A.L. Greer, Eutectics and the formation of amorphous alloys, Nature. (1989). doi:10.1038/339363a0.

[125] CALPHAD, CALPHAD, (n.d.). http://www.calphad.org/ (accessed August 26, 2018).

[126] P.J. Spencer, A brief history of CALPHAD, Calphad. 32 (2008) 1–8. doi:10.1016/J.CALPHAD.2007.10.001.

[127] Scientific Group Thermodata Europe, SGTE Applications, (n.d.). http://www.crct.polymtl.ca/sgte/index.php?what=1&customers=1 (accessed August 27, 2018).

[128] OpenCalphad, Available Open Databases, (n.d.). http://www.opencalphad.com/databases.html (accessed August 27, 2018).

[129] A. van de Walle, C. Nataraj, Z.-K. Liu, The Thermodynamic Database Database, Calphad. 61 (2018) 173–178. doi:10.1016/J.CALPHAD.2018.04.003.

[130] Scientific Group Thermodata Europe, SGTE Databases, (n.d.). http://www.crct.polymtl.ca/sgte/index.php?what=1&databases=1 (accessed August 27, 2018).

[131] T.-C. Software, Thermo-Calc Databases, (n.d.). http://www.thermocalc.com/products-services/databases/thermodynamic/ (accessed August 27, 2018).

[132] A. Zhu, G.J. Shiflet, D.B. Miracle, Glass forming ranges of Al–rare earth metal alloys: thermodynamic and kinetic analysis, Scr. Mater. 50 (2004) 987–991. doi:10.1016/J.SCRIPTAMAT.2004.01.019.

[133] L. Xia, S.S. Fang, Q. Wang, Y.D. Dong, C.T. Liu, Thermodynamic modeling of glass formation in metallic glasses, Appl. Phys. Lett. 88 (2006) 171905. doi:10.1063/1.2198830.

[134] Thermo-Calc Software AB, TCFE7 - TCS Steels/Fe-Alloys Database, Version 7.0, (2013).

[135] J.O. Andersson, T. Helander, L. Höglund, P. Shi, B. Sundman, Thermo-Calc & DICTRA, computational tools for materials science, Calphad. 26 (2002) 273–312. doi:http://dx.doi.org/10.1016/S0364-5916(02)00037-8.

[136] P. Duwez, S.C.H. Lin, Amorphous Ferromagnetic Phase in Iron-Carbon-Phosphorus Alloys, J. Appl. Phys. 38 (1967) 4096. doi:10.1063/1.1709084.

[137] J. Wang, R. Li, N. Hua, L. Huang, T. Zhang, Ternary Fe-P-C bulk metallic glass with good soft-magnetic and mechanical properties, Scr. Mater. 65 (2011) 536–539. doi:10.1016/j.scriptamat.2011.06.020.

[138] Metglas Inc, Metglas - history, (n.d.). https://metglas.com/company-history/ (accessed August 28, 2018).

[139] Y. Yoshizawa, S. Oguma, K. Yamauchi, New Fe-based soft magnetic alloys composed of ultrafine grain structure, Cit. J. Appl. Phys. 64 (1988) 6773. doi:10.1063/1.369007.

[140] A. Makino, A. Inoue, T. Mizushima, Soft magnetic properties of Fe-based bulk amorphous alloys, Mater. Trans. JIM. 41 (2000) 1471–1477. doi:10.2320/matertrans1989.41.1471.

[141] C.-Y. Lin, H.-Y. Tien, T.-S. Chin, Soft magnetic ternary iron-boron-based bulk metallic glasses, Cit. Appl. Phys. Lett. 86 (2005) 162501. doi:10.1063/1.1901808.

[142] A. Inoue, Y. Shinohara, J.S. Gook, Thermal and Magnetic Properties of Bulk Fe-Based Glassy Alloys Prepared by Copper Mold Casting, Mater. Trans. JIM. 36 (1995) 1427–1433. doi:10.2320/matertrans1989.36.1427.

[143] J. Shen, Q. Chen, J. Sun, H. Fan, G. Wang, Exceptionally high glass-forming ability of an FeCoCrMoCBY alloy, Cit. Appl. Phys. Lett. 86 (2005) 2342. doi:10.1063/1.110520.

[144] J.H. Yao, H. Yang, J. Zhang, J.Q. Wang, Y. Li, The influence of Nb and Zr on glass-formation ability in the ternary Fe–Nb–B and Fe–Zr–B and quaternary Fe–(Nb,Zr)–B alloy systems, J. Mater. Res. 23 (2008) 392–401. doi:10.1557/JMR.2008.0055.

[145] A. Inoue, K. Kobayashi, J. Kanehira, T. Masumoto, Mechanical properties and thermal stability of (Fe, Co, Ni)-M-B (M=IV, V and VI group transition metals) amorphous alloys with low boron concentration, Sci. Reports Res. Institutes, Tohoku Univ. Ser. A, Physics, Chem. Metall. 29 (1981) 331–342.

[146] M. Stoica, K. Hajlaoui, J. Das, J. Eckert, A.R. Yavari, FeNbB BULK METALLIC GLASS WITH HIGH BORON CONTENT, 2008. https://www.researchgate.net/publication/259475581 (accessed September 5, 2018).

[147] T. Bitoh, Effect of B2O3 Fluxing on Glass-Forming Ability and Soft Magnetic Properties of Fe(-Co)-B-Si-Nb Bulk Metallic Glasses, Mater. Sci. Forum. 783–786 (2014) 1895–1900. doi:10.4028/www.scientific.net/MSF.783-786.1895.

[148] H.W. Kui, A.L. Greer, D. Turnbull, Formation of bulk metallic glass by fluxing, Appl. Phys. Lett. 45 (1984) 615–616. doi:10.1063/1.95330.

[149] T. Itoi, A. Inoue, Thermal stability and soft magnetic properties of Fe-Nb-B amorphous alloys with high boron concentrations, Mater. Trans. Jim. 40 (1999) 643–647. doi:10.2320/matertrans1989.40.643.

[150] J. Torrens-Serra, P. Bruna, J. Rodriguez-Viejo, S. Roth, M.T. Clavaguera-Mora, Effect of minor additions on the glass forming ability and magnetic properties of Fe–Nb–B based metallic glasses, Intermetallics. 18 (2010) 773–780. doi:10.1016/J.INTERMET.2009.12.006.

[151] S.T. Lin, C.L. Lee, Formation and properties of amorphous (Fe1−xNb x) l B100−l, J. Mater. Sci. 23 (1988) 1324–1328. doi:10.1007/BF01154596.

[152] I. Kaban, P. Jóvári, A. Waske, M. Stoica, J. Bednarčik, B. Beuneu, N. Mattern, J. Eckert, P. Jovari, A. Waske, M. Stoica, J. Bednarcik, B. Beuneu, N. Mattern, J. Eckert, Atomic

structure and magnetic properties of Fe-Nb-B metallic glasses, J. Alloys Compd. 586 (2014) S189–S193. doi:10.1016/j.jallcom.2012.09.008.

[153] I. Škorvánek, J. Kováč, Magnetocaloric Behaviour in Amorphous and Nanocrystalline FeNbB Soft Magnetic Alloys, Czechoslov. J. Phys. 54 (2004) 189–192. doi:10.1007/s10582-004-0061-z.

[154] D. Szewieczek, J. Tyrlik-Held, S. Lesz, Structure and mechanical properties of amorphous Fe84Nb7B9 alloy during crystallisation, J. Achiev. Mater. Manuf. Eng. 24 (2007) 87–90. www.journalamme.org (accessed September 5, 2018).

[155] M. Imafuku, S. Sato, E. Matsubara, A. Inoue, Structural study of Fe90−xNb10Bx (x=10, 20 and 30) glassy alloys, J. Non. Cryst. Solids. 312–314 (2002) 589–593. doi:10.1016/S0022-3093(02)01790-8.

[156] E. Matsubara, S. Sato, M. Imafuku, T. Nakamura, H. Koshiba, A. Inoue, Y. Waseda, Structural study of amorphous Fe 70 M 10 B 20 (M= Zr, Nb and Cr) alloys by X-ray diffraction, Mater. Sci. Eng. A. 312 (2001) 136–144.

[157] Z. Stokłosa, J. Rasek, P. Kwapuliński, G. Haneczok, A. Chrobak, J. Lelątko, L. Pająk, Influence of boron content on crystallization and magnetic properties of ternary FeNbB amorphous alloys, Phys. Status Solidi Appl. Mater. Sci. 207 (2010) 452–456. doi:10.1002/pssa.200925356.

[158] M. Stoica, S. Kumar, S. Roth, S. Ram, J. Eckert, G. Vaughan, A.R. Yavari, Crystallization kinetics and magnetic properties of Fe66Nb4B30 bulk metallic glass, J. Alloys Compd. 483 (2009) 632–637. doi:10.1016/j.jallcom.2007.11.150.

[159] K. Suzuki, J.. Cadogan, K. Aoki, A.. Tsai, A. Inoue, T. Masumoto, Nanocrystallization and glass transition in Cu-Free Fe-Nb-B soft magnetic alloys, Scr. Mater. 44 (2001) 1417–1420. doi:10.1016/S1359-6462(01)00849-1.

[160] M. Imafuku, S. Sato, H. Koshiba, E. Matsubara, A. Inoue, Crystallization Behavior of Amorphous Fe90−XNb10BX (X=10 and 30) Alloys, Mater. Trans. JIM. 41 (2000) 1526–1529. doi:10.2320/matertrans1989.41.1526.

[161] E. Matsubara, S. Tanaka, A. Makino, T.-H. Chiang, Crystallization Behavior of αFe in Fe84Nb7B9 and Fe85Nb6B9 Amorphous Alloys, Mater. Trans. 45 (2004) 1199–1203. doi:10.2320/matertrans.45.1199.

[162] M. Imafuku, S. Sato, H. Koshiba, E. Matsubara, A. Inoue, Structural variation of Fe-Nb-B metallic glasses during crystallization process, Scr. Mater. 44 (2001) 2369–2372. doi:10.1016/S1359-6462(01)00776-X.

[163] J. Torrens-Serra, J. Rodríguez-Viejo, M.T. Clavaguera-Mora, Influence of composition in the crystallization process of Fe75−xNb10B15+x metallic glasses, J. Non. Cryst. Solids. 353 (2007) 842–844. doi:10.1016/J.JNONCRYSOL.2006.12.052.

[164] J. Torrens-Serra, J. Rodríguez-Viejo, M.T. Clavaguera-Mora, Glass forming ability and nanocrystallization kinetics of Fe65Nb10B25 metallic glasses, Phys. Status Solidi. 207 (2010) 1114–1117. doi:10.1002/pssa.200983353.

[165] J. Torrens-Serra, J. Rodríguez-Viejo, M.T. Clavaguera-Mora, Nanocrystallization kinetics and glass forming ability of the Fe 65 Nb 10 B 25 metallic alloy, Phys. Rev. B. 76 (2007)

214111. doi:10.1103/PhysRevB.76.214111.

[166] M. Shapaan, J. Lábár, J. Lendvai, L.K. Varga, Crystallization behavior of Fe62Nb8-xZrxB30 bulk amorphous alloy, Mater. Sci. Eng. A. 375–377 (2004) 789–793. doi:10.1016/j.msea.2003.10.182.

[167] K. Yoshitomi, Y. Nakama, H. Ohtani, M. Hasebe, Thermodynamic Analysis of the Fe – Nb – B Ternary System, ISIJ Int. 48 (2008) 835–844.

[168] D.B. Miracle, D. V Louzguine-Luzgin, L. V Louzguina-Luzgina, A. Inoue, An assessment of binary metallic glasses: correlations between structure, glass forming ability and stability, Int. Mater. Rev. 55 (2010) 218–256. doi:10.1179/095066010X12646898728200.

[169] G.H. Zhao, H. Mao, D. V. Louzguine-Luzgin, Glass forming range of the Ti-Fe-Si amorphous alloys: An effective materials-design approach coupling CALPHAD and topological instability criterion, J. Appl. Phys. 120 (2016) 205106. doi:10.1063/1.4968585.

[170] A. Tabeshian, H. Mao, L. Arnberg, R.E. Aune, Investigation of Glass Forming Ability in the Zr-rich Part of the Zr-Fe-Al Ternary System, Manuscr. Submitt. Publ. (2018).

Publications

Journal of Alloys and Compounds 742 (2018) 952–957

Contents lists available at ScienceDirect

Journal of Alloys and Compounds

journal homepage: http://www.elsevier.com/locate/jalcom

Tensile properties of $Zr_{70}Ni_{16}Cu_6Al_8$ BMG at room and cryogenic temperatures

David D.E. Brennhaugen [a, *], Konstantinos Georgarakis [b], Yoshihiko Yokoyama [c], Koji S. Nakayama [d], Lars Arnberg [a], Ragnhild E. Aune [a]

[a] Department of Materials Science and Engineering, NTNU, Norwegian University of Science and Technology, 7491, Trondheim, Norway
[b] School of Aerospace, Transport and Manufacturing, Cranfield University, Cranfield, MK43 0AL, UK
[c] Institute for Materials Research, Tohoku University, 2-1-1, Katahira, Sendai, 980-8577, Japan
[d] New Industry Creation Hatchery Center, Tohoku University, 2-1-1, Katahira, Sendai, 980-8577, Japan

ARTICLE INFO

Article history:
Received 1 August 2017
Received in revised form
23 January 2018
Accepted 25 January 2018
Available online 31 January 2018

Keywords:
Amorphous materials
Metallic glasses
Mechanical properties

ABSTRACT

The mechanical behaviour in tension of a hypoeutectic $Zr_{70}Ni_{16}Cu_6Al_8$ Bulk Metallic Glass (BMG) was studied at room (295 K) and cryogenic temperatures (150 K and 77 K) using various strain rates between 10^{-4} and 10^{-1} s^{-1}. The yield strength was found to increase at lower temperatures with average values increasing by 16%, from 1503 MPa at 295 K to 1746 MPa at 77 K. The Zr-based BMG was found to exhibit tensile plastic elongation of about 0.4% before fracture at room temperature and high strain rates (10^{-1} s^{-1}). Even higher tensile plasticity was recorded at low temperatures; plastic deformation was found highest at the intermediate temperature (150 K) reaching remarkable plastic strains in the order of 3.9%, while values up to 1.5% were recorded at 77 K. The lateral surface of the tensile specimens was observed in-situ during deformation using a high frame rate camera offering interesting insights with regard to the deformation mechanisms. Room temperature plasticity occurred through the formation and interaction of several nucleated shear bands before critical failure, while at intermediate and liquid nitrogen temperatures, most of the plastic deformation was accommodated through stable flow within a single shear band.

1. Introduction

Bulk Metallic Glasses (BMGs) exhibit a host of interesting and beneficial properties such as high mechanical strength, high hardness, high elastic limit as well as good wear and corrosion resistance, superior to that of conventional crystalline metals and alloys [1]. The bottleneck limiting the wider application of BMGs as structural materials relates, however, to their limited ductility, especially in tension. While BMGs often exhibit considerable plastic strains under compressive loads, most fail prematurely with very limited plastic deformation before fracture under tensile loading. Understanding their precise mechanical behaviour and deformation mechanisms under tensile load is therefore very valuable for the wider applicability of metallic glasses in general.

Deformation in metallic glasses at temperatures below their glass transition ($T \ll T_g$) typically occurs through the formation of highly localized shear bands with a reduced viscosity compared to the bulk material, intersecting the sample at around 45° [2]. The nucleation of these shear bands is thought to happen through the interaction of Shear Transformation Zones (STZ), atomic clusters with lower-than-average density, or higher-than-average free volume, and thus lower shear strength [3,4]. When sufficient elastic energy is stored in the material, cooperative interaction between the STZs will activate their topological coordination leading to the formation of shear bands with thicknesses typically in the order of 20 nm [5,6].

Shear banding is also often related to a localized rise in temperature [2,7–9]. It is thought that local temperature increase in the shear bands is not the primary cause of the viscosity drop, but a secondary effect of the localized plastic deformation [8]. Nevertheless, the increase in temperature may contribute to a further reduction of viscosity and destabilization of the shear bands [2]. The actual magnitude of the heating and its effects has been hotly debated, with answers depending on assumed adiabaticity, local deformation rate and shear band thickness [2,7]. The relation

* Corresponding author.
E-mail address: david.e.brennhaugen@ntnu.no (D.D.E. Brennhaugen).

https://doi.org/10.1016/j.jallcom.2018.01.322
0925-8388/

between shear banding as a deformation mode and temperature, has further put forward the obvious question of the effect of ambient temperature. Theoretical work on yield strength as a function of temperature has shown a good fit with experimental work, when normalized to the glass transition temperatures of different alloys [3,5,10]. Lowered temperature is generally predicted to increase strength. Several experimental studies have looked at different BMG alloys in cryogenic conditions, reporting increases in yield strength [11–13] and plasticity [11,12,14]. Some report the concentration of deformation into one major shear band rather than several minor ones at low temperatures and strain rates [10,15].

Though the operation of shear bands in metallic glasses, i.e. nucleation, propagation and arrest, is still not fully understood [2], intense research efforts in the last decade have improved our understanding of the deformation mechanisms and inspired novel strategies for designing BMGs with higher ductility. For example, phenomena such as nanocrystallization in the shear bands [16], in-situ formation of soft crystalline phases in glassy matrices [17] and structural rejuvenation through thermal cycling [18,19] or thermomechanical processing [20] may provide promising routes for extending ductility in BMGs. Yokoyama et al. [21] have shown that hypoeutectic bulk glass alloys have a promising potential for designing ductile BMGs, due to the higher free volume that can be quenched in during vitrification. Thus, designing a hypoeutectic $Zr_{70}Ni_{16}Cu_6Al_8$ BMG with high Poisson ratio (0.393 ± 0.003) and low Young's modulus (73 ± 4 GPa), plastic deformation positively correlated to strain rate in tensile mode was found, with a maximum of 1.7% at 2×10^{-1} s^{-1}. The plasticity for this alloy was later improved to 2.8% by increasing the sample cooling rate during casting, entrapping higher free volume to facilitate STZ coordination, as well as by testing at 1.5×10^{-1} s^{-1} [22]. This improvement was linked to an increased ability to form multiple shear bands at high strain rates [14,22]. Low temperature and strain rate, i.e. 133 K and 10^{-4} s^{-1} respectively, were found to further increase the plastic deformability, but with a lower number of shear bands apparent on the surface [15].

In the present work, the hypoeutectic $Zr_{70}Ni_{16}Cu_6Al_8$ bulk glassy alloy was tested in tension at various strain rates, nominally 10^{-4}, 10^{-3}, 10^{-2} and 10^{-1} s^{-1}. Ambient temperature was set to 77 K, 150 ± 20 K (referred to as "150 K" from now on) and 295 K during the tests in order to evaluate the effect of strain rate and low temperature on the mechanical behaviour of BMGs and gain new insights on the deformation mechanism. The samples were filmed during the tensile tests using a high frame rate camera, allowing the direct observation of the deformation phenomena and how they are affected by the imposed conditions.

2. Experimental procedure

$Zr_{70}Ni_{16}Cu_6Al_8$ master alloy ingots were produced by weighing out in total 30 g of alloying elements to within an error of 1%. The ingots were automatically melted, flipped and remelted four times in a Diavac Limited arc melter under 5N Ar atmosphere.

A Nissin Giken double torch arc melter and tilt casting system [23] was used to cast cylindrical rods with 3.5 mm diameter and 85 mm length. All castings were done under 5N Ar protective atmosphere using Zr as oxygen getter. The rods were individually verified to be amorphous using a Rigaku Ultima IV X-ray diffractometer. 28 mm long tensile specimens with a 2.3 by 0.8 mm gage area with circular cross section were machined from the cast rods. All samples were polished with 4000 grit lapping tape and checked for surface defects using a Shimadzu HMV-2 ADW optical microscope.

Tensile testing was performed at nominal strain rates of 10^{-1}, 10^{-2}, 10^{-3} and 10^{-4} s^{-1} at 295 K, 150 K and 77 K. Tests at 77 K were done submerged in liquid nitrogen, while the intermediate temperature was achieved by suspending the sample above the liquid nitrogen surface. A specially designed sample holder for liquid nitrogen submersion was used on a strain rate controlled Shimadzu AG-X tensile testing machine. Specimen temperature was measured by a thermocouple attached to the sample holder. Two specimens were tested for each combination of strain rate and temperature.

The tensile tests were filmed using a Photron FASTCAM SA1.12 high speed camera with a Leica Z16 APO lens at framerates between 60 and 5400 frames per second (depending on strain rate). The strain data was measured both by cross-beam displacement and through Digital Image Correlation(DIC) using eCorr software by Egil Fagerholt and Track Eye Motion Analysis software by Imagesystems [24,25]. Young's modulus was found by linear regression of DIC data. Stress-strain curves were constructed by combining the regressed elastic regime with plastic deformation data from the cross-beam displacement, smoothed and scaled to correct for machine compliance. This was done to compensate for high deformability in the special sample holder and for scatter in the DIC results. High compliance in the sample holder required for liquid nitrogen submersion, resulted in only about 20% of the applied nominal strain rate being transferred to the sample. The nominal strain rates are still used as reference for the remainder of the article.

3. Results and discussion

The mechanical behaviour of the $Zr_{70}Ni_{16}Cu_6Al_8$ BMG under uniaxial tensile loading was investigated at temperatures between 295 K and 77 K using various nominal strain rates in the range from 10^{-4} s^{-1} to 10^{-1} s^{-1}. Representative engineering stress-strain curves obtained at various temperatures for strain rates of 10^{-4} and 10^{-2} s^{-1}, are presented in Fig. 1. It is interesting to note the effect on tensile behaviour of the Zr-based hypoeutectic BMG at cryogenic temperatures. The plastic strain increases from a negligible value at 295 K to 3.7% at 150 K, whereas at even lower temperatures (77 K) the plastic strain before fracture is in the order of 2%. These values of plastic deformation at cryogenic temperatures are remarkable for BMGs, which are known to exhibit very limited plastic strains under tensile loading. In addition, a clear increase of the mechanical strength can be observed from about 1400 MPa at 295 K to 1700 MPa at 77 K.

Fig. 2 a) and b) show the yield stress and tensile plastic deformation before fracture, respectively, as a function of temperature for the various strain rates used in the present work. Each value in

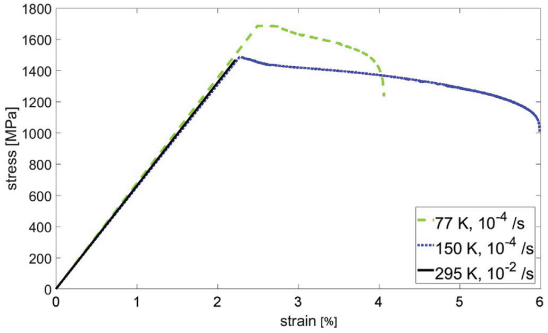

Fig. 1. Representative stress-strain curves for samples tested at 10^{-4} and 10^{-2} s^{-1} nominal strain rate at 77, 150 and 295 K.

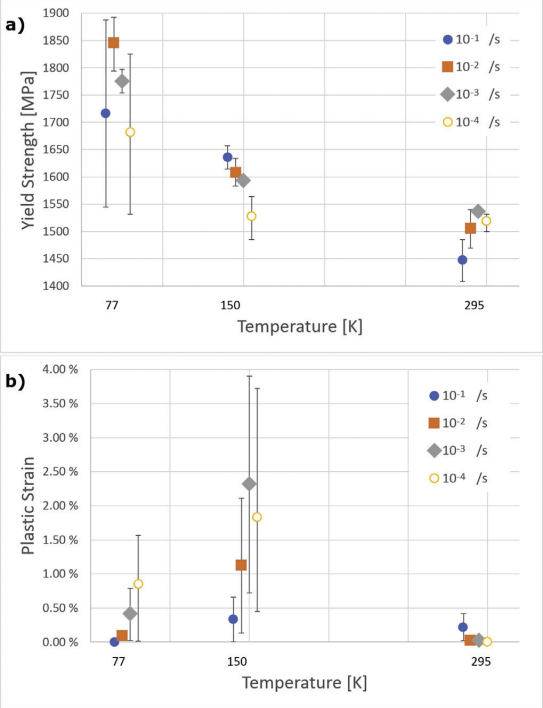

Fig. 2. Comparison of tensile mechanical properties for the $Zr_{70}Ni_{16}Cu_6Al_8$ BMGs for various strain rates ranging between 10^{-1} to 10^{-4} s^{-1} at 77, 150 and 295 K: a) Yield strength as a function of temperature and b) Plastic strain before fracture as a function of temperature. Error bars mark highest and lowest measured values.

these graphs represents the average of two independent experiments, whereas the error bars indicate the highest and lowest measurements in the group. The dispersion of values in the yield strength and ductility, indicated by the error bars in Fig. 2a) and b) respectively, is firstly noted. Such dispersion may not be surprising for the tensile properties of BMGs and may be related to the sensitivity of their mechanical behaviour to nano- and micro-scale defects, as well as local structural variations introduced during casting. Therefore, for the remainder of the present work, focus is on the main clear trends observed in the graphs rather than the absolute values.

In Fig. 2a) the tensile yield strength, σ_y, is observed to increase with decreasing temperature for all the strain rates used in this work. This increase in the yield strength is in the order of 10–15% from 295 K to 77 K, in good agreement with the strengthening of BMGs at cryogenic temperatures reported in the literature [5,10–13,26]. It has been proposed that the strengthening at cryogenic temperatures may be attributed to structural densification related with the reduction of atomic radii through the reduction of thermal atomic fluctuations and to increased bond strengths at low temperatures [5,11–13,26]. In addition, such behaviour may be related to the reduced mobility of STZs, which are thermally hindered from assuming positions conductive to cooperative shear [12]. Between 150 and 295 K, there happens an apparent reversal of strain rate sensitivity with regards to yield stress. Maass et al. showed a good fit for positive correlation with strain rate below a critical temperature (approximated to 200 K for the similar Vit105 alloy) [10], drawing the analogy to non-Newtonian flow in viscous media. For compressive deformation, the disappearance of flow serration was reported at the same temperature, along with a reversal of strain rate sensitivity. This was explained by structural rejuvenation around the STZ when sufficient thermal energy and time is supplied [27].

Fig. 2b) shows the tensile plastic elongation of $Zr_{70}Ni_{16}Cu_6Al_8$ as a function of temperature for the strain rates used in the present work. Interestingly, the hypoeutectic Zr-based BMG exhibits (limited but appreciable) room temperature ductility at higher strain rates (~10^{-1} s^{-1}), whereas no plastic deformation was observed at lower strain rates 10^{-2}-10^{-4} s^{-1}. The absence of tensile plastic deformation at low strain rates and the ductility at high strain rates is in general agreement with previous observations by Yokoyama et al. [22]. It has to be noted, however, that the tensile elongation at room temperature and high strain rates observed in the present work is lower than that observed by Yokoyama et al. [22], which may be related to the sensitivity of the tensile behaviour of BMGs to the manufacturing processes as well as to variations in machine compliance. More interestingly, increased tensile ductility can be observed at 150 K for all the strain rates, reaching a remarkable 2.4% average plastic strain at 10^{-3} s^{-1} strain rate, despite the observed dispersion of measured values. At even lower temperature, 77 K, the tensile ductility decreases again but maintains appreciable plastic deformation values of the order of 0.8% and 0.4% at 10^{-4} s^{-1} and 10^{-3} s^{-1} strain rates respectively. Change in plastic deformability at low temperatures has been previously reported at various magnitudes. Dependent on alloy composition, improvements in plastic tensile deformability at cryogenic temperatures have ranged from none [13], through less than one percent [11,12] to several percent [15] for Zr-based BMGs. Lower strain rate gives higher plasticity for both cryogenic temperatures, which could relate to the change from a Newtonian to non-Newtonian regime in the stress-strain rate-temperature relationship of the viscosity in the sliding shear band.

Fig. 3a), b) and c) shows images recorded in-situ by a high-speed camera during the tensile test of the Zr-based BMG (at 295 K and 10^{-1} s^{-1} strain rate) at progressive stages of deformation, while Fig. 3d) shows a zoom-in at the plastic deformation region of the corresponding stress-strain curve. As can be seen from Fig. 3a) a shear step formed on the surface of the tensile specimen about 35 ms before fracture as a result of a shear band operating in a cross-sectional plane. Fig. 3b) shows the formation of a second shear step in close proximity, eventually intersecting the first shear band. After intersection, the specimen enters a new elastic-like linear regime before fracture finally occurs through the second shear band as seen in Fig. 3c). In the present work, tensile plasticity at room temperature was only observed when two (or more) shear bands nucleated to intersect each other, as shown in Fig. 3b) and c). Tensile plastic deformation at room temperature occurs through the formation of multiple shear bands; thus, the operation of a higher number of shear bands increases the recorded plastic deformation and increases the probability of interacting with each other. The formation of multiple shear bands during tensile loading provokes the serrated flow observed in Fig. 3d), resembling the serrated flow observed under compressive loads [9,28]. The temporal resolution to deeply study flow serrations was however not available on the used setup. Previous work [15] found a positive correlation between absolute number of shear bands observed on the sample surface and strain rate, suggesting a higher deformability at higher strain rates, supporting the present observations.

On the other hand, even though higher tensile ductility was observed at cryogenic temperatures as shown in Figs. 1 and 2b), plastic deformation was accommodated mainly through the operation of a single shear band. Fig. 4a) through c) shows images of the evolution of plastic deformation for $Zr_{70}Ni_{16}Cu_6Al_8$ during tension

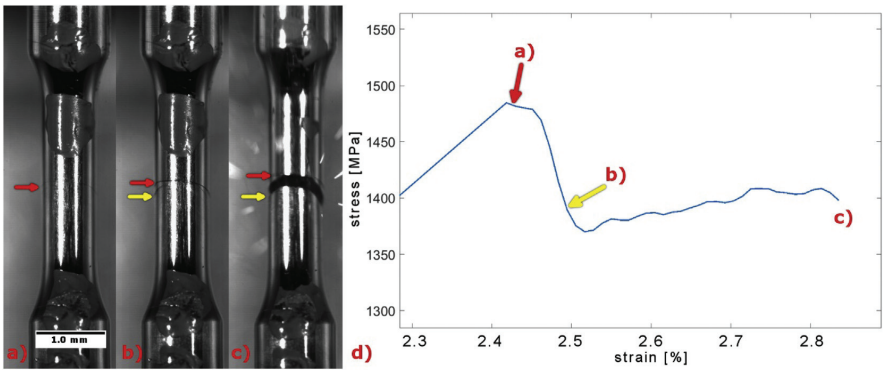

Fig. 3. Nucleation of intersecting shear bands at 295 K, 10^{-1} s^{-1} nominal strain rate. a) first shear band, red arrow, appears 35 ms before fracture, b) second shear band, yellow arrow, nucleates to intersect first shear band at 30 ms before fracture and c) final fracture along second shear band. Corresponding locations in the stress-strain relationship are marked in d). (For interpretation of the references to colour in this figure legend, the reader is referred to the Web version of this article.)

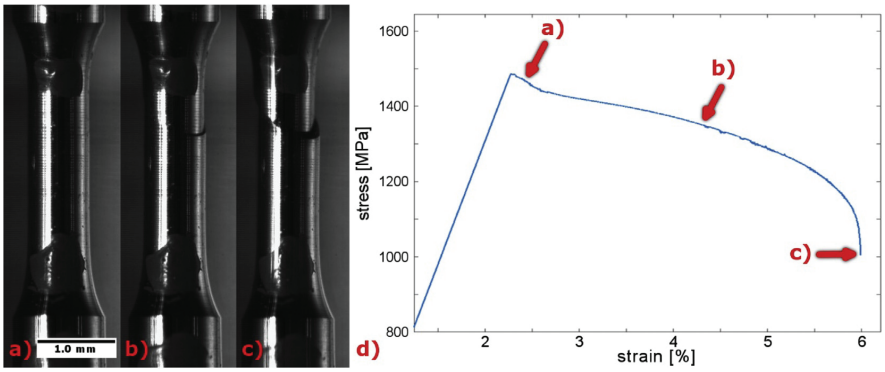

Fig. 4. Nucleation and propagation of single shear band in stable flow at 150 K, 10^{-4} s^{-1} nominal strain rate. a) first trace of shear band 80 s before fracture, b) extent of shear band flow 38 s before fracture and c) final video frame at the time of fracture. Corresponding locations in the stress-strain relationship are marked in d).

under tensile loading at 150 K and 10^{-4} s^{-1} strain rate. Fig. 4a) shows the initial stages of formation of a large shear step at the surface of the tensile specimen resulting from the operation of one shear band. As can be seen, the shear step forms at the beginning of the yield flow as indicated in Fig. 4d). Plastic deformation in this case mainly occurs through the propagation of this main shear band which remarkably accommodates more than 3% plastic strain before fracture, see Fig. 4b) and c). In the case of tests run at 10^{-4} s^{-1} strain rate, the whole shear event of the major shear band elapsed over the order of tens of seconds, and can therefore be regarded as truly stable plastic flow. The sliding of shear bands can be regarded as exothermic, with the added heat further amplifying the instability of structurally reduced viscosity [7]. At low strain rate and low temperature, both time and driving force are supplied to allow heat to diffuse out from the shear band. This might be enough to delay the final stage of critical failure, letting the viscous layer slide in a stable manner before runaway instability.

Comparison of SEM investigations of fracture and lateral surfaces with what was captured by the recorded videos reveals that the specimens do in fact show nucleation of several minor shear bands, as well as sliding of the primary band. Fig. 5 shows representative micrographs at room temperature, a) and b), and liquid nitrogen, c and d), tests. Evidence of the sliding shear band is marked by lines on the fracture surfaces in Fig. 5a) and c). In the videos, the sliding can only be observed at low temperatures except for the single case shown in Fig. 5. This difference in timeframe, sliding and rupture in only the range of milliseconds at high temperature and over minutes at low temperatures indicates a difference in it's role in deformation. At high temperature, sliding is catastrophic and cannot be stopped. Although the fracture morphology left behind is similar, the sliding at low temperature is slow and can be arrested by unloading [10], and can therefore be regarded as true plasticity. In some cases, only a single shear band nucleated, to accommodate the entire strain, while in most cases a major shear band was selected from among many nucleated ones. This has similarly been observed in both compression [10] and tension [15], where the single shear banding can be related to the presence of defects that induce shear before normally expected flow stress is reached.

Interestingly, tests at 77 K exhibit lower plastic capacity than those at 150 K. In this case deformation still mainly occurs through the operation of the primary shear band, similar to what is observed at 150 K, see Fig. 4.

A linear decrease in impact toughness with decreasing temperature has previously been observed for some metallic glasses [29] which could impact plastic deformability as a competition

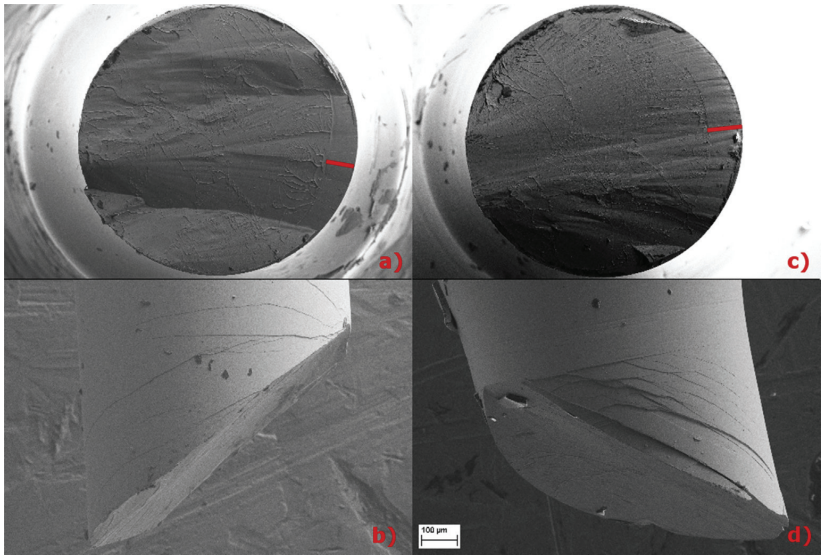

Fig. 5. SEM micrographs of fracture surfaces, top, and lateral surfaces, bottom, of samples tested at room temperature, a) and b), and in liquid nitrogen, c) and d). Sliding of the primary shear band marked by red lines in a) and b). In a) the intersection of two major shear bands, previously shown in Fig. 3 can also be seen. (The spots on the sample surfaces are remainders of marks used for DIC). (For interpretation of the references to colour in this figure legend, the reader is referred to the Web version of this article.)

between embrittlement and shear band stabilization. Reduced mobility of STZs could likewise be a factor in the re-lowering of plasticity at 77 K. If low-temperature deformation is purely driven by STZ coalescence, lower diffusivity could inhibit their ability to accommodate strain, resulting in a more brittle failure.

4. Conclusion

The tensile mechanical behaviour of a $Zr_{70}Ni_{16}Cu_6Al_8$ BMG was investigated at room and cryogenic temperatures using four different nominal strain rates in the range between 10^{-4} and 10^{-1} s^{-1}. The yield strength was found to increase at lower temperatures, ranging from a 1503 MPa average at room temperature to 1746 MPa at 77 K. A reversal of strain rate sensitivity was observed between 150 and 295 K, where low strain rate at room temperature and high strain rate at low temperatures resulted in the highest observed yield strengths. Plastic deformation was found to increase at lower temperatures compared to room temperature. However, tensile ductility does not increase monotonically with decreased temperature; the highest plastic strains were observed at 150 K for all the strain rates reaching an average 2.4% at 10^{-3} s^{-1}, which is remarkable for tensile loading of BMGs. Different mechanisms of apparent plasticity were observed at room and cryogenic temperatures. Tensile plastic deformation at room temperature occurs through the formation of multiple shear bands, whereas at lower temperatures (150 K and 77 K) deformation mainly happens through the operation of a single shear band. The high plastic deformability at lower temperatures and strain rates is thought to stem from the temperature dependence of the Newtonian-non-Newtonian flow transition as well as the reduced adiabaticity of the shear bands due to both an increased driving force and longer allowed time for heat dissipation, allowing a single preferred shear band to deform in a stable manner. At the same time, competition with linearly dropping fracture toughness with a decrease in temperature is thought to contribute to higher plasticity at intermediate temperature than at liquid nitrogen temperature.

Funding

This work was supported by the Department of Materials Science and Engineering, Norwegian University of Science and Technology (NTNU), Trondheim, Norway, and the Institute of Materials Research, Tohoku University, Sendai, Japan.

References

[1] M. Ashby, A.L. Greer, Metallic glasses as structural materials, Scr. Mater. 54 (2006) 321–326, https://doi.org/10.1016/j.scriptamat.2005.09.051.
[2] A.L. Greer, Y.Q. Cheng, E. Ma, Shear bands in metallic glasses, Mater. Sci. Eng. R Rep. 74 (2013) 71–132, https://doi.org/10.1016/j.mser.2013.04.001.
[3] A. Argon, Plastic deformation in metallic glasses, Acta Metall. 27 (1979) 47–58, https://doi.org/10.1016/0001-6160(79)90055-5.
[4] F. Spaepen, Homogeneous flow of metallic glasses: a free volume perspective, Scr. Mater. 54 (2006) 363–367, https://doi.org/10.1016/j.scriptamat.2005.09.046.
[5] W.L. Johnson, K. Samwer, A universal criterion for plastic yielding of metallic glasses with a (T/T g) 2/3 temperature dependence, Phys. Rev. Lett. 95 (2005) 195501, https://doi.org/10.1103/PhysRevLett.95.195501.
[6] A.R. Yavari, K. Georgarakis, W.J. Botta, A. Inoue, G. Vaughan, Homogenization of plastic deformation in metallic glass foils less than one micrometer thick, Phys. Rev. B 82 (2010) 172202, https://doi.org/10.1103/PhysRevB.82.172202.
[7] J.J. Lewandowski, A.L. Greer, Temperature rise at shear bands in metallic glasses, Nat. Mater. 5 (2006) 15–18, https://doi.org/10.1038/nmat1536.
[8] F. Spaepen, Metallic glasses: must shear bands be hot? Nat. Mater. 5 (2006) 7–8, https://doi.org/10.1038/nmat1552.
[9] K. Georgarakis, M. Aljerf, Y. Li, A. LeMoulec, F. Charlot, A.R. Yavari, K. Chornokhvostenko, E. Tabachnikova, G.A. Evangelakis, D.B. Miracle, A.L. Greer, T. Zhang, Shear band melting and serrated flow in metallic glasses 93 (2008) 31907, https://doi.org/10.1063/1.2956666.
[10] R. Maaß, D. Klaumünzer, E.I. Preiß, P.M. Derlet, J.F. Löffler, Single shear-band plasticity in a bulk metallic glass at cryogenic temperatures, Scr. Mater. 66 (2012) 231–234, https://doi.org/10.1016/j.scriptamat.2011.10.044.
[11] L.S. Huo, H.Y. Bai, X.K. Xi, D.W. Ding, D.Q. Zhao, W.H. Wang, R.J. Huang, L.F. Li, Tensile properties of ZrCu-based bulk metallic glasses at ambient and cryogenic temperatures, J. Non Cryst. Solids 357 (2011) 3088–3093, https://doi.org/10.1016/j.jnoncrysol.2011.04.017.
[12] Y.H. Li, W. Zhang, C. Dong, A. Kawashima, A. Makino, P.K. Liaw, Effects of cryogenic temperatures on mechanical behavior of a Zr60Ni25Al15 bulk

metallic glass, Mater. Sci. Eng. A 584 (2013) 7–13, https://doi.org/10.1016/j.msea.2013.06.063.
[13] J. Yi, S.M. Seifi, W. Wang, J.J. Lewandowski, A damage-tolerant bulk metallic glass at liquid-nitrogen temperature, J. Mater. Sci. Technol. 30 (2014) 627–630, https://doi.org/10.1016/j.jmst.2014.04.017.
[14] H. Tokunaga, Y. Nitta, A. Shirota, K. Fujita, Y. Yokoyama, T. Yamasaki, A. Inoue, Tensile plastic deformation of Zr 70 Ni 16 Cu 6 Al 8 bulk metallic glass at cryogenic temperature, J. Jpn. Inst. Met. 73 (2009) 919–923. https://www.jstage.jst.go.jp/article/jinstmet/73/12/73_12_919/_pdf. (Accessed 6 June 2017).
[15] H. Tokunaga, K. Fujita, Y. Yokoyama, Tensile Plastic Deformation Behavior of Zr 70 Ni 16 Cu 6 Al 8 Bulk Metallic Glass at Cryogenic Temperature, (n.d.). https://doi.org/10.2320/matertrans.M2012102.
[16] A.R. Yavari, K. Georgarakis, J. Antonowicz, M. Stoica, N. Nishiyama, G. Vaughan, M. Chen, M. Pons, Crystallization during bending of a Pd-Based metallic glass detected by X-ray microscopy, Phys. Rev. Lett. 109 (2012) 85501, https://doi.org/10.1103/PhysRevLett.109.085501.
[17] S. Pauly, S. Gorantla, G. Wang, U. Kühn, J. Eckert, Transformation-mediated ductility in CuZr-based bulk metallic glasses, Nat. Mater. 9 (2010) 473–477, https://doi.org/10.1038/NMAT2767.
[18] S. V Ketov, Y.H. Sun, S. Nachum, Z. Lu, A. Checchi, A.R. Beraldin, H.Y. Bai, W.H. Wang, D. V Louzguine-Luzgin, M.A. Carpenter, A.L. Greer, Rejuvenation of metallic glasses by non-affine thermal strain, (n.d.). https://doi.org/10.1038/nature14674.
[19] W. Guo, R. Yamada, J. Saida, Rejuvenation and plasticization of metallic glass by deep cryogenic cycling treatment, Intermetallics 93 (2018) 141–147, https://doi.org/10.1016/j.intermet.2017.11.015.
[20] Y. Sun, A. Concustell, A.L. Greer, Thermomechanical processing of metallic glasses: extending the range of the glassy state, Nat. Rev. Mater. 1 (2016) 16039, https://doi.org/10.1038/natrevmats.2016.39.
[21] Y. Yokoyama, K. Fujita, A.R. Yavari, A. Inoue, Malleable hypoeutectic Zr–Ni–Cu–Al bulk glassy alloys with tensile plastic elongation at room temperature, Philos. Mag. Lett. 89 (2009) 322–334, https://doi.org/10.1080/09500830902873575.
[22] Y. Yokoyama, H. Tokunaga, A.R. Yavari, T. Kawamata, T. Yamasaki, K. Fujita, K. Sugiyama, P.K. Liaw, A. Inoue, Tough hypoeutectic Zr-Based bulk metallic glasses, Metall. Mater. Trans. A 42A (2011) 1468–1475, https://doi.org/10.1007/s11661-011-0631-1.
[23] Y. Yokoyama, K. Inoue, K. Fukaura, Pseudo float melting state in ladle arc-melt-type furnace for preparing crystalline inclusion-free bulk amorphous alloy, Mater. Trans. 43 (2002) 2316–2319, https://doi.org/10.2320/matertrans.43.2316.
[24] E. Fagerholt, Field Measurements in Mechanical Testing Using Close-range Photogrammetry and Digital Image Analysis, Norwegian University of Science and Technology, 2012. http://folk.ntnu.no/egilf/Thesis_Egil_Fagerholt.pdf. (Accessed 15 June 2017).
[25] S.X. Song, X.-L. Wang, T.G. Nieh, Capturing shear band propagation in a Zr-based metallic glass using a high-speed camera, Scr. Mater. 62 (2010) 847–850, https://doi.org/10.1016/j.scriptamat.2010.02.017.
[26] R. Maaß, J.F. Löffler, Shear-band dynamics in metallic glasses, Adv. Funct. Mater. 25 (2015) 2353–2368, https://doi.org/10.1002/adfm.201404223.
[27] A. Dubach, F.H. Dalla Torre, J.F. Löffler, Deformation kinetics in Zr-based bulk metallic glasses and its dependence on temperature and strain-rate sensitivity, Philos. Mag. Lett. 87 (2007) 695–704, https://doi.org/10.1080/09500830701494037.
[28] B.A. Sun, S. Pauly, J. Tan, M. Stoica, W.H. Wang, U. Kühn, J. Eckert, Serrated flow and stick–slip deformation dynamics in the presence of shear-band interactions for a Zr-based metallic glass, Acta Mater. 60 (2012) 4160–4171, https://doi.org/10.1016/j.actamat.2012.04.013.
[29] S. Roberts, C. Zachrisson, H. Kozachkov, A. Ullah, A.A. Shapiro, W.L. Johnson, D.C. Hofmann, Cryogenic Charpy impact testing of metallic glass matrix composites, Scr. Mater. 66 (2012) 284–287, https://doi.org/10.1016/j.scriptamat.2011.11.011.

SCIENTIFIC REPORTS

OPEN

Probing heat generation during tensile plastic deformation of a bulk metallic glass at cryogenic temperature

Received: 9 August 2018
Accepted: 18 October 2018
Published online: 05 November 2018

David D. E. Brennhaugen[1], Konstantinos Georgarakis[2], Yoshihiko Yokoyama[3], Koji S. Nakayama[4], Lars Arnberg[1] & Ragnhild E. Aune[1]

Despite significant research efforts, the deformation and failure mechanisms of metallic glasses remain not well understood. In the absence of periodic structure, these materials typically deform in highly localized, thin shear bands at ambient and low temperatures. This process usually leads to an abrupt fracture, hindering their wider use in structural applications. The dynamics and temperature effects on the formation and operation of those shear bands have been the focus of long-standing debate. Here, we use a new experimental approach based on localized boiling of liquid nitrogen by the heat generated in the shear bands to monitor the tensile plastic deformation of a bulk metallic glass submerged in a cryogenic bath. With the "nitrogen bubbles heat sensor", we could capture the heat dissipation along the primary shear banding plane and follow the dynamics of the shear band operation. The observation of nitrogen boiling on the surface of the deforming metallic glass gives direct evidence of temperature increase in the shear bands, even at cryogenic temperatures. An acceleration in bubble nucleation towards the end of the apparent plastic deformation suggests a change from steady-state to runaway shear and premonitions the fracture, allowing us to resolve the sequence of deformation and failure events.

Metallic glasses are a unique group of amorphous materials typically produced by rapid quenching of some selected alloys. While mechanically very strong, these glasses fracture differently from most other metals in that their deformation is localized to thin bands, intersecting the sample body at ~45°[1] to the stress axis. The hows and whys of these shear bands are therefore very important questions for improving deformability in metallic glasses and making them practically applicable.

Although amorphous, a metallic glass is not purely homogeneous at the nanometric scale[2]. The structural origin of shear banding in metallic glasses is thought related to the coalescence of low-density-and-strength atomic clusters, called shear transformation zones, under applied stress[3,4], into ~20 nm[5,6] thin planes. Viscosity reduction through structural dilation[7] then causes preferential deformation in these bands, with the final fracture typically leaving traces of completely molten material on the surface in the form of Saffman-Taylor fingering[8,9]. With viscosity and temperature being intimately related, and considering these shear bands are high-friction environments, the role of temperature and heating in the failure of metallic glasses has received a fair amount of attention. Significant work has focused on the effect of ambient temperature, since cryogenic temperatures have an apparent stabilizing effect on plastic deformation[10–13], as well as on the heating of the shear band itself[7,14–20]. Various methods applied to disentangle structural and caloric effects include coating the metallic glass sample with fusible coatings with known melting points[15,16], high frequency infrared thermography[21,22], back-calculations from estimated viscosity in shear bands[23] and theoretical approaches based on release of elastically stored energy in the sample[19,24] and heat release from shear deformation[25].

[1]Department of Materials Science and Engineering, NTNU, Norwegian University of Science and Technology, 7491, Trondheim, Norway. [2]School of Aerospace, Transport and Manufacturing, Cranfield University, Cranfield, MK43 0AL, UK. [3]Institute for Materials Research, Tohoku University, 2-1-1, Katahira, Sendai, 980-8577, Japan. [4]New Industry Creation Hatchery Center, Tohoku University, 2-1-1, Katahira, Sendai, 980-8577, Japan. Correspondence and requests for materials should be addressed to D.D.E.B. (email: david.e.brennhaugen@ntnu.no)

Lewandowski and Greer studied shear band temperature using their novel fusible coating technique, where they coated samples in tin before bend testing, and observed local melting along shear bands[15]. They confirmed hot zones of 200–1000 nm, which had heated by at least 207 K, to melt the coating. Based on this observation, an initial core temperature of 3400–8600 K was estimated, depending on assumed deformation time. The same technique was later applied by other groups, but molten coating was in those cases only observed on the shear band involved in final fracture[16,20].

Several groups have tried to estimate temperature increases by assuming that work done by elastic contraction of the machine-sample system during yield is released as heat into the shear band. Wang *et al*. calculated increases of up to 1600 K, with hot zones in the range of 1 µm reaching 500 K increase[26]. Similar studies estimated up to 2000 K in a very narrow band, resulting in a 450 K increase in a 0.4 µm hot zone, with the additional note that heating was heavily dependent on assumed shear time, becoming negligible at around 100 ms and upwards[19]. Finite element simulations have also showed that the temperature rise in a shear band can reach values higher than 1000 K[27,28].

The existence of a critical shear time, distance or velocity, all intrinsically related, in relation to heating has similarly been discussed by several groups: Jiang *et al*. found a direct link between global strain rate and temperature increase in individual shear bands, using infrared thermography during compression testing[29]. Other groups found critical shear step sizes[18] and sliding velocities[25,30] for a shear band to destabilize, relating these factors to viscosity drop caused either by temperature or shear strain rate.

Aside from theoretical approaches, the only method allowing direct measurements of the timescale of events has been high frame rate thermography. Such studies have typically given temperature increase values over the duration of shear events in the range 1 to 6 K[22,29,31]. This technique is however, despite rapidly advancing technology, still limited in spatial and temporal resolution to observing hot zones in the 10 µm range after heat has dissipated from the shear band.

Testing and application of metallic glasses at cryogenic temperatures has some important benefits. Strength and plasticity have both been found to increase[11–13]. Further, some groups report the concentration of plastic deformation into few, or even single, shear bands, as opposed to the normally expected multitude[10,13]. The combination of increased plasticity and localization of deformation significantly facilitate the study of shear band dynamics at reduced temperatures.

Here, using a novel "nitrogen bubbles heat sensor" technique, we resolve the shear band dynamics of a tensile specimen submerged in liquid nitrogen (LN2) into three separate stages: steady-state shear, runaway shear and fracture. We study the timescale and related temperature evolution of each step by combining *in-situ* measurements of the stress-strain relationship and high frame rate imaging of deformation and nitrogen boiling on the deforming sample surface, with post-mortem analysis through Atomic Force Microscopy (AFM) and Scanning Electron Microscopy (SEM).

Results

***In-situ* tensile deformation analysis.** We investigated the tensile response of a $Zr_{70}Ni_{16}Cu_6Al_8$ Bulk Metallic Glass (BMG) at a nominal strain rate of $10^{-2}\,s^{-1}$ (effective strain rate measured to $2*10^{-3}\,s^{-1}$ during elastic deformation, due to machine compliance). The testing was performed at cryogenic temperature (77 K) with the sample and part of the testing rig submerged in a LN2 bath. A high frame rate camera was used to record the specimen response during testing. Importantly, we observed nitrogen vapor formation on the sample surface during the latter stages of deformation, as direct evidence of heat release. Figure 1 shows a series of selected video snapshots (see also supporting video) at various degrees of sample deformation and surface boiling.

Figure 2 shows an enlarged view of the plastic deformation part of the recorded stress-strain relationship, with the full curve as an inset. The upper horizontal axis in the figure gives the corresponding timeline, in ms before fracture occurs, as well as the plastic deformation. The sample undergoes about 2.2% elastic deformation, followed by a relatively limited 0.11% plastic response. SEM images of the two sides of the fractured sample, (Fig. 3a,b), indicate that the plastic deformation was mainly accommodated along the primary shear band. This high degree of localization is in accordance with previous reports for cryogenic tensile testing of BMG[10,12,13,32], and will be discussed in further detail later.

Let us now discuss the nitrogen gas bubbles forming on the sample surface during plastic deformation. It is interesting to note that no boiling was observed on the sample surface during the elastic regime, see (Fig. 1a). The first nucleated bubble, at 0.035% plastic deformation, can be seen at 75 ms before fracture, marked by the arrow in (Fig. 1b). After relatively stable boiling for 40 ms, the formation rate of bubbles increases drastically, as in (Fig. 1c), resulting in violent boiling of the LN2 bath in the final ms before fracture occurred, shown in (Fig. 1d). We also note that all bubbles were generated along the same plane, as marked by the dotted line in (Fig. 1a). This line corresponds to the primary shear band that later results in fracture as seen in (Fig. 3a,b). The bubbles seen above this line in (Fig. 1c,d) have risen due to buoyancy in the LN2 bath (Supplementary Video).

Boiling incipience below the homogeneous nucleation temperature of LN2 (105 K)[33], is driven by both the wall and bath superheat as well as the favorability of nucleation sites[34,35]. The presence of nucleating sites along the entire shear band, considering that the shear step geometry varies along its boundary, as well as the fact that the bath was kept open to the atmosphere, indicates that wall superheat is the main driving factor for bubble formation. Thus, the above observations can be considered as direct evidence of heating in the shear band.

In what follows, we attempt to quantify the heat necessary for the formation of the observed bubbles. The work done by bubble growth consists of enthalpy of vaporization, formation of new interfacial surface and displacement of a liquid volume by gas[34]. The latter two are negligible for bubbles of the observed size, so we focus on the former.

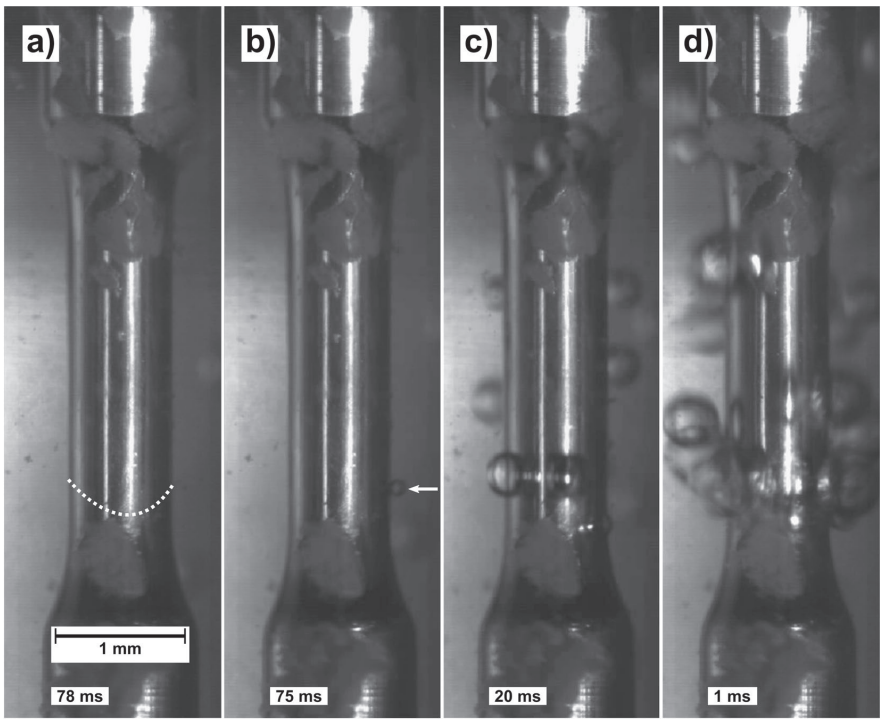

Figure 1. Video snapshots at various stages of plastic deformation during uniaxial tensile loading while submerged in a LN2 bath: (**a**) The sample is shown at 78 ms before fracture (after 0.03% plastic deformation) with no apparent nitrogen gas bubble nucleation. The dotted white line indicates the primary shear plane, along which fracture will eventually occur. (**b**) The sample is shown at 75 ms before fracture (after 0.035% plastic deformation) when the first bubble can be seen nucleating, marked by a white arrow. (**c**) At 20 ms (after 0.09% plastic deformation), bubble nucleation has started accelerating towards violent boiling. (**d**) At 1 ms before fracture (after 0.11% plastic deformation), violent boiling of the LN2 along the primary shear plane is apparent. The arrows in Fig. 2 correspond to the location of each of the snapshots.

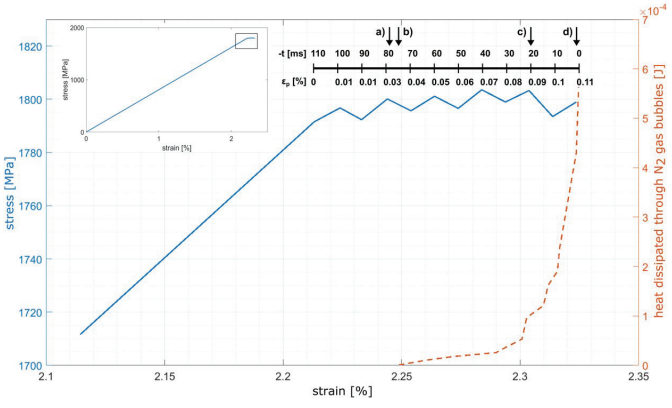

Figure 2. Plastic part of engineering stress-strain relationship (blue line) overlaid with corresponding cumulative energy expenditure for gas evaporation (dashed red line). The inset at the upper left hand corner shows the full stress-strain relationship. The bar above the plastic part of deformation shows time before fracture in ms as well as plastic deformation, with the arrows marked (a) through (d) indicating the locations that correspond to the snapshots in Fig. 1.

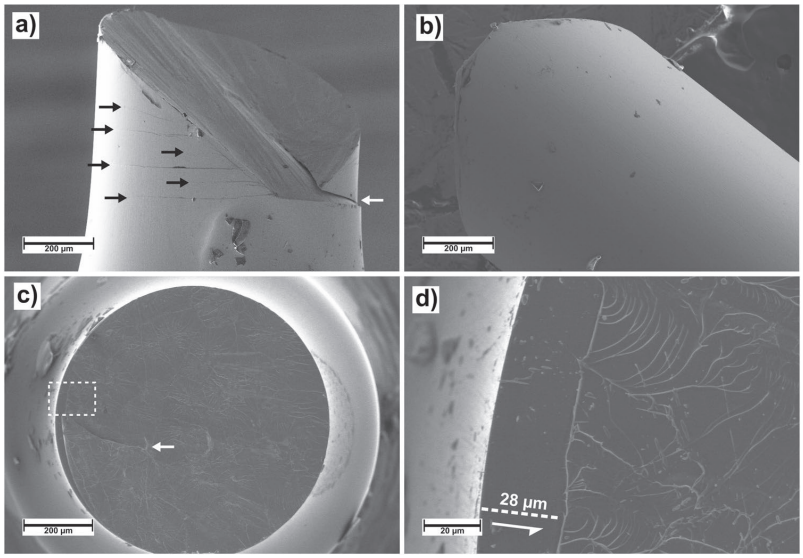

Figure 3. SEM micrographs of tensile specimen after fracture at cryogenic temperature. Several secondary shear bands, marked by black arrows in (**a**), can be seen emerging from the primary shear band. The secondary shear bands do not continue to the other half of the sample, (**b**), indicating they were generated after the primary. Overview of the fracture surface, (**c**), reveals a featureless sliding zone, while the remaining surface is covered in characteristic Saffman-Taylor fingering. In (**d**), the dotted square in (**c**) is enlarged to measure the sliding zone length. Shear direction is indicated by a white arrow. A crack in the surface, marked by white arrows in (**a**,**c**), indicates that sliding first happened along the primary shear band, before final fracture occurred along the intersection of the primary and a secondary shear band. The dark particles on the surface, primarily visible in (**a**,**b**), are remainders of tracer markings used for image analysis[13].

Studying the recorded video frame-by-frame, we measure the time of nucleation as well as the time and diameter at release from the sample surface for each bubble. We then use the ideal gas law with the volume of a sphere inserted to estimate the number of evaporated LN2 molecules, n, by

$$n = \frac{4P\pi r^3}{3RT} \tag{1}$$

where P is internal gas pressure (assumed atmospheric), r bubble radius, R the universal gas constant and T is temperature (approximated here to the equilibrium 77 K). The number of gas molecules can then be directly translated to consumed heat by the heat of vaporization, $\Delta H_{vap} = 5.57\ kJ/mol$ for nitrogen[36]. A total heat consumption of $5.6*10^{-4}$ J is measured by the final frame, with the whole estimated heat profile plotted by the red, dashed line in Fig. 2.

N_2 close to its boiling point does not act as a perfectly ideal gas, so the use of Equation 1 must be regarded as an approximation. However, the trend of heat dissipation from the shear band through the LN2, as shown in Fig. 2, should be independent of the actual deviation from ideal behaviour.

Released heat from the shear plane increases in a stable, quasi-linear fashion between 0.035% and 0.08% plastic strain, as seen in Fig. 2. The heat release starts to increase drastically at about 0.09% of plastic strain, Fig. 2, indicating an apparent change in the shear band propagation. We consider the deformation recorded on the stress-strain curve as part of the steady state regime[7], as the shear propagation rate seems to be approximately constant and relatively slow. The change however in boiling dynamics foreshows the transition into "runaway" shear[30], as we observe both increased heating and a slight apparent stress drop. This transition will be discussed in further detail later. During steady-state flow, effective strain rate on the sample is equal to the nominal strain rate $10^{-2}\,s^{-1}$, while the stress drop during runaway shear gives an increase in strain rate, due to a simultaneous elastic relaxation of the machine-sample system. The acceleration of shear and temperature increase relate to a lowered viscosity in the shear banding runaway regime[7,18,30], eventually leading to imminent fracture.

Post-mortem analysis. To gain further insight into the late stages of deformation and fracture, we investigate the post-mortem fracture surface top-down using SEM. In (Fig. 3c) we see an overview of the surface mostly covered in the characteristic Saffman-Taylor fingering indicating separation along a viscous layer between two plates[8,9]. Along the left-hand edge, a smooth, featureless sliding zone, evidence of shear sliding before final fracture can be seen. A crack, also observed in (Fig. 3a), indicates that final fracture occurred along the intersection

of the primary shear band and a major secondary shear band. Generation of the secondary shear band happened after sliding of the primary, evident by the lack of a sliding zone above the crack.

The featureless zone seen in (Fig. 3c), is studied in further detail in (Fig. 3d). The widest part of the featureless zone indicates the shear displacement of the two surfaces before fracture, and is measured to 28 µm in the top-down projection. Accounting for the 54 ° shear band angle to the tensile axis in the present sample, this measurement gives a total in-plane shear displacement of 34.6 µm. Interestingly, the 0.11% plasticity in the stress-strain curve only corresponds to 4.3 µm in-plane sliding, marking a clear discrepancy between *in-situ* and post-mortem observations.

We therefore divide shear deformation into two regimes by what is observable by the testing rig, *i.e.* 4.3 µm steady-state and 30.3 µm runaway shear. Comparing the timescales of the events, the steady-state shear happened over 110 ms, while the runaway sliding occurred in less than 1 ms, as it was neither caught by the testing rig (temporal resolution 100 Hz) nor the camera (spatiotemporal resolution of 6.4 µm/px and 1000 Hz). We can use these numbers to calculate propagation velocities in the respective regimes: For the steady-state shear, we assume constant velocity[23] directly translatable from the cross-beam displacement, as there was no sufficient stress drop to make system compliance significant. The measured strain rate gives an in-plane sliding velocity of $4*10^{-5}\,ms^{-1}$. In comparison, the runaway shear happened at an average velocity of at least $3*10^{-2}\,ms^{-1}$. There is hence at least a three order of magnitude difference in velocities.

Although supercooled metallic liquids are not fully Newtonian[37], we approximate shear layer viscosity between two plates, η, by

$$\eta = \tau\frac{h}{v} \tag{2}$$

where τ is the shear stress, h the viscous layer thickness and v the sliding velocity[23]. For h we use 20 nm, which corresponds to an estimated initial shear band thickness[6]. As the area reduction at the end of the shear event was only ~5%, we simplify τ to

$$\tau = \sigma_y \sin\alpha \cos\alpha \tag{3}$$

where σ_y is yield stress 1790 MPa and α the shear band angle 54°. Viscosities for the two cases are then calculated to $4.4*10^5$ Pas and $5.6*10^2$ Pas for steady-state and runaway shear, respectively.

In the case of steady-state shear, the calculated viscosity is presumably a slight under-estimate, as the viscous liquid layer thickness might grow throughout the duration of deformation. In the runaway case, the calculated viscosity is an upper bound. Real velocity can be orders of magnitude higher than the minimum we estimate and there is most likely also a significant shear stress drop, which would both decrease viscosity. Potential liquid layer thickness increase is limited in its contribution to a maximum factor of ~6, as final thickness after fracture is 120 ± 40 nm, found through volumetric integration of surface features measured by AFM. In the equilibrium state, the calculated viscosities would correspond to temperatures of 743 K and 908 K for steady-state and runaway shear, respectively, both well above the 630 K glass forming temperature of the alloy[38]. These figures are, however, not directly translatable, considering the viscosity dependence on stress state, heating rate and temperature[7,37,39].

Using the findings on stress and displacement, we quantify the heat generation inside the shear band. Work done by shear deformation is found by

$$W = \tau\delta \tag{4}$$

where δ is the shear offset[40]. Not accounting for energy consumed by structural changes, which should be negligible for displacements of the observed magnitude[18], we treat this work as equal to heat released during the shear banding event, H. For steady-state shear, where we know that $\sigma = \sigma_y$, H becomes 3.7 kJm^{-2}, for a total of $2.3*10^{-3}$ J over the shear band area. Interestingly, this value is about 4 times higher than the heat consumed by the bubble formation in the steady state shear regime ($5.6*10^{-4}$ J, (Fig. 2) implying that about 25% of the heat generated by the work done was dissipated to the LN2 bath through the shear plane. Due to a stress drop of unknown magnitude, the subsequent runaway shear generated less than, but probably close to, 23 kJm^{-2}, $1.44*10^{-2}$ J in total.

Fracture. Studying the fracture morphology of the sample in more detail, we obtain information on the event progression during the catastrophic failure itself. Figure 4 shows some important fracture features. The segregation of fracture domains, marked by smooth cores and radiating veins, is distinct on a large part of the surface at 77 K, in accordance with previous reports on typical tensile fracture surfaces[11,41,42]. The nucleation cores are marked in (Fig. 4a) by dashed lines. Some of the highly localized cores are approximately rhombic in shape, as seen more closely in (Fig. 4b), and align with each other and roughly with the shear direction.

The ridges demarking the domains of their respective voids forming a Voronoi tessellation implies that fracture has initiated at each of these voids simultaneously. The lack of directionality in the vein pattern further indicates that the present fracture has been driven outwards by normal stresses, rather than shear. Several of the nucleation cores are rhombus-shaped, oriented along the direction of deformation. This shape suggests involvement of shear forces in the core nucleation, fitting well with shear induced cavitation[30] in the late stages of failure.

The presence of a viscous ridge defining the featureless zone, as seen in (Fig. 3d), further suggests that final separation has not initiated along this line and originates mainly from the cores.

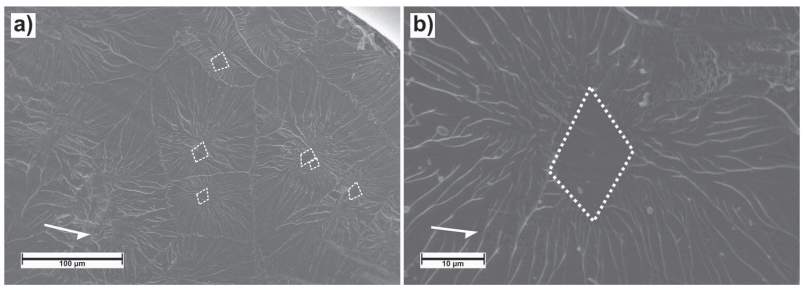

Figure 4. Fracture morphology showing the characteristic viscous fracture. (**a**) Overview micrograph of fracture surface showing Saffman-Taylor fingering radiating out from smooth cores. Some distinctly rhombus-shaped cores are marked by dashed lines. (**b**) Shows a magnified image of a rhombus-shaped core, with the arrow marking shear band sliding direction.

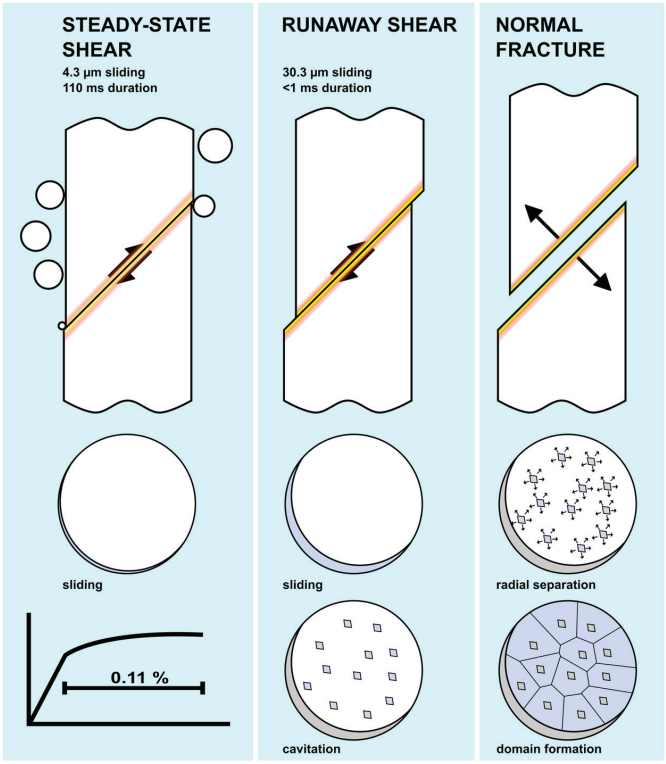

Figure 5. Side and top-down view of the progressive stages of deformation and failure. Active stages in the top-down view are marked in deep blue, while previous stages are grey. First, we observe limited steady-state deformation, with bubbles nucleating along the shear band edges. Further larger scale sliding happens in the runaway state, with increased heat release, ending in shear induced cavitation. The final fracture spreads outwards from the shear induced cores.

Discussion

Based on the combination of *in-situ* and post-mortem analysis, we estimate the deformation-and-fracture sequence as summarized in Fig. 5. Steady-state shear happened over the duration of 110 ms, comprising 0.11% plastic deformation. In the latter 77 ms of this deformation stage, we observe an increasing number of bubbles nucleating on the sample surface. The incipience of boiling is 33 ms after onset of plasticity, and the heat release remains relatively low, ~$0.5*10^{-4}$ J up to 0.085% of measured steady-state strain. In the final 0.025% of observable

plastic strain, the released heat increases by an order of magnitude, and presumably further during runaway shear not captured in Fig. 2. Thus the results point towards the heat release following the operation of the shear band, in accord with previous theoretical analyses by Jiang *et al.*[43], as well as experimental results[16,20].

If we assume an initial hot zone around the shear band of 1 µm, the wall heat flux during the initial stable boiling becomes ~0.3 MWm^{-2}. Comparing this to previous experiments by Okuyama and Iida, this flux should result in boiling incipience at a wall superheat around 20 K[33]. The required wall superheat could however be somewhat lower if the surrounding LN2 were already superheated. The temperature at the end of shear could approach 1000 K, based on the equilibrium viscosity calculations.

Using Equation 1, we calculate a total heat consumption of $5.6*10^{-4}$ J, equivalent to 25% of the work done, *i.e.* $2.3*10^{-3}$ J as calculated by Equation 4. The consumed heat cools the sample surface, so that no new bubble nucleates until sufficient superheat is provided again[44], explaining why a single spot does not continue to nucleate bubbles immediately after being activated. The increase in nucleation rate towards the end of steady-state shear premonitions the transition into runaway deformation.

Sun *et al.*[30] proposed 10^{-4}-10^{-3} ms^{-1} as a threshold between steady-state and runaway shear. The velocities calculated for the present sample are $4*10^{-5}$ and at least $3*10^{-2}$ ms^{-1} for the two regimes respectively, falling neatly on either side of that threshold. The latter could, however, be several orders of magnitude higher. Correspondingly, previously reported values suggest above 10^{-3} ms^{-1} for hot shear bands in similar glasses[18].

The transition from runaway shear to final fracture occurs once the viscous layer is sufficiently unstable to allow shear induced cavitation[30]. In (Fig. 4a,b) we observe Saffman-Taylor fingering[8,9] radiating out from smooth cores. This fracture morphology is similar to that seen in previous reports on tensile testing, at both room[32] and cryogenic temperature[11,42,45]. Some previously reported surfaces show round cores with a degree of directionality in the viscous fingering, consistent with the shear direction[11,32], indicating normal stress driven cavitation and shear driven final fracture. However, our results show several cavitation cores with clearly defined rhombic shapes, roughly oriented in the shear direction, as in (Fig. 4b). This morphology indicates involvement of shear forces during cavitation. That the veins radiate omnidirectionally and form a Voronoi tessellation, see (Fig. 4a), is indicative of normal stress domination when driving the voids outwards. Previously, it has been suggested that the cores themselves nucleate due to normal stresses, but are then driven outward by shear[11,32]. Our results seemingly show the opposite order of dominating stresses.

Conclusion

We observe steady-state shear band propagation during tensile testing at 10^{-2} s^{-1} in LN2 through 0.11% macroscopic plasticity. Heat generation is evidenced at this stage by local boiling of the surrounding LN2 bath. The boiling consumes an estimated $5.6*10^{-4}$ J, corresponding to about 25% of the calculated work done by shear deformation. Steady-state shear occurred over 110 ms, with an acceleration in boiling marking the imminent destabilization of the band. The commencement of boiling after 0.085% plastic strain, and at a relatively low wall superheat, indicates that the heating follows the operation of the shear band. Once the shear band reaches runaway instability, its propagation accelerates by several orders of magnitude, and can only be observed post-mortem. At a critical point, the liquid layer is sufficiently weakened to let shear forces nucleate fracture through cavitation at several sites across the shear band simultaneously. These voids spread outwards by normal forces, generating a surface covered in the characteristic Saffman-Taylor fingers radiating outwards from each void.

The presented findings give a novel way of analyzing heating and propagation of shear bands. The clear observation of the steady-state shear band dynamics helps pinpoint the limit below which the deformation is still arrestable, and the bulk metallic glass can be safely used. This approach could be translated directly to ambient temperature cases by submerging the sample in various liquid mixtures with different boiling points and enthalpies of evaporation.

Experimental Procedures. $Zr_{70}Ni_{16}Cu_6Al_8$(ZNCA) master alloy ingots were produced by arc melting high purity elements in a Diavac Limited custom-made, automatic arc melter. A Nissin Giken double torch arc melter was used to produce ø = 3.5 mm, l = 12.5 mm cylindrical rods by tilt casting[46]. Full vitrification was ensured by X-ray diffraction using a Rigaku Ultima IV with a Cu target and $20° < 2\theta < 100°$. Tensile specimens with gauge area ø = 0.8 mm and l = 2.3 mm were machined from the rods. P4000 lapping tape was used to polish the specimen gauge areas, which were inspected by optical microscopy.

A specially made sample holder consisting of two coaxial rods allowed the tensile specimen to be submerged in LN2 while mounted in a displacement controlled Shimadzu AG-X tensile testing machine with a data gathering frequency of 100 Hz, and a resolution of 15 kPa and 20.8 nm. A high frame rate camera, Photron FASTCAM SA1.12, was used to record the sample through a window in the LN2 container during deformation. The sample was tested at nominal strain rate 10^{-2} s^{-1}, with corresponding video frame rate 1000 Hz and a resolution of 6.4 µm per pixel. The actual strain rate during elastic deformation in the sample was $2*10^{-3}$, due to low machine stiffness resulting from the required sample holder setup. Digital image correlation was used to find the stress-strain relationship, as explained elsewhere[13]. Note that the plotted irregularities in the plastic deformation correspond in magnitude to load cell resolution, and do not necessarily reflect real serration events like observed in compression testing[19]. The elastic region was smoothed mathematically, while the plastic region was left unsmoothed to preserve more accurate data. The present work focuses on a single sample which is a subset of a previously reported work[13]. The reported boiling was, however, observed for all samples tested in LN2. Only one sample was chosen for deeper analysis due to its coincidence of plastic deformability, high video quality and a suitable strain- and frame rate.

Kinovea 0.8.15 software was used to study the resulting video frame-by-frame. The diameter of bubbles evolving along the shear band was measured at the frame of release. Timestamps for first appearance and release from the sample surface were noted. Bubbles hidden behind the sample were accounted for by a correction factor of

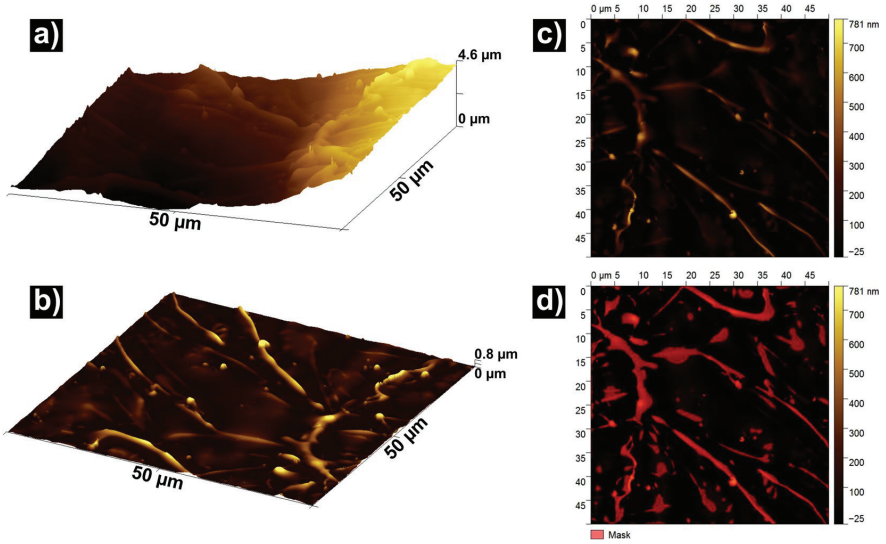

Figure 6. AFM scan of a selected area on the fracture surface, detailing the process of the viscous layer thickness measurement. (**a**) Shows the original scan in 3D, while (**b**) is the same area after flattening through polynomial subtraction. (**c**) is a map of the same area, where (**d**) is a mask of the highest 80%, considered to constitute the viscous layer involved in shear and fracture.

17%, based on average bubble size compared to the sample width. A low angle of view limited size distortion of bubbles, allowing direct measurements regardless of position relative to the specimen.

SEM was used to inspect the sample side and fracture surface. A Zeiss Ultra 55 and a Hitachi S−3400N were used, both in secondary electron mode.

The thickness of the viscous layer was measured by studying the fracture surface by AFM, in an Agilent 5500 microscope. 9 representative $50 \times 50\ \mu m^2$ spots across the sample were scanned. Results were visualized and analyzed using Gwyddion 2.49 software[47]. The total volume of the present vein pattern was found by first subtracting the global topography of the scan by an automatically generated 11th degree polynomial (highest possible in the program). The highest remaining part (80%) of the sample surface was then taken to represent the Saffman-Taylor fingering[9], which was spatially integrated using an automatic feature in the software. The calculated volume was then used to find the thickness of the original layer. The stepwise procedure for an example scan is shown in Fig. 6 where (a) depicts the initial scanned area, (b) and (c) the same area after polynomial flattening and d) shows the raised areas taken to have composed the liquid layer, which is then spatially integrated.

References

1. Greer, A. L., Cheng, Y. Q. & Ma, E. Shear bands in metallic glasses. *Mater. Sci. Eng. R Reports* **74**, 71–132 (2013).
2. Laws, K. J., Miracle, D. B. & Ferry, M. A predictive structural model for bulk metallic glasses. *Nat. Commun.* **6**, 8123 (2015).
3. Spaepen, F. Homogeneous flow of metallic glasses: A free volume perspective. *Scr. Mater.* **54**, 363–367 (2006).
4. Argon, A. S. Plastic deformation in metallic glasses. *Acta Metall.* **27**, 47–58 (1979).
5. Li, J., Spaepen, F. & Hufnagel, T. C. Nanometre-scale defects in shear bands in a metallic glass. *Philos. Mag. A Phys. Condens. Matter, Struct. Defects Mech. Prop.* **82**, 2623–2630 (2002).
6. Zhang, Y. & Greer, A. L. Thickness of shear bands in metallic glasses. *Appl. Phys. Lett.* **89**, 071907 (2006).
7. Guan, P., Chen, M. & Egami, T. Stress-temperature scaling for steady-state flow in metallic glasses. *Phys. Rev. Lett.* **104**, 205701 (2010).
8. Pampillo, C. A. & Reimschuessel, A. C. The fracture topography of metallic glasses. *J. Mater. Sci.* **9**, 718–724 (1974).
9. Saffman, P. G. & Taylor, G. The Penetration of a Fluid into a Porous Medium or Hele-Shaw Cell Containing a More Viscous Liquid. *Proc. R. Soc. A Math. Phys. Eng. Sci.* **245**, 312–329 (1958).
10. Maaß, R., Klaumünzer, D., Preiß, E. I., Derlet, P. M. & Löffler, J. F. Single shear-band plasticity in a bulk metallic glass at cryogenic temperatures. *Scr. Mater.* **66**, 231–234 (2012).
11. Huo, L. S. *et al.* Tensile properties of ZrCu-based bulk metallic glasses at ambient and cryogenic temperatures. *J. Non. Cryst. Solids* **357**, 3088–3093 (2011).
12. Tokunaga, H., Fujita, K. & Yokoyama, Y. Tensile Plastic Deformation Behavior of Zr70Ni16Cu6Al8 Bulk Metallic Glass at Cryogenic Temperature. *Mater. Trans.* **53**, 1395–1399 (2012).
13. Brennhaugen, D. D. E. *et al.* Tensile properties of Zr70Ni16Cu6Al8BMG at room and cryogenic temperatures. *J. Alloys Compd.* **742**, 952–957 (2018).
14. Spaepen, F. Metallic glasses: Must shear bands be hot? *Nat. Mater.* **5**, 7–8 (2006).
15. Lewandowski, J. J. & Greer, A. L. Temperature rise at shear bands in metallic glasses. *Nat. Mater.* **5**, 15–18 (2006).
16. Ketov, S. V. & Louzguine-Luzgin, D. V. Localized shear deformation and softening of bulk metallic glass: Stress or temperature driven? *Sci. Rep.* **3**, 2798 (2013).
17. Song, S. X. & Nieh, T. G. Flow serration and shear-band viscosity during inhomogeneous deformation of a Zr-based bulk metallic glass. *Intermetallics* **17**, 762–767 (2009).

18. Cheng, Y. Q., Han, Z., Li, Y. & Ma, E. Cold versus hot shear banding in bulk metallic glass. *Phys. Rev. B - Condens. Matter Mater. Phys.* **80**, 134115 (2009).
19. Georgarakis, K. *et al*. Shear band melting and serrated flow in metallic glasses. *Appl. Phys. Lett.* **93**, 031907 (2008).
20. Slaughter, S. K. *et al*. Shear bands in metallic glasses are not necessarily hot. *APL Mater.* **2**, 096110 (2014).
21. Wang, G. *et al*. Thermographic studies of temperature evolutions in bulk metallic glasses: An overview. *Intermetallics* **30**, 1–11 (2012).
22. Thurnheer, P., Haag, F. & Löffler, J. F. Time-resolved measurement of shear-band temperature during serrated flow in a Zr-based metallic glass. *Acta Mater.* **115**, 468–474 (2016).
23. Yokoyama, Y. *et al*. Viscous flow in sliding shear band formed during tensile deformation of hypoeutectic Zr-based metallic glass. *Intermetallics* **19**, 1683–1687 (2011).
24. Yavari, A. R., Georgarakis, K., Botta, W. J., Inoue, A. & Vaughan, G. Homogenization of plastic deformation in metallic glass foils less than one micrometer thick. *Phys. Rev. B - Condens. Matter Mater. Phys.* **82**, 172202 (2010).
25. Miracle, D. B., Concustell, A., Zhang, Y., Yavari, A. R. & Greer, A. L. Shear bands in metallic glasses: Size effects on thermal profiles. *Acta Mater.* **59**, 2831–2840 (2011).
26. Wang, J. G. *et al*. How hot is a shear band in a metallic glass? *Mater. Sci. Eng. A* **651**, 321–331 (2016).
27. Battezzati, L. & Baldissin, D. Quantitative evaluation of lengthscales for temperature rise in shear bands and for failure of metallic glasses. *Scr. Mater.* **59**, 223–226 (2008).
28. Bazlov, A. I., Churyumov, A. Y., Buchet, M. & Louzguine-Luzgin, D. V. On Temperature Rise Within the Shear Bands in Bulk Metallic Glasses. *Met. Mater. Int.* **24**, 481–488 (2018).
29. Jiang, W. H., Liao, H. H., Liu, F. X., Choo, H. & Liaw, P. K. Rate-dependent temperature increases in shear bands of a bulk-metallic glass. *Metall. Mater. Trans. A Phys. Metall. Mater. Sci.* **39**, 1822–1830 (2008).
30. Sun, B. A., Yang, Y., Wang, W. H. & Liu, C. T. The Critical Criterion on Runaway Shear Banding in Metallic Glasses. *Sci. Rep.* **6**, 21388 (2016).
31. Yang, B. *et al*. *In-situ* thermographic observation of mechanical damage in bulk-metallic glasses during fatigue and tensile experiments. *Intermetallics* **12**, 1265–1274 (2004).
32. Zhang, Z. F., Eckert, J. & Schultz, L. Difference in compressive and tensile fracture mechanisms of Zr59Cu20Al10Ni8Ti3bulk metallic glass. *Acta Mater.* **51**, 1167–1179 (2003).
33. Okuyama, K. & Iida, Y. Transient boiling heat transfer characteristics of nitrogen (bubble behavior and heat transfer rate at stepwise heat generation). *Int. J. Heat Mass Transf.* **33**, 2065–2071 (1990).
34. Blander, M. & Katz, J. L. Bubble nucleation in liquids. *AIChE J.* **21**, 833–848 (1975).
35. Hsu, Y. Y. On the Size Range of Active Nucleation Cavities on a Heating Surface. *J. Heat Transfer* **84**, 207–213 (1962).
36. Lide, D. *CRC Handbook of Chemistry and Physics. CRC Handbook of Chemistry and Physics*, https://doi.org/10.1136/oem.53.7.504 (CRC Press, 2005).
37. Way, C., Wadhwa, P. & Busch, R. The influence of shear rate and temperature on the viscosity and fragility of the Zr41.2Ti13.8Cu12 .5Ni10.0Be22.5metallic-glass-forming liquid. *Acta Mater.* **55**, 2977–2983 (2007).
38. Yokoyama, Y. *et al*. Tough Hypoeutectic Zr-Based Bulk Metallic Glasses. *Metall. Mater. Trans. A* **42**, 1468–1475 (2011).
39. Khonik, V. A., Ohta, M. & Kitagawa, K. Heating rate dependence of the shear viscosity of a finemet glassy alloy. *Scr. Mater.* **45**, 1393–1400 (2001).
40. Zhang, Y. *et al*. Local temperature rises during mechanical testing of metallic glasses. *J. Mater. Res.* **22**, 419–427 (2007).
41. Chen, S. H., Chan, K. C. & Xia, L. Fracture morphologies of Zr-based bulk metallic glasses under different stress states. *Adv. Eng. Mater.* **17**, 366–373 (2015).
42. Jiang, M. Q. *et al*. Cryogenic-temperature-induced transition from shear to dilatational failure in metallic glasses. *Acta Mater.* **77**, 248–257 (2014).
43. Jiang, M. Q. & Dai, L. H. On the origin of shear banding instability in metallic glasses. *J. Mech. Phys. Solids* **57**, 1267–1292 (2009).
44. Myers, J. G., Yerramilli, V. K., Hussey, S. W., Yee, G. F. & Kim, J. Time and space resolved wall temperature and heat flux measurements during nucleate boiling with constant heat flux boundary conditions. *Int. J. Heat Mass Transf.* **48**, 2429–2442 (2005).
45. Li, Y. H. *et al*. Effects of cryogenic temperatures on mechanical behavior of a Zr60Ni25Al15bulk metallic glass. *Mater. Sci. Eng. A* **584**, 7–13 (2013).
46. Yokoyama, Y., Inoue, K. & Fukaura, K. Pseudo Float Melting State in Ladle Arc-Melt-Type Furnace for Preparing Crystalline Inclusion-Free Bulk Amorphous Alloy. *Mater. Trans.* **43**, 2316–2319 (2002).
47. Nečas, D. & Klapetek, P. Gwyddion: An open-source software for SPM data analysis. *Cent. Eur. J. Phys.* **10**, 181–188 (2012).

Acknowledgements

This work was funded by the Faculty of Natural Sciences at NTNU, Norwegian University of Science and Technology with contributions from both Tohoku University and Cranfield University. The authors thank Professor A. L. Greer for discussions and the Tohoku University technical staff for tensile specimen machining.

Author Contributions

Metallic glass production, casting, tensile testing and SEM was done by D.D.E.B. under direction of Y.Y. and L.A. Motion analysis, SEM and AFM was done by D.D.E.B. under direction of R.E.A. and K.G. Fracture morphology analysis was done by D.D.E.B., K.G. and K.S.N. Boiling nucleation analysis was done by D.D.E.B., K.G. and L.A. D.D.E.B. led the project and the writing of the paper. All authors contributed to interpretation, writing and quality assurance of the results.

Additional Information

Supplementary information accompanies this paper at https://doi.org/10.1038/s41598-018-34681-4.

Competing Interests: The authors declare no competing interests.

Publisher's note: Springer Nature remains neutral with regard to jurisdictional claims in published maps and institutional affiliations.

Journal of Alloys and Compounds 707 (2017) 120–125

Contents lists available at ScienceDirect

Journal of Alloys and Compounds

journal homepage: http://www.elsevier.com/locate/jalcom

Predictive modeling of glass forming ability in the Fe-Nb-B system using the CALPHAD approach

David D.E. Brennhaugen [a, *], Huahai Mao [b], Dmitri V. Louzguine-Luzgin [c], Lars Arnberg [a], Ragnhild E. Aune [a]

[a] Department of Materials Science and Engineering, NTNU, Norwegian University of Science and Technology, 7491 Trondheim, Norway
[b] Department of Materials Science and Engineering, KTH Royal Institute of Technology, 100 44 Stockholm, Sweden
[c] WPI Advanced Institute for Materials Research, Tohoku University, 2-1-1,Katahira, Sendai 980-8577, Japan

ARTICLE INFO

Article history:
Received 7 August 2016
Received in revised form
17 November 2016
Accepted 5 December 2016
Available online 6 December 2016

Keywords:
Amorphous materials
Metallic glasses
Metals and alloys
Rapid-solidification
GFA
Computer simulations
CALPHAD

ABSTRACT

Accurate values needed for the most commonly used indicators of good Glass Forming Ability (GFA) in alloys, *i.e.* the liquidus (T_l), crystallization (T_x) and glass transition (T_g) temperatures, are only available after successful production of the metallic glass of interest. This has traditionally made discovery of new metallic glasses an expensive and tedious procedure, based on trial-and-error methodology.

The present study aims at testing the CALPHAD (Computer Coupling of Phase Diagrams and Thermochemistry) approach for predicting GFA in the Fe-Nb-B system by the use of the Thermo-Calc software and the thermodynamic database TCFE7. The melting temperatures and phase stabilities were calculated and combined with data for an atomic size mismatch factor, λ, in order to identify and map potential high-GFA regions. Selected compositions in the identified regions were later produced by suction casting and melt spinning, and the potential success verified using X-Ray Diffraction (XRD). Differential Scanning Calorimetry (DSC) was also used to compare thermodynamic calculations for the model predictions, and evaluate standard GFA indicators.

The model is found to fit well with literature data, as well as predict new bulk glassy compositions at and around $Fe_{70.5}Nb_7B_{22.5}$. These results show promise in further predictive use of the model.

1. Introduction

Fe-based metallic glasses are of special interest due to their application as soft magnets in electronics [1]. Compared to standard electrical steel, which is commonly used for transformer cores, Fe-based metallic glasses show lower coercivity, higher permeability and resistivity, but somewhat lower saturation magnetization. Important factors hindering the widespread application of the amorphous alloys are, among others, their cost and the difficulty of designing or discovering new alloys.

Although several indicators of good Glass Forming Ability (GFA) are known, these often require after-the-fact analysis, making trial and error the most viable approach. The availability of a precise predictive modeling tool will therefore be valuable as a compliment to the experimental search in the further development of the field.

In the present study focus is on the Fe-Nb-B system, which was the first ternary Fe-based system in which a Bulk Metallic Glass (BMG), *i.e.* a fully amorphous rod with diameter of at least 1 mm, was successfully produced [2,3]. The availability of literature data on known compositions therefore makes the system a good candidate for testing a novel predictive modeling tool based on the CALPHAD (Computer Coupling of Phase Diagrams and Thermochemistry) approach.

The main aim of the present study has been to experimentally verify the viability of such a model, through the production of metallic glasses in both bulk and ribbon form. Thermal stability values obtained through DSC are used to evaluate the stability of the produced glasses in relation to the model.

2. Theory

The reduced glass transition temperature $T_{rg} = T_g/T_l$, where T_g and T_l are the glass transition temperature and the liquidus temperature respectively, was among the earliest proposed indicators of GFA [4]. Several similar indicators utilizing T_g, T_l, the

* Corresponding author.
E-mail address: david.e.brennhaugen@ntnu.no (D.D.E. Brennhaugen).

http://dx.doi.org/10.1016/j.jallcom.2016.12.049
0925-8388/

solidification onset temperature (T_s) or crystallization temperature (T_x), *e.g.* $T_{rg} = T_g/T_s$, $\Delta T_x = T_x - T_g$, $\alpha = T_x/T_l$ *and* $\gamma = T_x/(T_g + T_l)$ [1], have later been proposed, suggesting that these values have at least some indicative power. While T_g remains relatively stable, T_l varies significantly with composition, and is therefore a powerful guide during the design of new glassy alloys. Indeed most BMG are found at eutectic or near-eutectic compositions [5], where T_l is depressed, making phase diagrams an obvious tool during the alloy design phase.

The use of phase diagrams in the search for new metallic glasses is, however, limited to relatively simple systems, where an experimental mapping of temperatures and compositions exists. For more complex systems, which are generally required for good GFA, this approach is difficult. The CALPHAD methodology, which aims at developing models to represent thermodynamic properties for the various phases present in the system of interest, may therefore be used effectively to develop a satisfactory extrapolation of the relevant phase diagrams by mapping a limited number of experimental data points.

The Thermo-Calc software [6] is created using the CALPHAD methodology, and uses extensive thermodynamic databases of assessed systems to calculate the Gibbs free energies of all possible phases present in a system. Based on this, the stable phase at each composition and temperature may be predicted. The TCFE7 database, and other Thermo-Calc compatible thermodynamic descriptions available in literature [7], contain the relevant thermodynamic information on the present Fe-Nb-B ternary system. A Liquidus projection of the Fe-rich corner of the Fe-Nb-B system, taken from Yoshitomi et al. [7] is shown in Fig. 1. However, as the TCFE7 database was developed mainly for applications in the steel-making industry, the system and its subsystems are not fulled assessed, *i.e.* some Nb-B binary and Fe-Nb-B ternary compounds are not included. Thus, the calculations performed in the present study using TCFE7 represent the metastable phase relations. The second set of calculations, based on the independently published thermodynamic description by Yoshitomi et al. [7] is therefore considered to be more reliable in this particular system, and are used to control the quality of the TCFE7 results.

In addition to thermodynamics, topological features may also be used effectively to predict glass formation. This effect has long been accounted for through the empirical requirement for constituent atoms with at least 12% size difference [8]. A more continuous

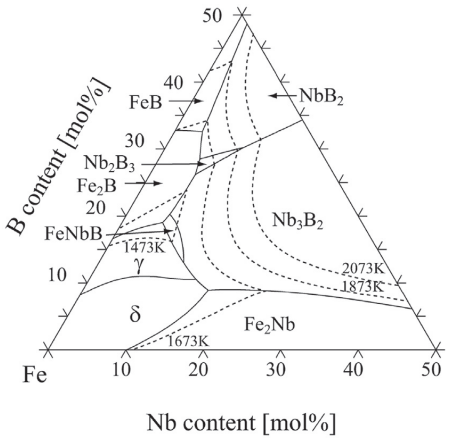

Fig. 1. Liquidus projection of the Fe-rich corner in the Fe-Nb-B system, taken from Yoshitomi et al. [7].

approach to the question of topology was introduced by Egami and Waseda in 1984 [9] through the atomic mismatch factor, λ:

$$\lambda = c^B \left| \left(\frac{r_B}{r_A} \right)^3 - 1 \right| \tag{1}$$

where c^B is the concentration of solute B in matrix A, and r^A and r^B the atomic radii of A and B respectively. By applying equation (1) they established that glass forming was possible at $\lambda \geq 0.1$ for the surveyed binary metallic glasses, and linked this to a critical lattice strain, caused by the volumetric mismatch of the species, required to suppress crystallization. The same concept was later extended to multi-component systems by Sá Lisboa et al. [10].

$$\lambda = \sum_{i=B}^{Z} c_i \left| \left(\frac{r_i}{r_A} \right)^3 - 1 \right| \tag{2}$$

where i denotes the different solutes B through Z in matrix A.

Yan et al. [11] noted that optimal glass forming happens at $\lambda = 0.18$ for several investigated multi-component systems. When assuming that an amorphous material is made up of numerous clusters of icosahedra, the packing efficiency of these is shown to be at its peak at $\lambda = 0.18$.

Similarly, Miracle et al. [12] have used densely packed clusters of varying sizes with both substitutional and interstitial solutes to successfully predict glass forming compositions. This "efficiently packed clusters" model has gone far in pinpointing exact optimal locations for GFA based on topology alone.

While not taking the role of interstitial atoms into account, the λ-factor's simplicity facilitates its combination with other indicative approaches. By combining information on the compositional regions with low liquidus temperatures calculated by the Thermo-Calc software, with knowledge of the optimal λ-factor, a predictive model can be made which encompasses both topological and chemical effects.

3. Methodology

3.1. Model

In the present study Thermo-Calc version 2015a was used with the TCFE7 thermodynamic database, as well as the critically assessed data by Yoshitomi et al. [7], to model the ternary Fe-Nb-B phase diagram. An isothermal rendering at 1450 K of the area of interest, *i.e.* 10–30 at. % B, 0–10 at. % Nb, was used to locate the areas close to the peritectic line where liquid is still in equilibrium with one competing primary crystalline phase at low temperatures. Iso-λ lines from 0.10 to 0.20 were overlaid with the phase diagram to find the compositions with the highest topological susceptibility to glass forming. Two series of compositions were chosen along the two intersecting lines representing the lowest melting point and $\lambda = 0.18$. The isothermal section of the Fe-Nb-B phase diagram at 1450 K, with overlaying iso-λ lines, can be seen in Fig. 2. In the figure, the minimum solute content for expected successful production of amorphous compositions has also been identified.

3.2. Sample production

High purity elements, Fe 99.99 mass % purity, Nb 99.9 mass % purity and B 99.5 mass % purity, were weighed with an error of maximum ±0.2%. Master alloy ingots of 5 g (10 g for melt spinner samples) were prepared by arc melting in Ar atmosphere (99.999%) in an Edmund Bühler MAM-1 arc melter. Each ingot was turned and remelted five times to ensure compositional homogeneity.

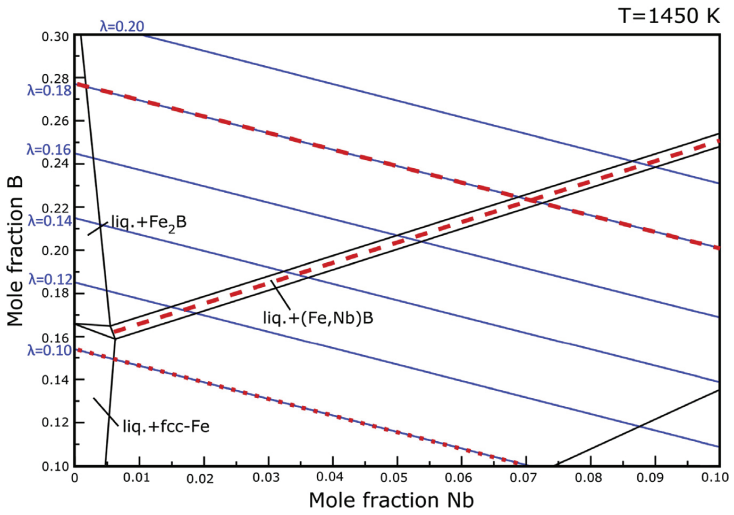

Fig. 2. Isothermal section at 1450 K of the phase diagram Fe-Nb-B calculated by Thermo-Calc using TCFE7. Iso-λ lines are overlaid. The two intersecting lines of expected maximal GFA are drawn in red dashes. Minimum λ value for successful amorphous ribbons is marked with a red dotted line. (For interpretation of the references to colour in this figure legend, the reader is referred to the web version of this article.)

Pieces of approximately 0.3 g each were used to cast 1 mm diameter rods in the suction caster module of the arc melter. Pieces of approximately 0.2 g were melt spun into 30 μm thick ribbons in Ar atmosphere (99.999%) using a copper wheel with a surface velocity of 40 m/s.

3.3. Sample analysis

The structure of the produced materials was studied by X-Ray Diffraction (XRD) with Mo-Kα radiation (Bruker D8 Advance equipped with LynxEye detector) in Θ–2Θ mode.

Prior to analysis, the sample rods were polished lengthwise to a half-cylinder shape, and mounted in a capillary sample holder. By using a Soller slit, this method allows for selective analysis of various regions of the sample rod. The melt spun ribbons were cut into pieces and placed on a Si substrate sample holder. Both the wheel contact surface and the non-contact surface were analyzed to ensure full vitrification. Compositions which were established to be partially or fully crystalline were recast twice to ensure correct results.

Differential Scanning Calorimetry (DSC) was used to evaluate approximate T_g, T_x, T_s and T_l values. Samples were measured for T_g and T_x during heating at 20 K/min, in the range of 303–1573 K, while T_s and T_l were found during cooling at the same rate in a NETZSCH STA449 Jupiter under Ar flow.

4. Results and discussion

High GFA is expected in low-T_l areas where the liquid extending from the Fe-B binary is in equilibrium with a stable Nb-B crystalline phase, as identified using the CALPHAD methodology, while topology is proposed to be at its most beneficent along the 0.18 iso-λ line. It should therefore be expected to find the highest GFA values in the intersection of these two indicators. The locations of the samples produced in the present study are mapped out in the isothermal section of the generated Fe-Nb-B phase diagram, based on data from the TCFE7 database, presented in Fig. 3. As can be seen in the figure, a total of 14 compositions were cast into 1 mm rods, and four were produced as ribbons by melt spinning. Out of these, XRD confirmed seven rods with a completely amorphous cross section, and one amorphous ribbon. The XRD results for the fully amorphous bulk samples are shown in Fig. 4.

From Fig. 3 it can be seen that the successfully produced glassy compositions are concentrated between $\lambda = 0.17$ and $\lambda = 0.20$, while at the same time being close to the peritectic line, in accordance with the assumptions of the model. The dividing line between amorphous and crystalline melt spun ribbons is at $\lambda = 0.10$, as originally proposed by Egami and Waseda [9].

The BMG compositions reported by Yao et al. [13] to exist in the in the Fe-Nb-B system coincide partly with those produced in the present study, as shown in Fig. 5. The composition $Fe_{71}Nb_6B_{23}$ directly overlaps, while $Fe_{68.5}Nb_8B_{23.5}$, $Fe_{70.5}Nb_7B_{22.5}$ and $Fe_{72.5}Nb_6B_{21.5}$ are within 0.5% B of previously reported glasses. The present authors failed to reproduce the amorphous $Fe_{71}Nb_5B_{24}$ alloy, but produced a fully amorphous $Fe_{70.5}Nb_8B_{21.5}$ alloy. The composition $Fe_{71}Nb_8B_{21}$ was, however, previously reported as crystalline. These discrepancies are believed to be attributable to differences in equipment, and individual variance in casting. The amorphous melt spun composition $Fe_{84}Nb_2B_{14}$ has previously been reported by Stoklosa et al. [14], together with $Fe_{87}Nb_2B_{11}$, which has a λ-value below 0.10 and was hence not expected to be amorphous. This suggests that the λ-factor used in the developed model does not signify an absolute limit.

In order to evaluate the trustworthiness of the TCFE7 database used in the present study, an additional phase diagram based on the specific critical assessment of the Fe-Nb-B system by Yoshitomi et al. [7] was generated. An isothermal section at 1450 K of the assessed Fe-Nb-B phase diagram is presented in Fig. 6, overlaid with the locations of samples produced in the present study. The desired multiphase region containing liquid can be seen to be wider than in the TCFE7 model at the same temperature, and its center is offset towards lower B content by about 3 at.%. The FeNbB phase present in the assessed phase diagram is not included in the TCFE7 database, which gives a metastable diagram with a solid solution of FeB and NbB, as well as expected T_s values that are unrealistically high. The important aspect of the phase diagram is, however, the

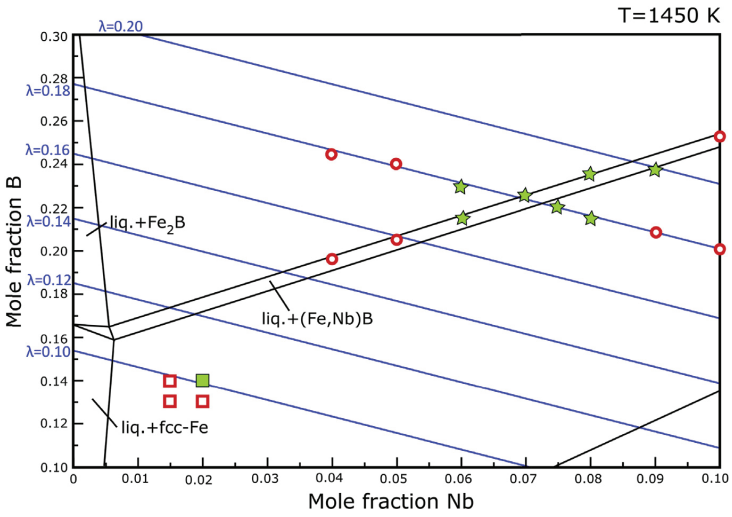

Fig. 3. Isothermal section at 1450 K of the Fe-Nb-B phase diagram produced by Thermo-Calc using the TCFE7 database, overlaid with iso-λ lines and results from the present study. Fully amorphous rods and ribbons are marked as filled green stars and squares respectively. Partly or fully crystalline rods and ribbons are marked as open red circles and squares respectively. (For interpretation of the references to colour in this figure legend, the reader is referred to the web version of this article.)

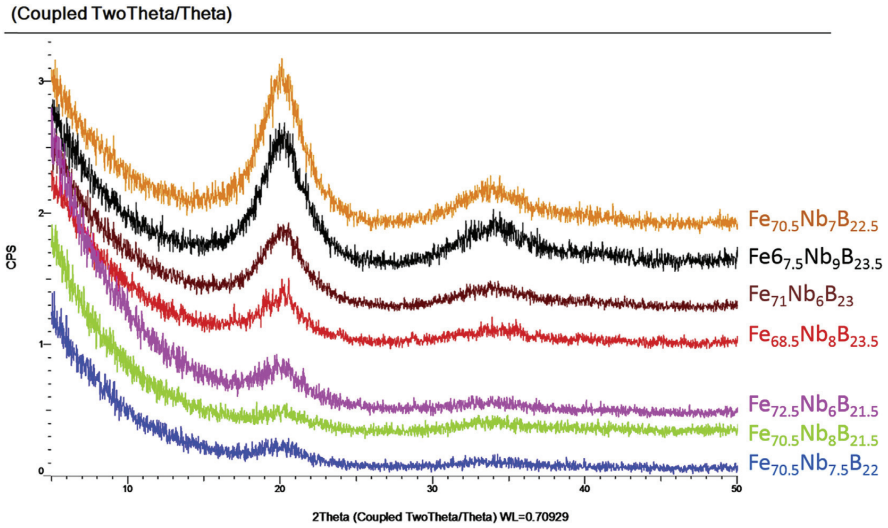

Fig. 4. XRD plots of all successfully cast amorphous rods (all individually examined).

location of the peritectic line, which, with a 3 at.% offset, is still sufficient to identify potential high GFA in the present system.

Thermodynamic stability parameters were evaluated by the use of DSC. A representative trace for the composition $Fe_{67.5}Nb_9B_{23.5}$, showing estimated T_g, T_x, T_s and T_l can be seen in Fig. 7. The DSC results were used to calculate the GFA evaluation parameters T_{rg} and ΔT_g, see Table 1, as well as to compare actual values to those predicted by Thermo-Calc.

As can be seen from Table 1, the DSC results indicate that T_g increases with an increase in the λ-factor, and highest values were found at the proposed optimum of $\lambda = 0.18$. The DSC measured T_l values show a significant offset from the calculated equilibrium values, with deviations of up to 1173 K in the case of TCFE7 and 296 K for those based on Yoshitomi et al. [7]. Significantly, TCFE7 expects a drop in T_l from the BMG samples to the melt spun ribbon, while the assessed model correctly predicts an increase. Both models increase in accuracy towards the Fe corner of the phase diagram. Although the T_l temperatures are not quantitatively correctly predicted, the location of the peritectic line and the correlation with measured values is sufficient for use in the present model.

T_{rg} trends towards higher values with increasing λ, but with

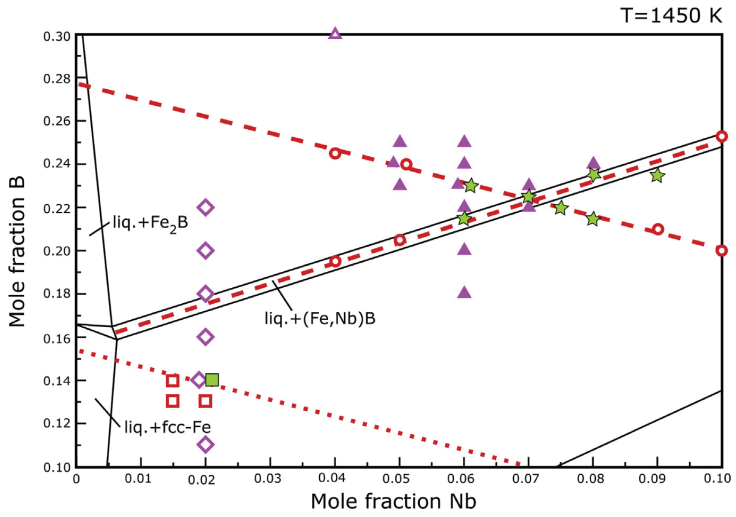

Fig. 5. Isothermal section at 1450 K of the Fe-Nb-B phase diagram produced by Thermo-Calc using the TCFE7 database, overlaid with optimal (red dashes) and minimal (red dots) GFA lines. Results from the present work are compared to BMG and ribbons reported in literature. Fully amorphous rods and ribbons presently produced are marked as filled green stars and squares respectively. Crystalline rods and ribbons are marked as open red circles and squares respectively. The BMG compositions reported from literature are taken from Yao et al. [13] represented by purple filled triangles, and Stoica et al. [2] by purple open triangle. Melt spun ribbons, as reported by Stoklosa et al. [14] are marked as purple open diamonds. (For interpretation of the references to colour in this figure legend, the reader is referred to the web version of this article.)

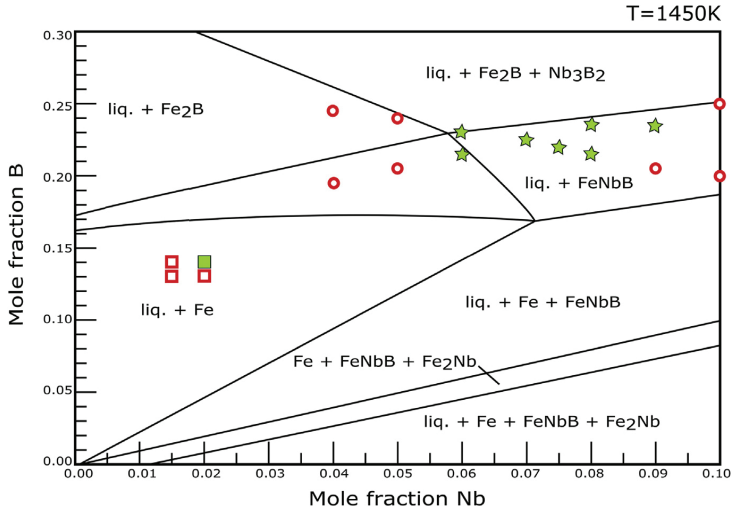

Fig. 6. Isothermal section at 1450 K of the Fe-Nb-B phase diagram produced by Thermo-Calc using assessed data from Yoshitomi et al. [7] Results from the present study are marked (fully amorphous rods and ribbons as filled green stars and squares respectively, crystalline rods and ribbons as open red circles and squares respectively). (For interpretation of the references to colour in this figure legend, the reader is referred to the web version of this article.)

significant spread in values. Interestingly the lowest T_{rg} values are found in two $\lambda = 0.18$ compositions, while higher T_{rg} is also found at similar compositions.

The locations of the successfully produced amorphous alloys suggests that the indications from the model are of sufficient quality to be useful in searching for new BMG in the present system. The main strength of the proposed predictive model derives from its ability to combine chemical factors, through the thermodynamic approach, with topology, from the λ-factor. The method itself is relatively simple to apply, as both the Thermo-Calc computations and the λ-calculations can be automated for a large number of systems, given access to the relevant databases. This could allow fast scanning of several complex systems for potential high-GFA compositions, guiding the experimental exploration. The potential for automatic scanning of alloy systems is also an important tool when working in systems with more than 3 components, which are not easily visualized for manual analysis. A sufficient database is still required to do precise models, which would be a limiting factor

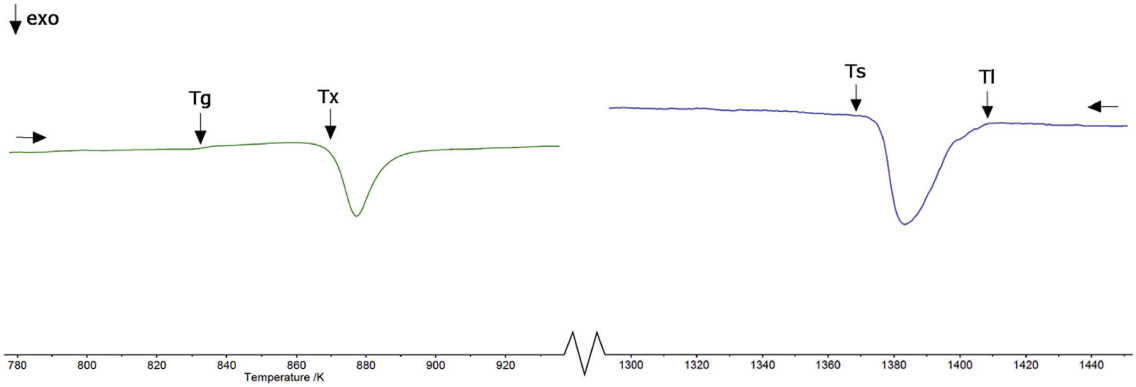

Fig. 7. Representative DSC trace of $Fe_{67.5}Nb_9B_{23.5}$ with T_g, T_x, T_s and T_l values marked.

Table 1
Summary of thermodynamic values obtained through DSC and Thermo-Calc, as well as calculated GFA indicators T_{rg}, ΔT_x and λ

Composition	T_l	T_s	T_g	T_x	T_{rg}	ΔT_x	λ
$Fe_{67.5}Nb_9B_{23.5}$	1408	1369	832	870	0,59	38	0,198
$Fe_{68.5}Nb_8B_{23.5}$	1403	1342	835	888	0,60	53	0,193
$Fe_{70.5}Nb_8B_{21.5}$	1440	1341	838	857	0,58	19	0,180
$Fe_{70.5}Nb_{7.5}B_{22}$	1442	1330	831	866	0,58	35	0,181
$Fe_{70.5}Nb_7B_{22.5}$	1411	1355	829	861	0,59	32	0,181
$Fe_{71}Nb_6B_{23}$	1410	1357	838	859	0,59	21	0,180
$Fe_{72.5}Nb_6B_{21.5}$	1404	1355	821	846	0,58	25	0,170
$Fe_{84}Nb_2B_{14}$	1472	1345	651	672	0,44	21	0,101

in what systems can be surveyed.

5. Conclusion

A predictive model for GFA in the Fe-Nb-B alloy system is proposed and tested. The CALPHAD methodology is used to locate areas of low T_l, and the data is combined with the atomic size mismatch factor λ, in order to identify high-GFA areas. Based on the model, BMG of seven different compositions at and around $Fe_{70.5}Nb_7B_{22.5}$ were produced by suction casting, along with one glassy ribbon by melt spinning at $Fe_{84}Nb_2B_{14}$. The samples show good agreement with the predictions of the model, both in compositional location and in the thermodynamic stability evaluation. Six of the produced BMG compositions were previously unreported.

Acknowledgements

S. V. Ketov, V. Zadorozhnyy, K. Georgarakis and Z. Wang are acknowledged for assistance during the experimental work at WPI Advanced Institute for Materials Research, Tohoku University, Sendai, Japan. M. Stoika is acknowledged for valuable discussions. The research was funded by NTNU, Norwegian University of Science and Technology, Trondheim, Norway.

References

[1] C. Suryanarayana, A. Inoue, Iron-based bulk metallic glasses, Int. Mater. Rev. 58 (2013) 131–166.
[2] M. Stoica, K. Hajlaoui, A. LeMoulec, A.R. Yavari, New ternary Fe-based bulk metallic glass with high boron content, Philos. Mag. Lett. 86 (2006) 267–275.
[3] J.H. Yao, J.Q. Wang, Y. Li, Ductile Fe-Nb-B Bulk Metallic Glass with Ultrahigh Strength, 2008.
[4] D. Turnbull, Under what conditions can a glass be formed? Contemp. Phys. 10 (1969) 473–488, http://dx.doi.org/10.1080/00107516908204405.
[5] H.S. Chen, Glassy metals, Rep. Prog. Phys. 43 (1980) 353. http://iopscience.iop.org/0034-4885/43/4/001/pdf/0034-4885_43_4_001.pdf.
[6] J.-O. Andersson, T. Helander, L. Höglund, P. Shi, B. Sundman, Thermo-calc & DICTRA, computational tools for materials science, Calphad 26 (2002) 273–312.
[7] K. Yoshitomi, Y. Nakama, H. Ohtani, M. Hasebe, Thermodynamic analysis of the Fe-Nb-B ternary system, ISIJ Int. 48 (2008) 835–844.
[8] A. Inoue, Stabilization of metallic supercooled liquid and bulk amorphous alloys, Acta Mater. 48 (2000) 279–306.
[9] T. Egami, Y. Waseda, Atomic size effect on the formability of metallic glasses, J. Non. Cryst. Solids 64 (1984) 113–134.
[10] R.D.S. Lisboa, C. Bolfarini, C.S. Kiminami, Topological instability as a criterion for design and selection of aluminum-based glass-former alloys, Appl. Phys. Lett. 86 (2005) 211904.
[11] Z.J. Yan, J.F. Li, S.R. He, Y.H. Zhou, Evaluation of the optimum solute concentration for good glass forming ability in multicomponent metallic glasses, Mater. Res. Bull. 38 (2003) 681–689.
[12] D.B. Miracle, D.V. Louzguine-Luzgin, L.V. Louzguina-Luzgina, A. Inoue, An assessment of binary metallic glasses: correlations between structure, glass forming ability and stability, Int. Mater. Rev. 55 (2010) 218–256.
[13] J.H. Yao, H. Yang, J. Zhang, J.Q. Wang, Y. Li, The influence of Nb and Zr on glass-formation ability in the ternary Fe–Nb–B and Fe–Zr–B and quaternary Fe–(Nb, Zr)–B alloy systems, J. Mater. Res. 23 (2008) 392–401.
[14] Z. Stokłosa, J. Rasek, P. Kwapuliński, G. Haneczok, A. Chrobak, J. Lelątko, L. Pająk, Influence of boron content on crystallization and magnetic properties of ternary FeNbB amorphous alloys, Phys. Status Solidi 207 (2010) 452–456.